

A Time-resolved Investigation of the Hall Thruster Breathing Mode

by

Robert Bryant Lobbia

A dissertation submitted in the partial fulfillment
of the requirements for the degree of
Doctor of Philosophy
(Aerospace Engineering)
in The University of Michigan
2010

Doctoral Committee:

Professor Alec D. Gallimore, Chair
Professor Iain D. Boyd
Professor Mark Kushner
Professor Yue Ying Lau

© Robert Bryant Lobbia

2010

Acknowledgements

The writing of this dissertation is the culmination of a long educational path I began many years ago that led me to the study of electric propulsion and its unsteady nature. Thus, it is quite important for me to thank my parents (Dr. and Mrs. Bob and DiAne Lobbia) for letting my experimental curiosity flourish—even though building rockets and their motors was not the safest of hobbies in my early years. Later, at the University of California, Los Angeles, I began to understand the deeper principles of rocket propulsion, I learned a lot about running proper experiments of value to the scientific community through working with Professor Ann Karagozian and others in the Combustion Research Laboratory. Also, at that time, I designed advanced hybrid rocket motors with a passionate group of students (Cathy Leong, Yoshi Noda, Saul Rios, Tony Tan, Brian Wiese, and others) in the UCLA AIAA chapter that was guided by undergraduates (myself and others). While figuring everything out on our own often led to many failures and dead ends, we also retained a certain degree of intellectual freedom which spawned ideas that were outside of the box of the conventional approaches taken by others—a quality that is critical to remember when forging new research ideas and technology. At the University of Michigan, I began working with electric propulsion devices under the guidance of Professor Alec Gallimore in the Plasmadynamics and Electric Propulsion Laboratory. Professor Gallimore's expertise and enthusiasm in the field of electric propulsion has always inspired me to work harder to understand the

involved physics of propulsion and to advance the current thruster devices to enhanced performance levels. Professor Gallimore has always replied to my questions with deeply insightful answers and has been very supportive during my graduate student tenure; for these things and others I shall be ever grateful. Also, at the University of Michigan, I had the pleasure of working with an array of some of the brightest students/researchers in the field of electric propulsion including Brian Beal, Dan Brown, Roland Florenz, Dan Herman, Rich Hofer, Dave Huang, Dave Kirtley, Justin Koo ("kooj"), Kristina Lemmer, Ray Liang, Jesse Linnell, Tom Liu, Mike McDonald, Bailo Ngom, Sonca Nguyen, Prashant Patel, Pete Peterson, Bryan Reid, Josh Rovey, Adam Shabshelowitz, Rohit Shastry, Tim Smith, Laura Spencer, Ricky Tang, Allen Victor, and Mitchell Walker. Special acknowledgment is needed to thank Dan Brown for helping me get through the coursework and preliminary exams with helpful discussions and the willingness to provide company at Starbucks from sunrise until closing any day of the week. Also, special thanks to kooj for helping me achieve the Greek ideal of mind and body by out-benching (or out-pacing or out-peddling) me at the gym and for his lively insights on the various methods by which Hall thrusters are numerically simulated. Tom Liu also deserves special thanks for always being able to spare a minute (or hour) to chat as my officemate and for lugging the FASTCAM over to the lab at 2 A.M. to look for high-speed plasma gerbils (spinning at nearly 15,000 R.P.M.). Finally, I need to thank my wonderful wife Tali Lobbia for putting up with my many late nights out with my mistress, $L_aV_aT_eF$, and for her patience and support whilst I was finishing this dissertation.

Forward

Electric propulsion devices have matured significantly since their first inception nearly one century ago. Today, the dedication of researchers in this field continues the advancement and evolution of ways in which electric and magnetic fields work in concert to produce thrust. While at many levels this is driven by the economic advantages the devices offer to the burgeoning telecommunications industry and space-based defense and awareness infrastructures, perhaps the greater inspiration comes from mankind's imperative to explore the cosmos, for "earth is the cradle of humankind, but one cannot live in the cradle forever"—Konstantin E. Tsiolkovsky (in a 1911 letter).

This dissertation is a small part of this effort, with its goal in unveiling a window into the nature of temporally resolved plasmadynamics with direct plasma measurements. Obtaining these measurements was far from trivial, requiring certain breakthrough insights obtained while poring over journal articles or just remembering to think "what if...?" The resulting techniques and devices are laid out in this work in a simple form that others can follow and build upon, for the included time-resolved measurements are perhaps a first of their kind, yet they are surely not the last.

In all things, from the sequence of notes in music to the journey through the turbulent plasma discharge embarked upon in this work, "everything changes and nothing remains still"—Heraclitus (4th century BCE). And just as the oscillating electric and magnetic fields "let there be light," this work hopes to illuminate hitherto unseen

plasmadynamics of devices that are already propelling humankind's exploration of the cosmos.

December 2009

R. Lobbia

Ann Arbor, MI, USA

Table of Contents

Acknowledgements	ii
Forward	iv
List of Figures.....	x
List of Tables	xvii
Abstract.....	xviii
Chapter 1 Introduction.....	1
1.1 Electric propulsion	1
1.2 Hall Effect Thrusters.....	4
1.3 Hall Thruster Clustering	6
1.4 Myriad of Plasma Oscillations in Hall thrusters	7
1.5 Breathing Mode Oscillations	8
1.6 Simple Breathing Mode Model.....	9
1.7 Plasma Fluctuations and Anomalous Transport	11
Chapter 2 Experimental Apparatus.....	13
2.1 Large Vacuum Test Facility.....	14
2.2 Low-power 600-W Hall thruster cluster	15
2.3 Automated Tables	19
2.4 FASTCAM: High-Speed Video System.....	22
2.5 High-Speed DAQ System.....	22
Chapter 3 High Speed Dual Langmuir Probe.....	26

3.1	The Time-resolved Langmuir Probe.....	27
3.2	Background: Rapid Sweep Langmuir Probing.....	27
3.3	Langmuir and Null Probes.....	29
3.4	Probe Transmission Lines.....	32
3.5	Probe Biasing Circuit.....	33
3.6	Dual-symmetric Current Sensing Circuit.....	37
3.7	I-V Trace "Noise" Vanishing Act.....	42
3.8	Error Analysis.....	44
3.9	Typical HDLP I-V processing results.....	47
3.10	Typical HDLP time-resolved plasma properties.....	48
3.11	Conclusions.....	48
Chapter 4 Temporal Limits and Theory of a Langmuir Probe.....		50
4.1	Introduction.....	51
4.2	Electrostatic Probe Theory.....	53
4.3	Simple Langmuir Probe Thin Sheath Analysis.....	54
4.4	Temporal Resolution Limits.....	57
4.4.1	Sheath Transit Time.....	57
4.4.2	Complete Sheath Formation.....	59
4.4.3	Resonance Effects.....	62
4.4.4	Magnetic-Field Effects.....	63
4.4.5	Capacitive Effects.....	64
4.4.6	Sheath Capacitance.....	65
4.4.7	Stray Capacitance.....	66
4.4.8	Mutual Capacitance.....	68
4.4.9	Alternative Capacitance Cancellation Technique.....	69
4.5	Summary of Temporal Sweeping Limits.....	70
4.6	Conclusions.....	73

Chapter 5 Method of Spatiotemporal Data Fusion	74
5.1 Introduction.....	75
5.2 Application of Spatiotemporal Fusion for Plasma Flow Visualization	75
5.3 Experimental Configuration Summary	76
5.4 Turbulent Statistics	77
5.5 Fourier Analysis.....	78
5.6 Empirical Transfer Function Estimation.....	80
5.7 Limitations of the Estimated Transfer Function	82
5.8 Fourier Synthesis of Data.....	84
5.9 Accuracy of Synthesized Signals.....	85
5.10 Overview of Signal Processing.....	86
5.11 Data Fusion Results	90
5.12 Typical Spatiotemporally-fused Density Contour Maps	92
5.13 Method of Data Fusion Conclusions.....	94
Chapter 6 Time and Space Resolved Plume Measurements.....	96
6.1 Deceptively Smooth HET Operation.....	96
6.2 Visual HET Startup Sequence	98
6.3 Hall Thruster Discharge Current Oscillations.....	101
6.4 Single-point Plasma Property Fluctuations.....	108
6.4.1 Ion Transit Delay	110
6.4.2 Variations with Thruster Settings	113
6.5 Electron Temperature and Plasma Potential Fluctuations	122
6.5.1 Plasma Fluctuations in Frequency Space.....	124
6.6 Space and Time Resolved Thruster Plume	126
6.6.1 2D Maps of Time-averaged and Fluctuation Amplitude Electron Density .	126
6.6.2 Two-dimensional Time-resolved Thruster Plume	128

6.6.3	Traveling Ion Waves in the Plume.....	130
6.7	Space and Time Resolved Results for Clustered HETs.....	133
6.7.1	Single-point Plasma Property Fluctuations.....	134
6.7.2	Clustered Modal Behavior	137
6.7.3	2D Maps of Time-averaged and Fluctuation Amplitude Electron Density .	139
6.7.4	Temporally and Spatially Resolved Electron Density Results.....	141
6.7.5	Conclusions.....	145
Chapter 7 Summary and Future Work		147
7.1	Future Work.....	150
Appendix A Measurements of Thrust from Clustered Hall Thrusters		151
A.1	Performance Measurements.....	152
A.2	Thrust Stand and Performance Measurements	153
A.3	Cathode Suspension.....	155
A.4	Single Thruster Performance Measurements.....	156
A.5	Clustered Hall Thruster Performance Measurements.....	161
A.6	Facility Effects on the Production of Thrust.....	163
A.7	Cluster Performance: Additional Results and Discussion	165
A.8	Concluding Remarks.....	167
Bibliography		169

List of Figures

- Figure 1.1 The beehive of known objects in Low-Earth Orbit (LEO). The finite propellant reserves of all satellites limit their operational lifetimes after which they often become debris littering LEO (ESA image 2008). 4
- Figure 1.2. Schematic of Hall Effect Thruster (HET), cross-sectional view showing half the annular discharge channel lined in high-temperature compatible dielectric..... 5
- Figure 2.1. Two-by-two 600-W Hall thruster cluster mounted inside LVTF. The 100-kHz dual Langmuir probe (HDLP) is positioned 10 cm downstream from Thruster3 (T3, the lower-right thruster) upon a pair of remotely controlled positioning tables. 13
- Figure 2.2. The Large Vacuum Test Facility (a) external photographic view and (b) top down schematically view..... 15
- Figure 2.3. Cluster of four 600 W Hall thrusters (with labels) discharging (a) in the LVTF. Inset (b) shows pre-operational front and rear views of the cluster. 17
- Figure 2.4. Flowrate calibration for the four 600-W HETs compared to the nitrogen reference specifications of each MFC..... 19
- Figure 2.5. Overview of experimental setup including: HET cluster, LVTF, 100-kHz HDLP system, FASTCAM, motion control, ADC system, and integration of all subsystems through various digital input/output (I/O) interfaces. .. 21
- Figure 3.1. Photographs of the Langmuir probe (a) prior to experiment and (b) afterwards indicate negligible dimensional and surface changes. 29
- Figure 3.2. Simplified schematic of experiment including the LVTF, 600-W HET, HDLP (attached to a pair of positioning tables), and the HDLP circuits for bias amplification and current sensing (not drawn to scale). Dozens of circuit elements, bypass capacitors, compensation circuits, clamping diodes, trim resistors, voltage rails, etc., are not included in this abbreviate view..... 30
- Figure 3.3. 100 time-resolved I-V characteristics acquired at 100 kHz showing the use of Eqn. (3.1) for HDLP data (a) 10 cm and (b) 60 cm downstream of the HET discharge channel exit. 31

Figure 3.4. SPICE Simulation results for custom developed broadband amplifier and transmission line. Left (a) transient response to input triangle waveform $\pm 10 V_{pk-to-pk}$, into a $5 k\Omega$ dummy load (to roughly simulate plasma loading on circuit). Right plot (b) frequency response of circuit—green trace shows magnitude (bump due to transmission line capacitive and inductive coupling).....	33
Figure 3.5. Broadband power-amplifier and signal-conditioning circuitry in ventilated aluminum enclosure.....	35
Figure 3.6. Various Langmuir probing biasing waveforms considered.....	37
Figure 3.7. COTS current measurement results versus custom current measurement circuit results. The upper trace shows raw current data obtained with “commercial-off-the-shelf” Tektronix P5200 differential high-voltage active probes with SNR of 60 dB. The lower trace shows raw current data obtained with the custom developed dual symmetric current shunt circuit with SNR of 80 dB. A dummy load $3\text{-}k\Omega$ non-inductive power resistor was used in this comparison, and the “Theory” traces correspond to the current expected via Ohm’s law.	41
Figure 3.8. Misleading I-V “noise” observed for a slowly swept (100 Hz sweep rate) Langmuir probe taken (a) 10 cm and (b) 60 cm downstream of the HET. The Raw I-V data pairs are sampled at 2-MHz and their resulting scatter is an indication not of poor measurement technique, but of plasma turbulence. A few averaged I-V traces are fitted to the raw I-V distributions to emphasize the arbitrariness of using the time-averaged I-V characteristic.	43
Figure 3.9. Typical single time-resolved (10- μ s) HDLP I-V characteristic with Langmuir probe algorithm results, shown on linear (a) and logarithmic (b) scales. The first (c) and second (d) electron current derivatives used in generating the lower two plots have not been smoothed, and are computed numerically.	47
Figure 3.10. HDLP time-resolved simultaneous plasma properties measured 20 cm downstream (channel aligned) from the HET. The black solid signal in (a)-(c) shows the instantaneous thruster discharge current, $I_D(t)$, that is dominated by the 19-kHz breathing mode fluctuation. While electron density fluctuations (a) follow the $I_D(t)$ fluctuations with a short delay ($\approx 20 \mu$ s), $T_e(t)$, (b), and $V_p(t)$, (b), track the fluctuations nearly in-phase. This sequence is a small 0.5 ms portion typical of the 1 sec of data collected at this position (see Chapter 6 for additional results and discussion).....	48
Figure 4.1. The important features of this HDLP I-V characteristic are labeled with the upper trace (a) showing the raw probe current (after null probe correction)	

and bias voltage while the lower trace (b) displays the effective electron current on a logarithmic scale. No averaging or smoothing has been applied to these time-resolved I-V data, demonstrating the effectiveness of the HDLP. 54

Figure 4.2. A comparison of time-resolved electron temperature formulations using Eqns. (4.2)-(4.4). (a) Temperature fluctuations (at about 19-kHz) appear nearly in-phase (and close in relative magnitude) with simultaneously sampled thruster (b) discharge current fluctuations. 57

Figure 4.3. (a) Illustration of particles transiting through Langmuir probe sheath (thickness exaggerated). (b) Simple 1D model of the sheath potential. Heavier ions traverse sheath significantly slower. 59

Figure 4.4. Schematic of HDLP configuration including effective sheath, stray, and mutual capacitances. The Langmuir and null probes maintain very close proximity to each other (< 10-mm separation for over 10-m of cabling). The current measurement shunts are placed near the probe bias amplifier. 65

Figure 5.1. Photograph (1/2 sec exposure) of the Hall thruster plume discharged under vacuum conditions. Deceptively stable to the human eye, the exhausted plasma in this photo is violently oscillating at 19 kHz with signal peak-to-peak magnitudes nearly 100% of the DC mean. The thruster is part of a 4 engine cluster, but only single thruster operation is analyzed in this chapter (clustered results are included in Chapter 6)..... 76

Figure 5.2. Quality of synthetic signals versus original signals for three different degrees of transfer function averaging: (a) no averaging, $Q = 1$, (b) $Q = 10$, and (c) $Q = 100$. *Due to sample length reduction by Q , a different portion of the signal is evaluated in each plot.* The synthetic result is taken from the $n_{e|synth}(x_n^*, y_m^*, t_p^*)$ position so that a direct comparison with original data may be shown. 86

Figure 5.3. Flowchart of signal processing steps from raw ADC in upper-left to (clockwise) 2D time-resolved density. 88

Figure 5.4. (a) Time domain discharge current and electron density transients (measured with HDLP) and (b) the respective power spectral densities of these signals in the frequency domain ($Q = 100$ in (b) data). Position is 15 cm downstream from the 600 W HET for both (a) and (b). 90

Figure 5.5. Bode plot of a single-point (15 cm downstream) transfer function from the thruster plume empirically estimated system showing (a) magnitude and (b) phase between discharge current and electron density. Smoothing has been applied. 91

- Figure 5.6. Typical data fusion results for time-resolved two-dimensional electron density contour maps in the plume downstream from a Hall thruster. This 46 μ s sequence of the plasma evolution was synthesized from an empirically estimated transfer function model of the measured thruster plume system using Eqns. (5.4)-(5.6) . Simultaneously acquired FASTCAM high-speed photographs of the HET are included for each density frame. 93
- Figure 6.1 Sequence of visual (a)-(f) non-filtered optical photographs (color-scaled for (h)-(m)), taken with Nikon D80 camera using a 300 mm lens stopped down to f/13 and exposed for 1/3 s at each of the 600-W Hall thruster discharge voltage and mean discharge current settings listed. (g) Shows the integrated total image intensity for each photograph, which in seen to scale roughly linearly with the mean discharge current..... 97
- Figure 6.2. Overlay of color-scaled FASTCAM frame, showing the imaged portion of the 600-W HET discharge channel. 98
- Figure 6.3. startup at 300-V, 2-A discharge. The high-speed optical images, limited to half of the anode as well as the entire cathode, are time-stamped (in microseconds following start of discharge) and presented as intensity plots with warmer colors corresponding to higher intensities. 99
- Figure 6.4. Thruster discharge current signal in (a) time domain and (b) frequency domain. 95% confidence interval shown for power spectrum estimate with $Q = 100$ terms averaged. 200 V 2 A thruster settings..... 102
- Figure 6.5. PSD of thruster discharge current for two thruster conditions: (a) 200 V 1.5 A and (a) 200 V 2 A discharge voltage and time-average discharge current. Both (a) and (b) use $Q = 100$ terms averaged. 103
- Figure 6.6. Discharge current spectra for various 150 V to 400 V thruster discharge voltage settings. The breathing mode peak frequency dominates each operating condition with harmonics visible in most traces. The shaded region behind each spectral trace is the 95% confidence interval of the power spectral density estimates shown (each estimate uses several million samples)..... 105
- Figure 6.7. Breathing mode frequency variation with discharge voltage and mean discharge current operation of a 600-W Hall thruster. While both V_D and I_D effect the frequency of the thruster breathing mode, the discharge voltage plays a stronger role. Theoretical estimate from Eqn. (6.2)..... 108
- Figure 6.8. Time-resolved near-field HET fluctuation measurements using the HDLP: (a) $n_e(t)$, (b) $T_e(t)$, and (c) $I_d(t)$ (with included uncertainties). 109
- Figure 6.9. Average axial ion transit speeds, measured versus (1D) theoretically expected values. The "error"-bars included span the 95% confidence intervals of the phase measurements and thereby indicate the level of turbulent

uncertainty in phase at each location. Data from 200 V 2 A thruster setting.....	112
Figure 6.10. Position of HDLP data collection for Sections 6.4.2 and 6.5.1.....	113
Figure 6.11. HDLP time-resolved plasma properties for a 200-V 1.5-A discharge measured 25 cm downstream from HET exit plane (aligned on thruster centerline).	114
Figure 6.12. HDLP time-resolved plasma properties for a 200-V 2-A discharge measured 25 cm downstream from HET exit plane (aligned on thruster centerline).	115
Figure 6.13. HDLP time-resolved plasma properties for a 300-V 1.5-A discharge measured 25 cm downstream from HET exit plane (aligned on thruster centerline).	116
Figure 6.14. HDLP time-resolved plasma properties for a 300-V 2-A discharge measured 25 cm downstream from HET exit plane (aligned on thruster centerline).	117
Figure 6.15. HDLP time-resolved plasma properties for a 400-V 1.5-A discharge measured 25 cm downstream from HET exit plane (aligned on thruster centerline).	118
Figure 6.16. Average ion transit velocity for 200-400V operation with 1.5-A and 2.0-A HET discharge. The linearly expanded confidence intervals contain 95% of the collected transit delay measurements suggesting either more experimental-error or more chaotic breathing mode fluctuations.....	120
Figure 6.17. Power spectral densities of plasma properties 25 cm downstream from HET for (a) 200 V 1.5 A and (b) 200 V 2 A discharge settings.....	124
Figure 6.18. Collection of planar time-averaged electron density $\langle n_e(x,y,t) \rangle$ and fluctuation average peak-to-peak electron density amplitude $\langle n_{e,pk2pk}(x,y,t) \rangle$. These averaged planar fields are computed by using all 100,000 time-resolved (with HDLP) electron density measurements obtained at each of the 352 grid points.	127
Figure 6.19. Series of time-resolved two-dimensional electron density contour maps for (a)-(c) 200 V 2 A and (d)-(f) 300 V 2 A HET discharge settings. The lower-frequency and slower-propagating breathing mode waves at 200V (18.6 kHz and 10-13 km/s) provide additional oscillation cycle detail with the 10- μ s frame-rate attained by the HDLP.....	129
Figure 6.20. 3D plot ($z = n_e$, $y =$ radial-position, $x =$ time) of radial profile transient axially travelling plasma density waves. The 31 cm wide radial profile is	

at a fixed position 25 cm axially downstream from the 200 V 2 A HET discharge exit-plane.	130
Figure 6.21. Travelling waves of plasma exhausted by a 600-W HET depicted in three simultaneously sampled signals. The upper series are of video frames acquired by the FASTCAM camera at a frame rate of 109,500 fps (with separate colormap scaling of 10-bit intensity). The middle traces (in black and magenta) show instantaneous discharge current and integrated FASTCAM frame intensity. And the lower surface plot of the electron density tracks temporally evolving waves as they propagate axially downstream from the thruster at 13 km/s. Each wave is a “breath” of xenon characteristic of the breathing mode phenomena inherent to Hall thruster operation; the breathing mode frequency for this 200-V, 2-A discharge is 19 kHz.	132
Figure 6.22. Illustration of T3 discharge channel aligned (light gray) and cluster aligned (black) plume positions examined in Figure 6.23.	134
Figure 6.23. Single-point, simultaneous plume electron density, electron temperature, plasma potential, and clustered HET discharge currents for two radial positions. (a) T3 discharge channel aligned (outer edge, away from T2) plume properties. (a) Cluster aligned properties including both separate thruster anode currents (I_{d3} and I_{d2} , gray dashed) and superimposed current ($I_{d3}+I_{d2}$, solid black).	136
Figure 6.24. Probability density for measured phase between clustered thruster oscillations. Predominate with 43% integrated probability is mode-0, with clustered thrusters oscillating in-phase.	138
Figure 6.25. Additional clustered modes identified using high-speed imaging. The same (b) all-thrusters in-phase mode-0 appears, but there exist three different modes (c)-(e) where only two thrusters are in-phase.	139
Figure 6.26. Clustered electron density contour maps of (a) HDLP time-averaged and (b) fluctuation peak-to-peak amplitude values. Both (a) and (b) are plotted on the same logarithmic colorbar scale, emphasizing the large magnitudes of the emitted density waves relative to the local DC electron density values.	140
Figure 6.27. Temporally and spatially resolved electron density contours for one (mode-0 type) breathing mode sequence. The simultaneous multi-rate signals of discharge current (sampled at 2 MHz), photo intensity (67.5 kHz), and electron density (100 kHz) are included for each time interval: (a) $t = 55.1 \mu\text{s}$, (b) $t = 65.0 \mu\text{s}$, (c) $t = 74.9 \mu\text{s}$, (d) $t = 84.8 \mu\text{s}$, (e) $t = 94.7 \mu\text{s}$, and (f) $t = 104.7 \mu\text{s}$. Colorbar (g) applies to all planar density maps.	143
Figure 6.28. 3D axial electron density wave profiles on cluster centerline ($R = 0$). The vertical axis combines all properties including: the time-resolved	

centerline electron density in blue (also colorbar scaled), separate thruster discharge currents (I_{d3} and I_{d2}), summed discharge currents ($I_{d3} + I_{d2}$), total integrated intensity ($F_{T3} + F_{T2}$), and the time-aligned FASTCAM photos. 145

Figure 7.1. Schematically exaggerated view of the electrodynamic Hall thruster breathing mode with simple scaling relations..... 148

Figure A.2. Internal view of Hall thruster cluster from within the LVTF. Cluster is mounted upon the NASA-type inverted pendulum thrust stand, near the radial center of the vacuum chamber. The seven cryogenic pumps are clearly visible. This photo was taken shortly before pumping down to vacuum conditions. 152

Figure A.3. Sample calibration of thrust stand as measured for test#1. Linear fit parameters are listed. A total of 10 points are plotted (five test masses twice sampled) but overlap quite well due to the excellent repeatability of the calibration..... 155

Figure A.4. Fixed power 600 W single thruster anode efficiency at discharge voltages ranging from 150 V to 600 V. Model data is included for qualitative comparison..... 157

Figure A.5. Fixed-power thrust-to-power trend of quasi-optimized single-thruster performance. Sample model data included for qualitative trend comparison..... 159

Figure A.6. Fixed-power anode specific impulse for quasi-optimized single-thruster. Sample model data included for qualitative trend comparison..... 160

Figure A.7. Total thrust produced by single (600 W), dual (2 x 600 W), tri (3 x 600 W), and quad (4 x 600 W) Hall thruster cluster operation. Also shown, is the sum of the thrusts collected for each of the thruster when operating alone (un-clustered). The clustered total thrust exceeds the sum of the non-clustered individual thrusts in all cases..... 162

Figure A.8. Anode efficiency for various clustered configurations. The single thruster data represent the mean anode efficiency computed from separate experiments with each of the four thrusters at the three discharge voltages shown. 166

Figure A.9. Thrust-to-Power ratios plotted against anode specific impulse for all clustered configurations. The single thruster data represents the mean T/P_D computed from separate experiments with each of the four thrusters. ... 166

List of Tables

Table 2.1. Measured performance for nominal 600 W thruster operating conditions.....	16
Table 2.2. High-speed DAQ system specifications.	23
Table 3.1. Specifications of the probe bias amplifier design for the HDLP.....	34
Table 3.2. Specifications of the dual-symmetric current sensing circuit designed for the HDLP.	40
Table 4.1. Tabulation of Langmuir probe frequency sweep limits for typical Hall effect thruster and Tokamak conditions (near-wall and Scrape Off Layer (SOL) conditions are common Langmuir probe-able regions while the core is too hot to probe but included to show continued trends).....	72
Table 6.1. Tabulation of time-averaged and fluctuation standard deviation plasma properties 25 cm downstream (on thruster centerline) of a 600-W HET.	121
Table A.1. Gain in thrust due to clustering Hall thrusters for three discharge voltages.	162
Table A.2. Estimation of facility-effect-thrust for clustered HETs.	164

Abstract

The existence of plasma oscillations in the near and far field discharge of a Hall effect thruster alters the conventionally held view of their operation as steady electrostatic propulsion devices. Indeed, the consequences from fluctuations in ionized propellant density, temperature, and potential may include increased thrust, exacerbated engine erosion, and spacecraft interference. In this work, the unsteady nature of a Hall effect thruster discharge is investigated via two-dimensional, time-resolved plasma measurements. A novel dual Langmuir probe diagnostic is developed to enable an unprecedented temporal resolution for electrostatically acquired plasma properties near the upper theoretical limits of this probe. Observations of large amplitude transient oscillations caused by the Hall thruster breathing mode are seen for all thruster conditions at all spatial locations and in all measured plasma properties including: discharge current, electron density, electron temperature, and plasma potential. A unique method of spatiotemporal data fusion facilitates visualization of two-dimensional time-resolved planar plasma density contour maps is also developed where discrete turbulent bursts of plasma are tracked as the thruster exhales breaths of ionized propellant at velocities in excess of 12 km/s. This time-resolved investigation of the plasma downstream from a Hall thruster unveils an environment rich in oscillatory behavior dominated by the Hall thruster breathing mode. These insights emphasize the importance of time-resolved plasma measurements and, through enhanced understanding of the discharge process,

may ultimately lead to improved thruster designs that work in concert with plasma fluctuations to achieve enhanced performance.

Chapter 1

Introduction

To begin this work, this chapter serves to briefly introduce the concept of electric propulsion, describe the basics of the particular type of propulsion used in this dissertation, and—by briefly exploring the relevant theoretical plasmadynamics—impart the need for time-resolved measurements when developing and understanding advanced plasma based thrusters. Next, in Chapters 2 and 3, the experimental setup and unique high-speed dual Langmuir probe are detailed with an outline of the probe theory and temporal limits. Then in Chapter 5, a unique method of data fusion is developed for use in combining data that spans the dimensions of time and space. Finally, in Chapter 6, a wide collection of temporally and spatially resolved results are presented and discussed with an overall summary (and a future work section) concluding this dissertation in Chapter 7.

1.1 Electric propulsion

The use of electric and magnetic fields to transfer momentum between a device and its environment is termed electric propulsion. In the context of space-based electric propulsion systems, electric and magnetic fields are applied to propellant particles, bestowing acceleration to the particles that is balanced in the production of thrust. The various methods by which electric and magnetic fields can accelerate matter are categorized into three major groups: electrothermal, electrostatic, and electrodynamic. A

number of texts have been written over that last 40 years that explore these types of electric propulsion systems [1, 2, 3] and the interested reader is encouraged to see these works for common configurations and the *accepted* physics governing these types of electric propulsion systems. However, the enormous effort of presently ongoing research in this field is evidence of a significant amount of untried concepts and governing physics of many devices that is still not fully understood.

By deriving propulsive energy from stored electrical reserves, the propellant acceleration for an electric thruster is nearly unlimited and exhausted propellant velocities in excess of 100 km/s are not difficult to attain with modern electric thrusters. In chemical-based rockets, the highest attainable exhaust velocities (U) are limited to about 5 km/s. Since thrust is defined as the changing rate of the system momentum,

$$T \equiv \frac{d}{dt}(mU) \quad (1.1)$$

the per particle (of mass m) thrust advantage of electrically accelerated matter versus chemical accelerated matter is obvious. The metric used to define the per mass effectiveness of a given propulsion system is the specific impulse, defined in Eqn. (1.2) :

$$I_{sp} \equiv U/g_o \quad (1.2)$$

With this terminology, the effectiveness of a given I_{sp} to increase the velocity (ΔU_{pay}) of a given payload (M_{pay}) by expending a given propellant mass (M_{prop}) is computed by integrating the thrust definition above:

$$\Delta U_{pay} = I_{sp} g_o \ln \left(\frac{M_{pay} + M_{prop}}{M_{pay}} \right) \quad (1.3)$$

Known as the "rocket equation," first derived by K. E. Tsiolkovsky in 1903, Eqn. (1.3) shows that a given fractional increase in I_{sp} provides a greater payload velocity increment than the same fractional increase in propellant mass. This relation led to the use of staged rocket systems that enabled humankind to enter the space age. And today, the advantageous mass savings with high- I_{sp} electric propulsion systems is being exploited for use in earth-orbiting satellite station-keeping as well as interplanetary and deep space exploration by NASA, the Russian Federal Space Agency, the ESA (European Space Agency), and others. The use of electric propulsion on earth-orbiting satellites can prolong their operational lifetimes (for a given propellant mass fraction) and, besides the obvious economic advantages, this could help curb the littering of low-earth orbit (presently orbiting objects—mostly expired satellites and assorted parts—is shown in Figure 1.1).



Note: Artist's impression; size of debris exaggerated as compared to the Earth

Figure 1.1 The beehive of known objects in Low-Earth Orbit (LEO). The finite propellant reserves of all satellites limit their operational lifetimes after which they often become debris littering LEO (ESA image 2008).

1.2 Hall Effect Thrusters

One type of electric propulsion device, in use by many presently earth-orbiting satellites, is the Hall Effect Thruster (HET), with over 250 thrusters launched into orbit since 1971. [4, 5] Originally developed in the former Soviet Union, these devices rely on both magnetic and electric fields to achieve efficient ionization and acceleration of a relatively dense (compared to ion thrusters with similar efficiencies) plasma exhaust. Schematically this configuration is described in Figure 1.2.

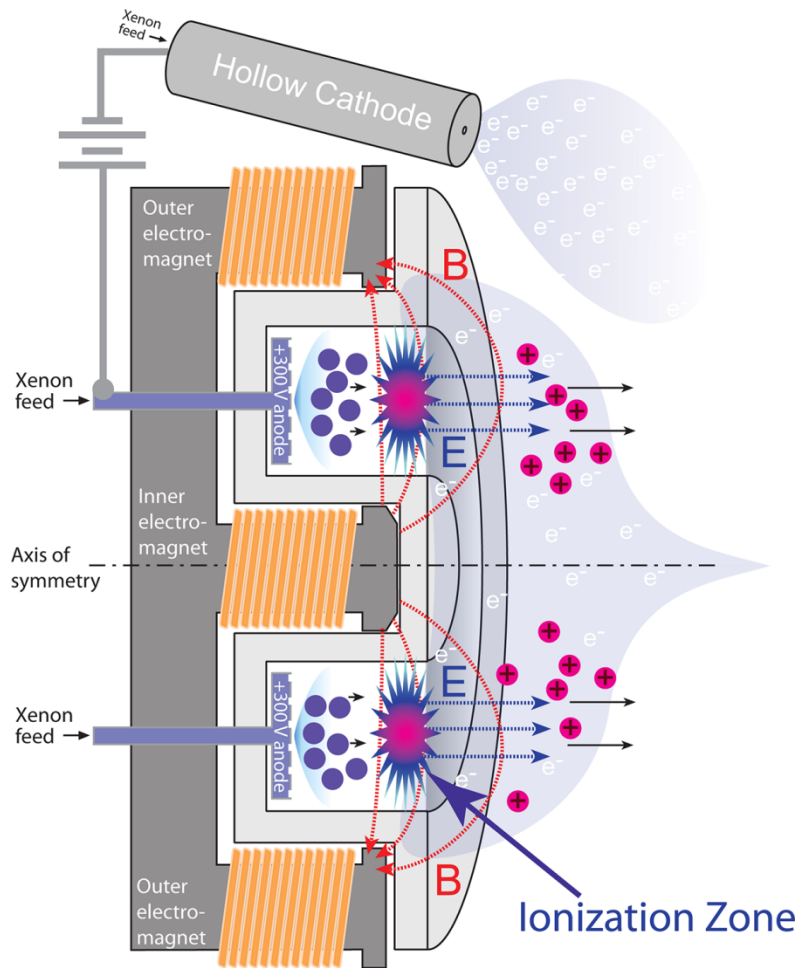


Figure 1.2. Schematic of Hall Effect Thruster (HET), cross-sectional view showing half the annular discharge channel lined in high-temperature compatible dielectric.

Conventionally categorized as an electrostatic form of electric propulsion (EP), the integral use of both electric and magnetic fields has led to some placing the device in the electromagnetic family of EP. Indeed, as the results of this dissertation shall make clear in later chapters, the dynamic nature of a HET discharge leaves few properties, if any, as "static." The magnetic-layer variety of Hall thrusters (also called stationary plasma thrusters) possess discharge channel walls lined in an insulating (electrically and thermally) layer of refractory low-ablation ceramic such as boron nitride (BN), borosil (BN-SiO₂), or alumina (Al₂O₃). The full influence of these walls on the internal

discharge physics is still not fully understood and different choices of wall materials has been shown to have a dramatic impact on discharge efficiency, fluctuations, electron conductivity, and thruster lifetime. [6, 7, 8]

1.3 Hall Thruster Clustering

As worldwide telecommunication demands increase, so too do the satellites that support these growing networks (e.g. in the U.S., 30% of TV service subscribers use satellite service (70% use cable) in 2009 versus just 6% in 1999 [9]). The development of comparably higher power Hall thrusters is following suit. The large solar arrays donned by modern telecommunication satellites, the high power-density (< 1 kg/kWe, kg/kW-electrically-generated) nuclear We to MWe power sources of future NASA missions [10, 11], along with increased satellite maneuverability demands from the Air Force [12], altogether represent the growing demand for an effective and efficient means of electrically propelling these large spacecraft. The aforementioned performance characteristics of modern Hall thrusters places them as a leading electrical spacecraft propulsion candidate for the growing base of applications thus discussed. Yet, the ground based testing of high power Hall thrusters has limits imposed by the difficulty in maintaining a space-simulating high-vacuum pressure (1×10^{-5} torr or lower) at the high mass-flowrates required to maintain the high power discharges [13]. Thus, interest has grown in the use of multiple Hall thrusters clustered together as a means of achieving greater overall thrust while still retaining the excellent performance characteristics of a single Hall thruster; one with moderate enough power to have undergone complete ground-based testing and development with coexisting vacuum chamber facilities.

In general, a cluster of thrusters totaling a given high-power level (e.g. 200 kW) will result in lower thrust efficiency, higher system dry-mass, and shorter lifetime than a single (monolithic) larger thruster of equivalent power. Yet, the advantages of a N-thruster clustered approach include: N-1 system redundancy, N-step fully optimized throttability, and cheaper system development. Indeed, the recent JAXA (Japan Aerospace Exploration Agency) asteroid explorer Hayabusa, launched with a 4-thruster cluster of ion engines, has managed to nearly complete its asteroid sample-return mission—beleaguered by multiple EP engine failures—thanks to clustered redundancy.[14, 15]

1.4 Myriad of Plasma Oscillations in Hall thrusters

Arising from the myriad of electromagnetic interactions between excited propellant particles, electrons, and the imposed magnetic and electric fields, HET plasmas are rich with oscillation in a wide band ranging from 1 kHz to 20 GHz. [16, 17] While limited, prior measurements of electric propulsion plasma oscillations do exist. Much of this work has focused on single-point (or two-point) floating and fixed-bias probe measurements. [18, 19, 20] These measurements have confirmed the presence of oscillations within the plasma, but with limited quantitative value, often just the variation in the floating potential or ion saturation current of the plasma. The few somewhat detailed measurements [21] suffer from use of a discharge current oscillation phase alignment technique (to reconstruct I-V curves) that, in its implementation, is physically invalid for the turbulent form of the fluctuations observed. While natural plasma oscillations and relaxation cycles can appear somewhat sinusoidal, the usage of phase averaged I-V methods (that are quite common for measurements in pulsed plasmas [22])

requires a fixed-frequency oscillation to reference phase with, and the spectral form of natural oscillations are usually quite broadband (e.g. turbulent). [16]

Also, while various theories regarding many of these oscillation modes have been presented [16, 23, 24, 25, 26] there is still a lot of physics involved in these modes that is not well understood. Choueiri's review [16] of the many oscillations observed in HETs evaluated (with various dispersion theories and experimental observations) an assortment of possible modes due to gradients, drift-type instabilities, ionization instabilities, transit-time oscillations, and other mechanisms. The resulting consensus of all the prior research on HET oscillations implies a plasma rich in azimuthal (about the thruster axis of symmetric) and axial oscillations (along the axis of symmetry).

However, high-resolution, spatially and temporally resolved measurements of Hall thruster plasma property oscillations, are absent from the literature and one of the central goals of this dissertation is to fill that gap; providing a detailed and completely time-resolved view of the plume field created by the operation of a Hall effect thruster.

1.5 Breathing Mode Oscillations

One of the lowest-frequency modes that is observed ubiquitously in the operation of HETs is the Hall Thruster breathing mode. This "breathing" mode (first labeled by Boeuf and Garrigues [24]) has been referred to in early Russian literature as an "instability of location of the ionization zone". [27] Although low in frequency, the breathing mode is often the largest (by orders of magnitude [16]) oscillation observed in a HET plasma. Breathing mode oscillations develop in the thruster discharge channel where the ionization-zone and neutrals engage in a "predator-prey" oscillatory behavior.

The cycle starts as the channel fills up with neutrals. Next, the Hall current (with maximum current density near the peak radial magnetic field) begins to ionize the neutrals. As the ionized-neutrals depart, they leave behind electrons that can contribute to the Hall current or anomalously approach the anode. The additional electrons that remain in the closed-drift orbit cause the electric field (between the anode and Hall current) to increase in order to maintain current continuity. This increases the $E \times B$ drift magnitude and results in a temporally enhanced ionization rate. However, the ionization burst rapidly depletes all the neutrals throughout most of the discharge channel. Following this, the discharge channel then begins to refill with neutrals and the cycle repeats.

The role of these oscillations has been thought by some researchers to be negative, and the very large amplitudes (often on the order of the mean value) of these oscillations can indeed lead to violent conditions that could potentially damage the thruster discharge supply. Yet, as was realized by their original Russian developers, these oscillations may "provide the necessary electric conductivity for operation [and] this type of oscillation can be considered as useful or normal." [27]

1.6 Simple Breathing Mode Model

A simple physical model for breathing mode oscillations was presented by Fife [23] and is briefly outlined. Invoking species conservation, by considering an ion source (and neutral loss) with an electron-neutral ionization collision rate, ξ_i , and an electrostatically driven convective loss of ions (and injected source of neutrals), Eqn. (1.4) is obtained.

$$\begin{aligned}\frac{\partial n_i}{\partial t} &= n_i n_n \xi_i - n_i \frac{U_i}{L_i} \\ \frac{\partial n_n}{\partial t} &= -n_i n_n \xi_i + n_n \frac{U_n}{L_i}\end{aligned}\tag{1.4}$$

In this equation an ionization zone length, L_i , has been introduced to evaluate the problem in a simple one-dimensional manner (in the axial direction of the electric field that ejects the ions at velocity U_i ; with neutrals entering at velocity U_n). Also, the ion and neutral densities are included as n_i and n_n respectively. The ionization rate, ξ_i , is in general a function of temperature and other parameters, but neglecting these dependencies and linearizing this equation using density perturbation of the convention form (time average, " $\bar{\quad}$ " plus fluctuation, ' \prime '):

$$\begin{aligned}n_i &= \bar{n}_i + n_i' \\ n_n &= \bar{n}_n + n_n'\end{aligned}\tag{1.5}$$

Using Eqn. (1.5) in Eqn. (1.4) and taking only zeroth-order terms, the following balance of loss and source terms is seen (this is just the DC solution of Eqn. (1.4)):

$$\begin{aligned}\xi_i \bar{n}_i &= \frac{U_i}{L_i} \\ \xi_i \bar{n}_n &= \frac{U_n}{L_i}\end{aligned}\tag{1.6}$$

However, by taking the first order terms and then combining the resulting equations into a single expression, one obtains:

$$\frac{\partial^2 n_i'}{\partial t^2} + \xi_i^2 \overline{n_i n_n} n_i' = 0\tag{1.7}$$

Fife identified this as an undamped harmonic oscillation equation, with a frequency of ion density (n_i') oscillation of simply $\omega^2 = \xi_i^2 \overline{n_i n_n}$, and by using Eqn. (1.6):

$$f_B = \frac{\sqrt{U_i U_n}}{2\pi L_i}, \quad (1.8)$$

where f_B is the thruster breathing mode frequency. Thus, the breathing mode of a thruster appears to depend on the ion and neutral velocities as well as the length of the zone of ionization. While relatively simple in form, and often in fair agreement with experimental data, the accuracy of Eqn. (1.8) should diminish for large ion density fluctuation amplitudes. Also, the ways in which the various parameters of this expression vary at different thruster operation conditions (e.g. mass flow rates, discharge voltages and currents, as well as magnetic field settings) are not addressed with this simple form.

1.7 Plasma Fluctuations and Anomalous Transport

In the plasma modeling community, it was recognized early on that electrons do not always stay confined to magnetic field lines as they "classically" should. In 1949, Bohm proposed the now commonly employed "Bohm" mobility for electrons, which scales with $1/B$ (with B as the magnetic field strength). Compared to the classical $1/B^2$ scaling, this Bohm mobility was able to explain large cross-field electron currents observed in fluctuating plasma environments. While Q-machines (quiescent plasma devices) tend to exhibit classical electron conduction perpendicular to the magnetic field that scaled as $1/B^2$, noisier plasmas did not. [28] The presence of turbulent oscillations within the magnetized plasma is thought to provide a mechanism for this anomalously large cross-field electron transport. Indeed, a great deal of effort is put forth in the fusion plasma community to measure and understand turbulent transport processes. [29, 30] The theory of turbulent plasma transport is complex and well out of the scope of this

work, yet to provide some sustenance to the concept, the following turbulent cross-field flux expression is included: [31]

$$\Gamma_x = \frac{1}{B_r} \langle \tilde{n}_e \tilde{E}_\theta \rangle \quad (1.9)$$

This flux (in SI units of electrons $\cdot \text{m}^{-2} \cdot \text{s}^{-1}$) occurs for a radial magnetic field direction as drawn in Figure 1.2 and azimuthal electric field fluctuations, \tilde{E}_θ , (about the thruster axis of symmetry). This equation is derived from the first order terms for an $E \times B$ drift with a fluctuating electric field. If the density fluctuations, \tilde{n}_e , are out of phase with those in the electric field (or if the density is not fluctuating), then zero net cross-field transport is established. However, when the density and electric field fluctuate with some phase other than 180° , then a net cross-field flux will be set up. In a famous work by Janes and Lowder [20], time-resolved measurements of ion saturation (roughly $\propto \tilde{n}_e$) current and hot filament probe potentials (roughly $\propto \tilde{E}_\theta$) confirmed the presence of a finite phase difference that would lead to anomalous electron transport inside the Hall thruster discharge channel examined.

Today, plasma modelers employ a combination of Bohm transport and another anomalous transport process referred to as near wall conductivity. [32] It is likely that both types of anomalous transport exist and this is a subject of much ongoing research to further understand the intricacies of how to correctly model this transport. [33, 34, 35]

Chapter 2

Experimental Apparatus

All experimental data in this work was collected at the University of Michigan's Plasmadynamics and Electric Propulsion Laboratory, utilizing the Large Vacuum Test Facility (LVTF). An internal vacuum chamber view of the setup used to collect the data presented in this dissertation is shown in Figure 2.1

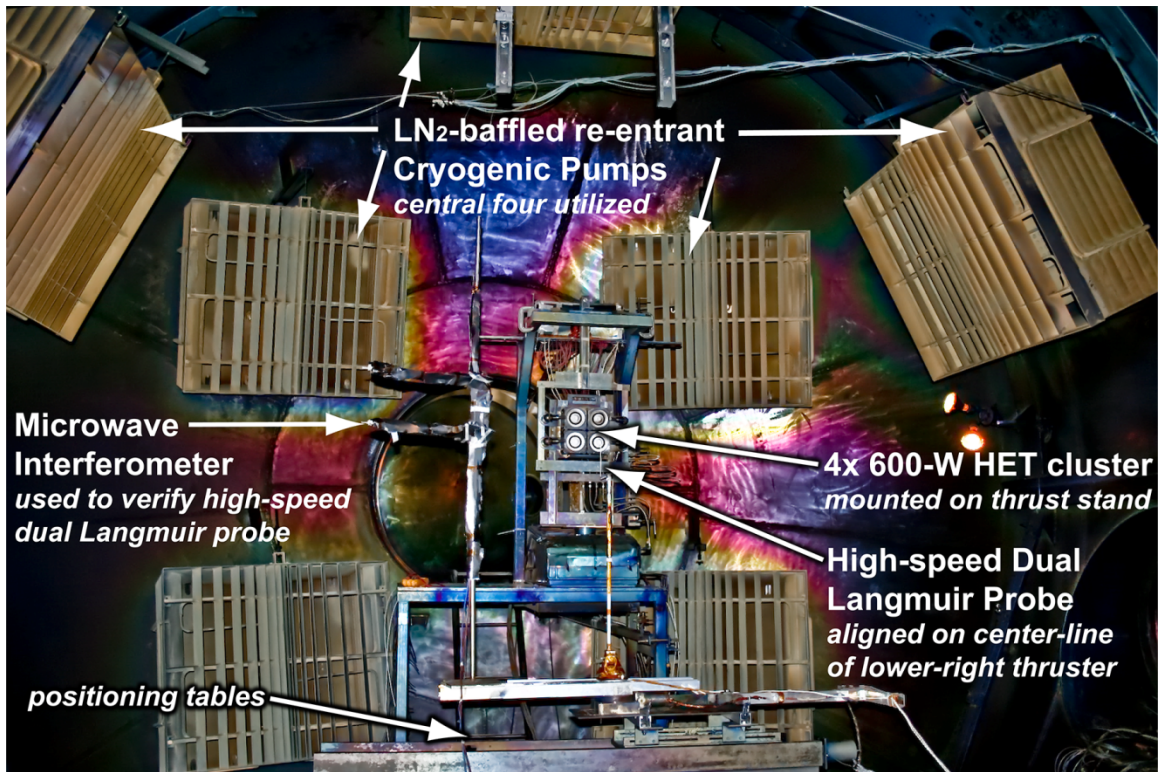


Figure 2.1. Two-by-two 600-W Hall thruster cluster mounted inside LVTF. The 100-kHz dual Langmuir probe (HDLP) is positioned 10 cm downstream from Thruster3 (T3, the lower-right thruster) upon a pair of remotely controlled positioning tables.

2.1 Large Vacuum Test Facility

The LVTF is a cylindrical stainless steel clad vacuum chamber measuring 6 meters in diameter and 9 meters in length. Four 400-CFM mechanical pumps along with two 2,000-CFM blowers serve to evacuate the chamber to a rough vacuum pressure of about 60 mtorr. A high-vacuum base pressure (P_{base}) of less than 3×10^{-7} torr is attained by operating the seven liquid-N₂ baffled CVI TM-1200 re-entrant cryopumps with an aggregate pumping speed of 240,000 liters/sec on xenon. Two hot-filament cathode ionization gauges (Varian models 571 and UHV-24/nude-gauge) are used to measure the chamber pressure (as $P_{ioniz.gauge}$), which is corrected for the propellant gas (typically xenon or krypton) using

$$P_{corr} = \frac{P_{ioniz.gauge} - P_{base}}{2.87} + P_{base} \quad (2.1)$$

The gas-corrected chamber pressure, P_{corr} , in this expression uses the numerical gas specific constant of 2.87 for xenon, and pressure units of torr. For the bulk of the data presented, only four of the seven available cryopumps were in use, and for single thruster operation the pressure was $P_{corr,4cryos} \approx 7 \times 10^{-6}$ torr (with about $\pm 50\%$ gauge uncertainty). The single thruster pressure with all cryos in operation was measured as $P_{corr,7cryos} \approx 3 \times 10^{-6}$ torr. The pressure at the edge of space (100 km altitude Kármán line) is approximately 4×10^{-3} torr, and in the low-earth orbit of the international space station (320-350 km) the pressure ranges $0.02-0.1 \times 10^{-6}$ torr. [36] The internal volume and high-vacuum features of the LVTF provide an excellent simulation of the space environment where the Hall thrusters used in this study nominally operate. While the majority of HETs are currently in use for GEO station keeping (where the pressures are below 10^{-10}

torr), there is growing interest in using these devices at lower orbits for atmospheric drag compensation and LEO to GEO transfers. [37]

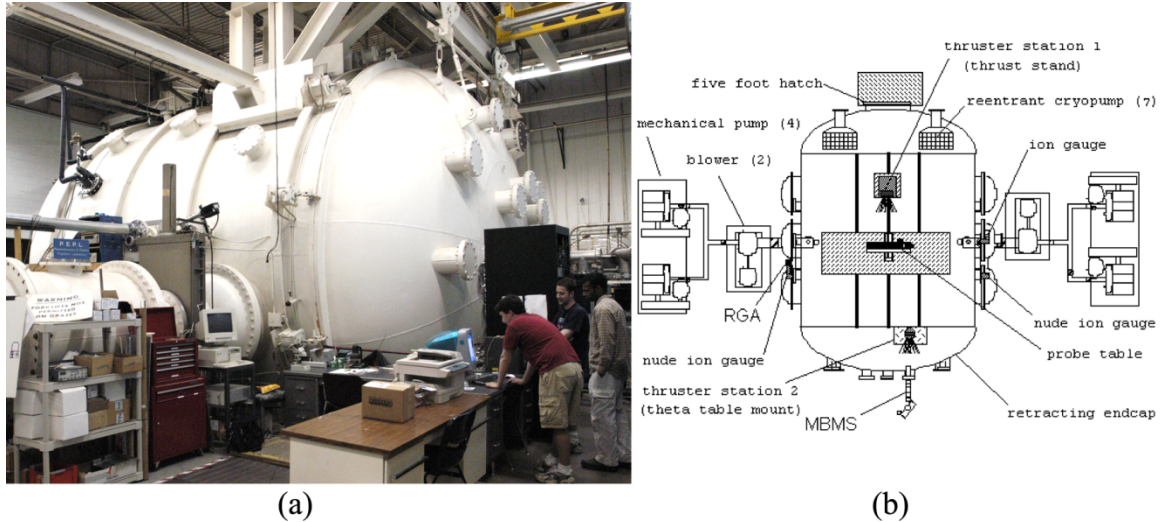


Figure 2.2. The Large Vacuum Test Facility (a) external photographic view and (b) top down schematically view.

2.2 Low-power 600-W Hall thruster cluster

A cluster of four identical 600 W Hall thrusters is utilized for these experiments. The cluster was obtained by the University of Michigan's Plasmadynamics and Electric Propulsion Laboratory (PEPL) in 2003 for testing the effects of operating clusters of Hall thrusters. Prior research performed at PEPL and the Air Force Research Lab (AFRL) [38, 39, 40] with a similar cluster of four 200 W Busek BHT-200-X3 Hall thrusters provided a wealth of insight into the plume effects from clustering and led to the work with the 600-W cluster used in this research. Pre-existing data for the performance from a cluster of four Hall thrusters had never been published (at least as far as could be determined; however, sparse data does exist for dual- [41] and tri- [42] thruster clusters), thus performance measurements for this new cluster were carried out inside the LVTF and are detailed in Appendix A. The precise measurement of sub-milli-Newton

resolution thrust levels from even a single thruster is a challenging task. Clustering four Hall thrusters together adds a great deal of complexity to the endeavor; since four times as many flow and electrical lines are required. Perhaps this explains the lack of prior research. Whatever the case, this research is crucial to quantifying and understanding the effects of clustering Hall thrusters—as such configurations will inevitably be required to propel future spacecraft—and ground-based testing facilities will not exist with the capacity to test fully clustered high-power Hall thruster configurations. The cluster used in this study is moderately low-power; at 600 Watts per thruster, the full cluster of four thrusters consumes a mere 2.4 kW of electrical power. Ground-based measurements from Hall thrusters powered in excess of 20 kW [43] are relatively uncommon, but lower-power level thrusters (~5-6 kW) are routinely tested. Therefore, this cluster and the individual hall thrusters are quite suitable for use in this study because they are unlikely to encounter vacuum pumping issues.

Table 2.1. Measured performance for nominal 600 W thruster operating conditions.

Nominal 600-W Thruster Performance	
Discharge Voltage, V_D	300 V
Average Discharge Current, I_D	2.01 A
Inner & Outer Magnet Current, $I_{IM\&OM}$	2.00 A
Anode Mass Flowrate, \dot{m}_a	2.47 mg-Xe/sec
Thrust, T	41.5 mN (± 1 mN)
Anode Efficiency, η_a	57.9% ($\pm 2.8\%$)
Anode Specific Impulse, $I_{sp,a}$	1715 sec (± 44 sec)
Thrust/Power, $T/(I_D V_D)$	69 mN/kW

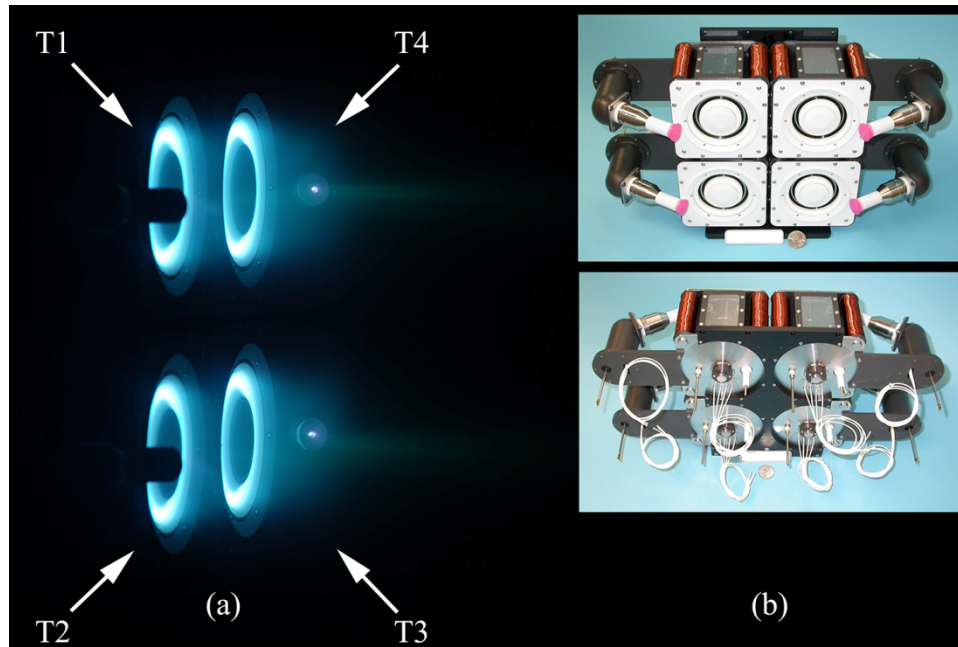


Figure 2.3. Cluster of four 600 W Hall thrusters (with labels) discharging (a) in the LVTF. Inset (b) shows pre-operational front and rear views of the cluster.

Each 600 W thruster has a discharge channel mean diameter of approximately 5 cm and the thruster centerlines are separated by 11 cm in both the vertical and horizontal arrangement within the cluster. Inner and outer electromagnets run at 2-A each for nominal conditions. Table 2.1 lists the nominal performance measured (at PEPL) at 600 Watts ($V_D = 300$ V, $I_D = 2.01$ A, $\dot{m}_a = 2.5$ mg/sec) for a single 600-W Hall thruster (see Appendix A). [44]

Each thruster is equipped with a 6.25-mm hollow cathode mounted at a 45° angle to the anode plane (as in Figure 2.3). The entire cluster unit is a flight-qualified like design, and appears to have a magnetic circuit and anode distributor optimized for a 2 A discharge current, as is shown in Appendix A. This challenges thruster optimization at off-design discharge currents. The thrusters are numbered sequentially in a counter-

clockwise manner beginning with the upper left thruster (T1) as viewed when looking into the discharge channel.

A dedicated set of five commercial Sorenson switching-based power supplies are configured to operate each of the four thrusters (for a total of 20 power supplies): discharge (400-V 5-A, DHP400-5), heater (40-V 15-A, DLM40-15), keeper (600-V 1.7-A, DCS600-1.7E), inner magnet (60-V 10-A, DLM60-10), and outer magnet (DLM60-10). No current filtering is applied to the discharge supplies. Xenon flow is similarly controlled independently for each Hall thruster within the cluster, using commercial UNIT (UFC-7301) mass flow controllers (MFCs) calibrated for Xenon: 40 sccm-Xe max for anodes and 10 sccm-Xe max for cathodes. All eight MFCs are digitally controlled with a central LabView interface, and 10-channel UNIT MFC power supply. Digital control of the volumetric flowrate enables enhanced accuracy of $\pm 1\%$ of the set-point for most of the MFC's specified range. A Humonics OptiFlow 570 Digital Flowmeter (bubble-meter) was used to calibrate each of the Anode MFCs using both Nitrogen (with manufacturer supplied N_2 reference flowrates) as well as xenon. After applying the appropriate temperature correction to the bubble-meter flowrates (at ambient temperature of 25.5°C) to compute the effective standard flowrates (standard conditions: 101,325 Pa and 0°C) excellent agreement was observed throughout the full range of all four anode MFCs. All measured flowrates lay within the nominal error bars ($\pm 1\%$) of manufacturer supplied MFC calibrations (with both N_2 and Xe); therefore the factory calibrations were left unchanged (see Figure 2.4).

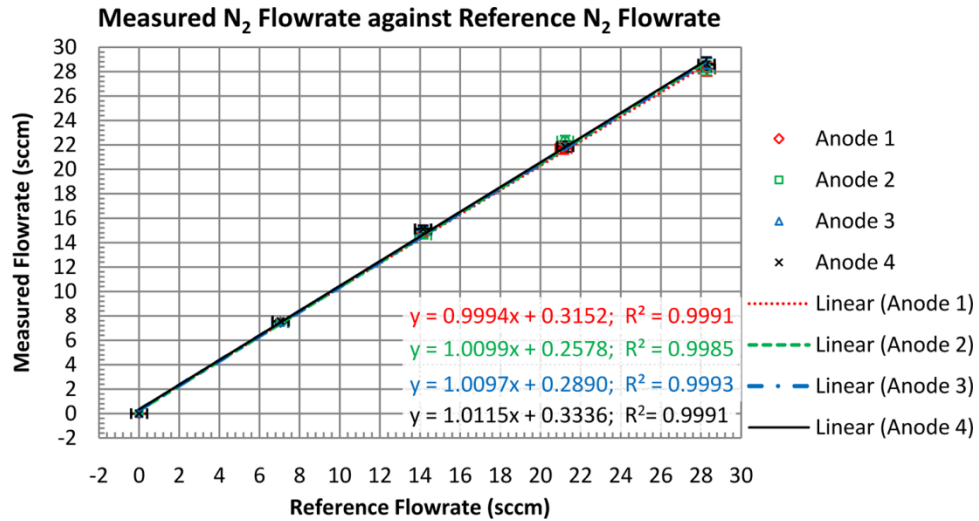


Figure 2.4. Flowrate calibration for the four 600-W HETs compared to the nitrogen reference specifications of each MFC.

2.3 Automated Tables

A pair of remotely controlled stepper-motor driven axial and radial motion tables performed positioning of the probes used in this research (see Figure 2.5). Overall motion ranges for the radial and axial tables were 1.4 m and 0.8 m respectively, with absolute positional accuracy of $\pm 150 \mu\text{m}$. A dedicated PC was used to command the table motion with a LabView program. While the entire range of the table allowed motion, 1.4 m by 0.8 m, was intended to be used as the data boundaries for the planar data collection grid, a reduced grid space measuring 0.5 m by 0.31 m was instead utilized for data collection. The reason for the smaller grid space was threefold. First, due to the large drop-off in plasma density that occurred at the edges of this boundary, the corresponding low signal-levels would be problematic to process. However, this effect was anticipated, and another set of circuit components was designed to handle this lower-current range. Secondly, repeatability issues were identified with motion accuracy of the tables near the edges of their motion ranges. A reduced range of motion was tested and performed with 100% repeatability (e.g. no missed motion command steps). Lastly, to

reduce the data collection time (to about 3 hours per condition) as well as aid in simplifying the data collection, fixed grid spacing of 10 mm radial and 50 mm axial was selected. These resolutions provide decent near-field radial resolution (thruster diameter ≈ 5 cm) and acceptable axial resolution given the expected axial plasma flow velocity at > 10 km/sec. The overall collection region measuring 50-by-31 cm resulted in a grid with 352 distinct points. Software delays were included in the table motion control to allow for vibrations to dampen (2.5 sec) and for the DAQ system to complete its data collection (1 sec of 2 MHz analog-to-digital conversions and 5 sec for writing a 32-MB file at 7 MB/sec hard drive speeds). The added delays together with the time required to move the tables (maximum speed of 1 mm/sec) resulted in an overall time of 3.5 hours to collect data from all grid-points. Thankfully, the entire data collection was fully automated, but even so, this length of time made large datasets (with more than 352 points) prohibitive.

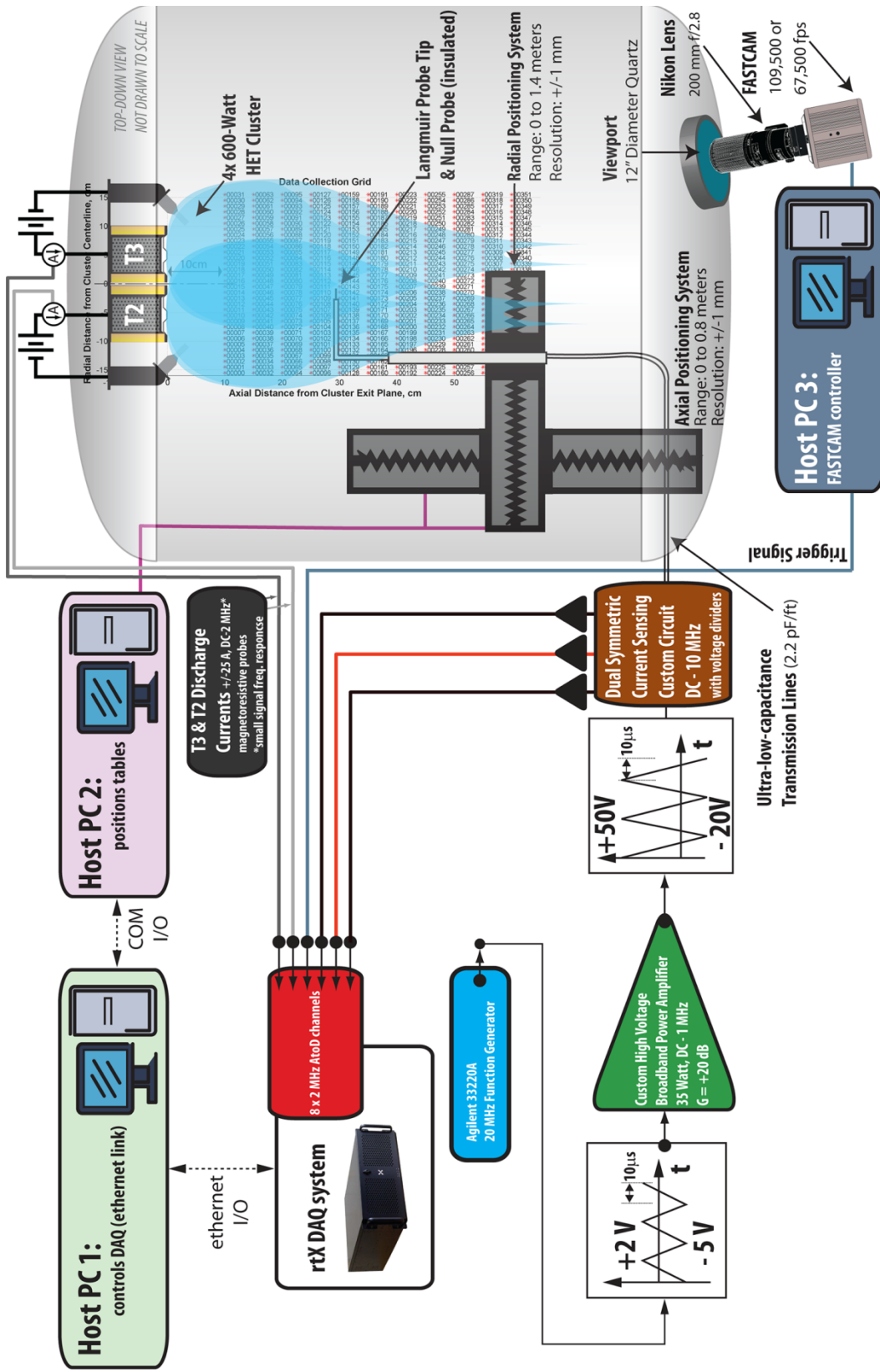


Figure 2.5. Overview of experimental setup including: HET cluster, LVTF, 100-kHz HDLP system, FASTCAM, motion control, ADC system, and integration of all subsystems through various digital input/output (I/O) interfaces.

2.4 FASTCAM: High-Speed Video System

Motivated by prior research of HETs with optical diagnostics [45, 46, 47, 48, 49], a Photron FASTCAM-1024PCI high-speed camera was employed to image the thruster discharge with high-framerate video. For selected thruster operating conditions, the FASTCAM was synchronized and operated simultaneously with the HDLP test setup. Imaging occurred at the highest two framerates: 109,500 fps (frames/sec), for single thruster cases, and 67,500 fps for clustered cases. The FASTCAM video Nyquist frequencies of 55 kHz and 34 kHz were higher than the thruster breathing modes of interest therefore ensuring their un-aliased capture. Unfiltered, monochromatic images of the thruster(s) were taken through a downstream quartz viewport. The 10-bit, raw camera files were exported to Tagged Image File Format (TIFF) for image post-processing. The lack of spectral-line-filtered and non-calibrated CCD spectral response limits the FASTCAM images collected in this setup to qualitative measurements. Even with this limitation, the high-speed imaging system proved a valuable diagnostic tool that provided an independent validation of the High-speed Dual Langmuir Probe (HDLP) system developed for this research.

2.5 High-Speed DAQ System

Capturing entire I-V curves at 100 kHz continuously requires a robust Data Acquisition (DAQ) system able to sample analog signals considerably faster than this rate. A specially designed DAQ system, (rtX, built by Applied Dynamics International (ADI)) was obtained to meet the data acquisition requirements of this experiment. Consisting of eight independent 16-bit analog-to-digital converters clocked synchronously at 2 MHz, with dual-core 2.4-GHz Opteron processors that control FIFO

buffers, triggering, and ethernet I/O—this system can sample seamless records in excess of 80-million samples. The high-speed and high-resolution 16-bit analog-to-digital converters (ADCs) allow for a theoretical signal-to-noise ratio, SNR, of 90 dB. Yet any physical analog signal contains noise, and a simple loop-back experiment between the DACs and ADCs yielded a SNR of 82.3 dB—very close to the manufacturer’s quoted value.

Table 2.2. High-speed DAQ system specifications.

rtX High-Speed DAQ Specifications	
Analog input rate per channel	2 MHz
Number of channels	8 indep. analog inputs, 4 analog outputs, 4 digital I/O
Resolution	16 bits
SNR (analog inputs)	82 dB (quoted, 82.3 dB measured)
Voltage ranges	± 10 V, ± 5 V, and ± 2.5 V
Overall accuracies	± 5 mV (for ± 10 V range) and ± 2 mV (for ± 5 V range)
Hard-disk capacity	136 GB (100 GB dedicated for data storage)
Processors	2 x 2.4-GHz Opteron CPUs & 66-MHz DAQ controller
Communication	2 x Ethernet (100 Mbps)

This robust DAQ system provided high-speed, high-SNR, simultaneous multi-signal, and large sample-set measurements that vastly exceed what a laboratory oscilloscope or more typical (and less capable) DAQ system could provide. This feat is made clear in an examination of previous high-speed plasma studies (Section 3.2). While systems with faster rates of raw analog DAQ presently exist (with otherwise similar specifications), the first 16-bit high-frequency (> 100 MHz) analog-to-digital converters have only recently been developed (16-bits 105-MSPS first introduced in 2003 by Analog Devices AD10678 chip). [50]

The rtX system runs the QNX real-time operating system for efficient multitasking and multithreading required to ensure hard real-time performance. A host-PC running

ADI's software packages (ADvantageVI and ADvantageDE) provides a user interface to the rtX DAQ hardware. This software allows one to define all the DAQ settings including: sample-rates, DAC output waveforms, voltage input ranges, and many other parameters. Custom drivers were also developed by ADI for this project, allowing sampling of four of the analog inputs each at 2 MHz while maintaining a set of four digital-to-analog output signals. Computer programming (in C) is used to command the DAQ system in real-time and is used in this experiment primarily to trigger data acquisition and data-set file naming. Upon a digital request for data acquisition, the A-to-D channels ch0, ch1, ch3, and ch4 begin streaming samples into rtX RAM until the stop command is issued. Up to ten seconds of analog input data may be collected continuously in this manner (limited by the system memory). Once the ADCs are stopped, the C code writes the collected data values from RAM to a local hard drive on the rtX. The local hard disk for DAQ storage contained 100 GB of free space, and a full set of data at all grid-points from the grid shown in Figure 2.5, consumed 11 GB. Five completed runs (each lasting 3.5 hours) needed to be thrown out due to triggering failures (random loss of data due to noise in the COM/communication line from the PC running LabView) and table positioning errors, both of which were later addressed. Five full data sets were collected without any issues, and were taken with three separate HDLP sweeping frequencies (100 Hz, 50 kHz, and 100 kHz) as well as a variety of thruster operating conditions and clustered configurations. The slow data at 100 Hz is free of any stray capacitance or other defects and was used to provide a "DC" measurement of the plume properties using traditional Langmuir probe analysis. The 100 kHz data contain a probe bias sweep every 10 μ s and this is the data focused on in this work. The 50-kHz

data were acquired as a backup for the faster 100-kHz data since it was not yet certain there would be a sufficient number of data points in every I-V trace (with 10 μ s of 2 MHz acquisition only twenty distinct points are collected per trace). Indeed, the results of this study demonstrate that the faster 100 kHz I-V traces contained enough points for proper HDLP analysis (as shown in Chapter 3 and Chapter 4).

Chapter 3

High Speed Dual Langmuir Probe

In an effort to temporally resolve the electron density, electron temperature, and plasma potential for turbulent plasma discharges, a unique High-speed Dual Langmuir Probe (HDLP) has been developed. [51] A traditional single Langmuir probe of cylindrical geometry (exposed to the plasma) is swept simultaneously with a nearby capacitance and noise compensating null probe (fully insulated from the plasma) to enable bias sweep rates on a microsecond timescale. Traditional thin-sheath Langmuir probe theory is applied for interpretation of the collected probe data. Data at a sweep rate of 100 kHz are presented, however the developed system is capable of running at 1 MHz—near the upper limit of the applied electrostatic Langmuir probe theory for the investigated plasma conditions. Additional data using this diagnostic are extensively detailed in Chapter 6. Large sets (100,000 sweeps at each of 352 spatial locations) of contiguous turbulent plasma properties are collected using simple electronics for probe bias driving and current measurement attaining 80 dB signal-to-noise measurements with DC-1 MHz bandwidth. Near-field and far-field plume measurements with the HDLP system are performed downstream from a modern Hall effect thruster where the time-averaged plasma properties exhibit the approximate ranges: electron density n_e from 1×10^{15} - $5 \times 10^{16} \text{ m}^{-3}$, electron temperature T_e from 1-3.5 eV, and plasma potential V_p from 5-15 V. The thruster discharge of 200-V (constant anode potential) and 2-A (average

discharge current) displays strong, 2.2-A peak-to-peak, current oscillations at 19 kHz, characteristic of the thruster "breathing mode" ionization instability. Large amplitude discharge current fluctuations are typical for most Hall thrusters, yet the HDLP system reveals the presence of the same 19 kHz fluctuations in $n_e(t)$, $T_e(t)$, and $V_p(t)$ throughout the entire plume with peak-to-peak divided by mean plasma properties that average 94%.

3.1 The Time-resolved Langmuir Probe

Langmuir probes were the first plasma diagnostic [52] developed nearly a century ago. Today they are still employed as one of the most useful and common means of measuring plasma density, electron temperature (or the Electron Energy Distribution Function, EEDF), plasma potential, or floating potential with excellent spatial resolution, and a simple theory of probe data interpretation.[53, 54, 55, 56] The temporal resolution of this indispensable electrostatic diagnostic has often been quoted as the inverse of the ion plasma frequency [54, 55] which should enable μs resolution for a variety of plasmas. In the following Chapter 4, the temporal resolution of a rapidly swept Langmuir probe (and in HDLP configuration) is examined in detail, confirming sub- μs resolution (limited, not just by f_{pi}^{-1} , but also by capacitive and polarization effects) for plasma environments typical to Hall Effect Thrusters (HETs) and Tokamaks. In this chapter, the developed HDLP diagnostic is detailed and typical time- and space-resolved data taken downstream from a modern HET thruster are presented.

3.2 Background: Rapid Sweep Langmuir Probing

A scattering of previous investigations of rapidly swept (faster than or equivalent to 100 kHz) Langmuir probe experiments [57, 58, 59, 60, 61] have met limited success due to the many challenges of such measurements—most stemming from the electrical

biasing and measurement circuits. Cabling and circuit stray capacitance can introduce displacement current that can easily exceed the electron saturation current and some means of compensating for this current is required. The use of a capacitance matched "dummy probe" was first suggested by F. F. Chen in 1966, [55] and various implementations of this have utilized an external (positioned far from the actual Langmuir probe) but otherwise similar probe [59, 60, 62] or a variable capacitor [57, 61]. Perhaps the largest flaw of all prior fast-sweep Langmuir probe experiments resides in the use of low 8-12 bit digitization common to oscilloscope and high-speed DAQ cards. Coupled to small sample-set sizes (often less than 100 consecutive I-V curves), low-precision measurements are nearly unavoidable. In the High-speed Dual Langmuir Probe (HDLP) presented in this thesis, a null or dummy probe is used also, but effort was made to ensure the probes, and all circuitry and their wiring remained within 1 cm of each other. This guaranteed more exact capacitance cancellation, as well as extraneous electromagnetic pickup cancellation. The novel HDLP approach is unique for using nearly exactly matched probes (from amplifier to plasma, where one is covered and the other is exposed), (unshielded insulating) wiring, and electronics, facilitating sub- μ s timescale sweep-rates. Another challenge to rapidly swept probe experiments is the generation of the biasing waveform, which requires a broadband power amplifier with specifications (e.g. DC - 1 MHz, ± 200 V, ± 200 mA) that are uncommon in commercial off-the-shelf amplifiers and often requires custom design. A final difficulty arises in the measurement of the minute probe currents (nA to 10's of mA) riding high-voltages (± 200 V) at high-frequency (DC - 10MHz) whilst maintaining high signal-to-noise ratios (SNR > 80 dB) - specifications not presently served by any off-the-shelf ammeters. In this

realm of daunting experimental requirements, few have ventured. For these reasons, the pre-existing work using rapidly swept Langmuir probes is scarce and their resultant temporal properties are often of poor quality.

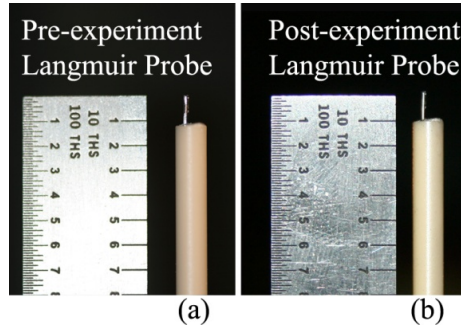


Figure 3.1. Photographs of the Langmuir probe (a) prior to experiment and (b) afterwards indicate negligible dimensional and surface changes.

3.3 Langmuir and Null Probes

When rapidly sweeping a probe bias, $V_B(t)$, it is necessary to correct for the capacitive loading observed; for the presented HDLP system, the null probe performs this duty. While alternative methods of capacitance correction exist,[57-62] the present method is most effective at measuring unknown a priori stray capacitance with simultaneous EMI rejection. These features facilitate sweeping at sub- μ s timescales near the temporal limits of the plasma and probe theory (as will be shown in Chapter 4). The Langmuir and Null probes are configured with identical tungsten collectors, supports, wiring, feedthrus, and measurement circuitry. The only difference between the probes is the additional (about 1 cm) extension of the Langmuir probe into the plasma while the null probe remains fully insulated from the plasma environment. The exposed portion of the Langmuir probe is 0.5 mm in diameter and 3.1 mm in length. The tungsten probe surface was initially cleaned abrasively (and dusted with high-pressure N_2) and chemically (to remove organic residues), then baked. The energetic HET ions (per ion

the resulting mutual (C_m) and stray capacitive (C_s) differences. However, small sensing shunts ensure $V_{LP} \approx V_{Null}$ and thus one may then neglect this final term. The effectiveness of the HDLP compensation technique is demonstrated in Figure 3.3 for 100 sequentially sampled raw I-V traces collected during one millisecond of HET plume data collection (data from near- and far-field locations included). The corrected I-V traces are devoid of cable capacitive effects and the wide family of I-V curves at this single point indicates strong plasma fluctuations arising from the HET breathing mode. Rounding of the uncompensated I-V space profiles occurs at the bias voltage range edges due to the change of sign in dV_B/dt and finite frequency-response effects.

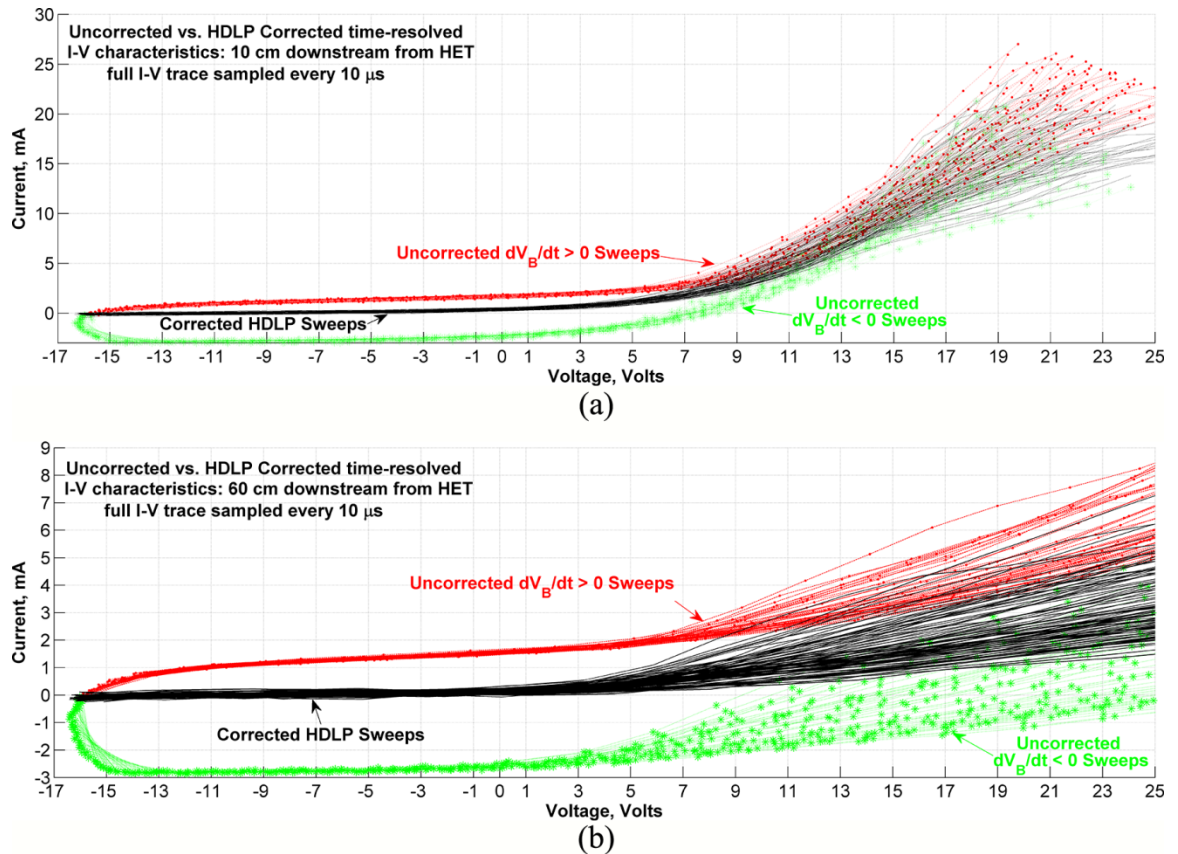


Figure 3.3. 100 time-resolved I-V characteristics acquired at 100 kHz showing the use of Eqn. (3.1) for HDLP data (a) 10 cm and (b) 60 cm downstream of the HET discharge channel exit.

3.4 Probe Transmission Lines

In an effort to minimize line capacitance along the conduction path from the probes to the bias driving amplifier, high-speed transmission line characteristics were studied in conjunction with SPICE circuit simulation software. Conventional Langmuir probe wiring consists of fully shielded BNC cable or twisted pair cable—yet with respective capacitances of 100 pF/m and 50 pF/m, use of these lines would have led to the generation of displacement currents at least two orders of magnitude larger than the expected far-field electron saturation current. Indeed, simulations involving large capacitive loading on the bias amplifier caused circuit destabilization in many scenarios. This phenomenon necessitated either placement of all circuitry (amplifier and current sensors) inside the chamber (in close proximity to the Langmuir and Null probes) or the use of dramatically lower capacitance transmission lines.

The theoretical capacitance per meter from a single bare wire of conductor radius, r , suspended a height, h , over a ground plane can be determined from Gauss's law as:

$$C_{||gnd} \approx 2\pi \epsilon_o / \ln(2h/r), \quad (3.2)$$

where ϵ_o is the permittivity of free space. Thus, a small gauge wire suspended relatively far from any conductive grounding planes will possess a very low capacitance. In this experiment, an 18-AWG stranded high-voltage silicone-insulated wire ($r_{18AWG} = 0.5$ mm) along with fiberglass supporting posts are used to maintain a suspension height of $h \approx 0.3$ m for the cable runs inside and outside the vacuum chamber. The theoretical transmission line capacitance of this configuration is 8 pF/m. This estimate neglects the

capacitance at the feedthrus as well as that inherent to the amplification and sensing circuitry. Measured total stray capacitance averages roughly 200-300 pF per probe—which varies from position to position and depends on the probe bias (via the plasma sheath surrounding the non-conductive portion of the probe support). This amount of stray capacitance works out to about 2-3 mA of displacement current for the 100 kHz swept data herein discussed and capacitive offsets of this magnitude are visible in Figure 3.3. The ion and electron saturation currents at the furthest point from the thruster (64 cm) average about 1 μ A and 0.3 mA, respectively.

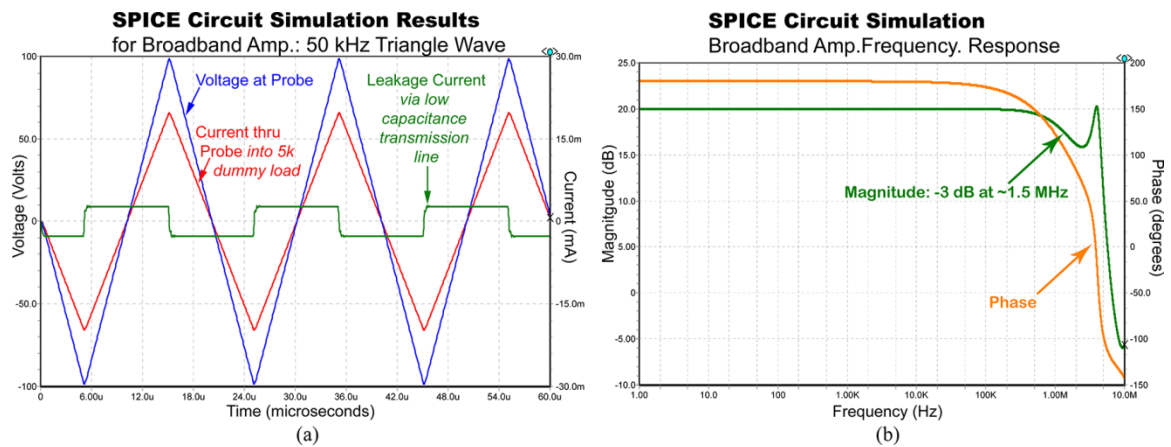


Figure 3.4. SPICE Simulation results for custom developed broadband amplifier and transmission line. Left (a) transient response to input triangle waveform ± 10 V_{pk-to-pk}, into a 5 k Ω dummy load (to roughly simulate plasma loading on circuit). Right plot (b) frequency response of circuit—green trace shows magnitude (bump due to transmission line capacitive and inductive coupling).

3.5 Probe Biasing Circuit

Conventional laboratory power supplies are not suitable for rapid high-voltage bias waveform generation since these supplies' frequency responses reside in the low kHz. In fact, there is a near void of commercially available high-voltage high-frequency broadband power-amplifiers that meet the requirements of the HDLP. SPICE was used to design a HDLP-capable amplifier with the specifications in Table 3.1 and Figure 3.4.

Table 3.1. Specifications of the probe bias amplifier design for the HDLP.

Broadband Power Amplifier Specifications	
Bandwidth	DC – 1 MHz (-3dB)
Voltage Output	± 200 V
Current Output	± 200 mA (4 quadrant)
Voltage Gain	20 dB to 40 dB

At the heart of the amplifier resides an APEX high-voltage (450-V) high-slewrate (1-kV/ μ s) MOSFET operational amplifier (PA98). Both active and passive cooling are applied to maintain stable high-performance operation (amplifier core temperature is continually monitored). A photograph of the assembled broadband amplifier is included in Figure 3.5. Laboratory-grade switch-mode power supplies (<0.1% ripple) are employed as ± 220 V rails with significant bypassing to ensure low-noise amplification (two Sorenson DCS600-1.7E supplies). Input to the PA98 is buffered, low-pass filtered (to about 1 MHz), and saturation-limited by a low-noise unity-gain operated Linear Technologies (LT1215) operational amplifier.

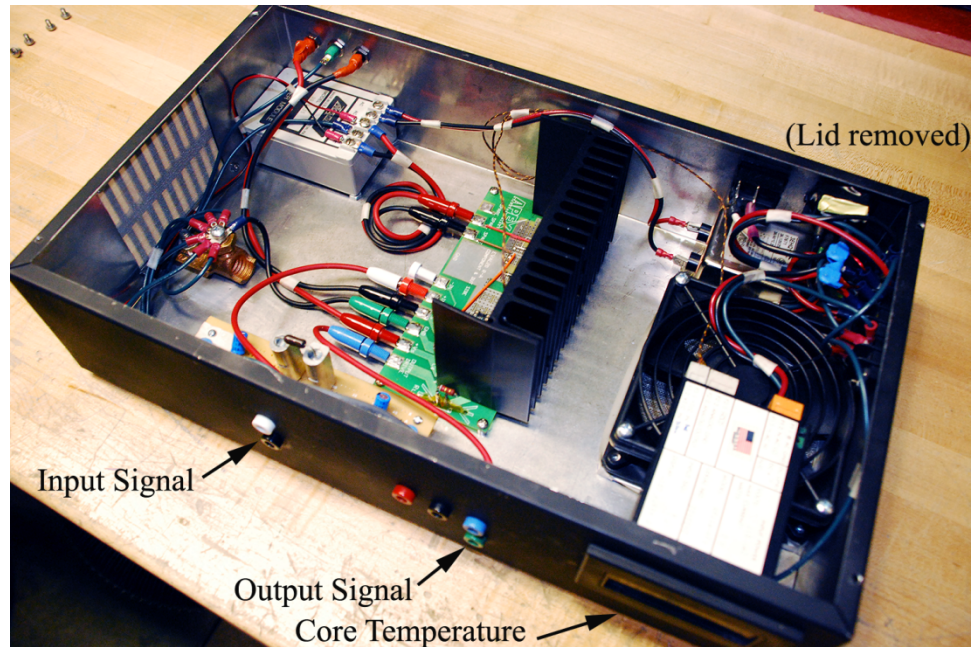


Figure 3.5. Broadband power-amplifier and signal-conditioning circuitry in ventilated aluminum enclosure.

Given the DAQ system discrete sampling rate at 2 MHz, only 20 current-voltage (I-V) points are collected for each Langmuir probe trace with sweeps every 10 μ s. Since several important features of a Langmuir probe I-V trace occur when the bias voltage is small (the electron retarding exponential current growth region, floating potential), it was initially thought to have additional points in this region as the “Modified Tangent Waveform” in Figure 3.6 shows. The major disadvantage of this non-linear waveform is that, from Eqn. (3.1), large variations in the leakage current occur for the non-constant dV_B/dt term. While the null probe was effective at removing the stray capacitive current for this waveform, the mutual capacitive current correction included in Eqn. (3.1) was not as effective and thus, this biasing waveform abandoned. The solution identified to mitigate this poor I-V resolution issue was to use a triangle waveform with a DC offset and a narrowed bias voltage range. Initially, experiments were run by sweeping the probe bias from -100 V to +100 V in 10 μ s, resulting in an I-V point sampled by the

DAQ system every 10 V. By instead sweeping from -20 V to +50 V, an increase in voltage resolution to a sample point every 3.5 V is attained. However, due to the voltage drops across the shunts (proportional to probe current) another improvement in probe bias spacing is gained, providing a resolution as fine as 0.5 V.

Once soldered, the broadband power-amplifier was housed in a shielded enclosure along with EM noise filtering, fuses, linear power supplies, active cooling, thermocouples for thermal monitoring, banana-jack connection ports for input and output signals, and star grounding (see Figure 3.5). A single shunt-based current-monitoring circuit was also added to the enclosure, but the addition of the null probe necessitated a more sophisticated dual-symmetric current measurement circuit discussed in the following Section 3.6.

The biasing waveform provided as input (for presented data) is a 7.0-V peak-to-peak (or $70\text{-V}_{\text{pk2pk}}$ after amplification) 50-kHz symmetric triangle (or sawtooth) wave setup by a 20 MHz arbitrary waveform generator (Agilent 33220A). A slight DC offset of +15 V is applied to ensure the probe bias attains plasma potential and electron saturation current. Many experimentalists make use of a skewed ramping triangle waveform, taking swept I-V data only during the wider (often positive dV/dt) portions. However, the narrow (often sub-ns wide) resetting of such waveforms produces enormous voltage slewrates that would (if the amplifier could handle such loading) produce enormous 0.1 to 1-A of capacitively displaced current as seen in Figure 3.6.

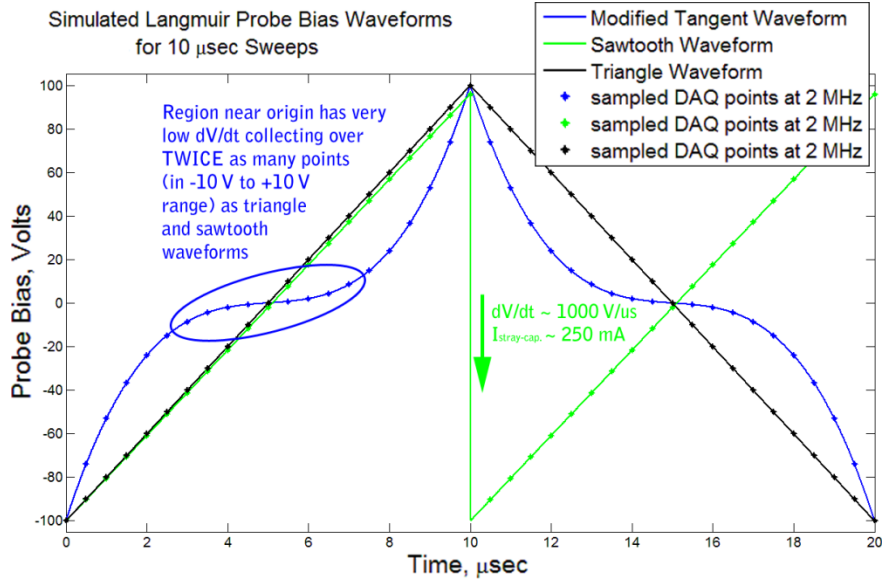


Figure 3.6. Various Langmuir probing biasing waveforms considered.

With the Null probe capacitance correction, both halves of a symmetric triangle wave yield I-V characteristics in a manner more amenable to the plasma probe-sheath equilibrium since the monolithic bias ramping between ion and electron saturation (then back to ion saturation, and so on) is not as abrupt as the skewed sawtooth. In this way, a 50-kHz triangle wave creates a full I-V characteristic, $V_B \in [-20V, 50V]$, every 10 μ s, with interpreted plasma properties time-stamped at the center of each trace, which typically occurs when the bias is near the plasma potential.

3.6 Dual-symmetric Current Sensing Circuit

While shunt-based current measurement is typically a straightforward means to acquire small and large currents alike, the high-voltage and high-bandwidth content of the Langmuir and Null probe signals complicate this method of current measurement considerably. Ideally, the voltage drop across a shunt resistor can be amplified by an optically isolated analog amplifier, thereby removing a high common mode voltage (200-V or more) from the signal. Unfortunately, the frequency responses of the fastest modern

isolation analog amplifiers cut off at 100-200 kHz, and for this experiment, 10-MHz or higher was targeted. Additionally, many conventional shunts are wire-wound precision resistors, which dissipate the I^2R heat load efficiently to minimize thermal resistance drifting. However, the inductance of wire-wound resistors is not negligible at high frequencies greater than 1-MHz. Thankfully, a new class of thin- and thick-film metal oxide shunts is available with ultra-low inductance and integrated heat sinks to maintain low thermal drifting. A BK Precision 5491A 50,000-count digital-multimeter was used to measure the shunt resistances with high-accuracy, allowing for selection of a pair of well matched shunts, having nearly equivalent resistances; i.e., <0.1% different. The 5491A was also used to measure the high-precision (0.1% tolerance) resistors used in the construction of the -21 dB (1/11) voltage dividing networks (used here to reduce the high common mode voltages to a DAQ compatible range of ± 10 V). In order to keep the voltage division reductions constant, special high-bandwidth (DC to 20-MHz) ultra-high input impedance JFET buffers were employed to maintain pico-ampere scale loading on the voltage dividing network. Current drain from the dividing networks may be corrected for during post processing, and using Figure 3.2 with Ohm's law, Eqn. (3.3) is obtained.

$$I_{LP,Null}(t) = \frac{V_{IN}(t) - V_{B,Null}(t)}{R_{S,LP,Null}} - \frac{V_{B,Null}(t)}{110k\Omega} \quad (3.3)$$

Since here $R_S = 989.2 \Omega \ll 110 \text{ k}\Omega$, the latter term can usually be ignored at a loss of accuracy. Using Eqns. (3.1) and (3.3), with measurement uncertainties of $\partial V_B = \pm 74$ mV (this includes Analog to Digital Conversion, ADC, and divider network uncertainties) and $\partial R_s = \pm 0.1 \Omega$, the typical current measurement overall accuracy is propagated to $\pm 53 \mu\text{A}$ (average conditions). If DAQ channels are in short supply, the

symmetric sensor design using identical current sensing shunts provides a good estimate of the true plasma current as simply $I_p \approx (V_{Null} - V_{LP})/R_S$.

Often, with repeatable signals at high frequencies, trigger aligned windowed averaging is a useful feature of oscilloscopes and data acquisition systems that can dramatically increase the SNR (by up to \sqrt{N} where N is the number of windows). Other electrostatic probe based investigations [21] of HET plume transients have used this approach with limited success. The plasma in the plume of a HET is rich with turbulent fluctuations and this stochastic behavior invalidates this type of time-series ensemble averaging. For this experiment, extreme care was placed in minimizing signal noise. Firstly, as mentioned in Section 3.3, the null probe signal subtraction effectively removes noise picked up by the probe transmission lines. Secondly, the current sensing circuit was designed with two channels of symmetrically mirrored component and trace layouts. The circuitry was also shielded from the high-voltage transmission lines. The unshielded transmission lines act as antennas and volts of electromagnetic radiation can easily be picked up by any conductor in close proximity. The two matched, low-noise current shunts are also thermally equalized to each other and ambient conditions via a large copper heat sink. An extra set of buffers provide additional output signal conditioning allowing for impedance matching with the BNC cable connections to the DAQ system. The full measured specifications of the dual symmetric current sensing circuit are listed in Table 3.2.

Table 3.2. Specifications of the dual-symmetric current sensing circuit designed for the HDLP.

Dual-Symmetric Current Sensing Circuit Specifications	
Bandwidth	DC – 1 MHz (-3 dB) ⁱ
Measurement Range	±200 mA ⁱⁱ
Resolution (with 16-bit DAQ)	3 μA
Signal-to-Noise Ratio (after DAQ)	80 dB
Max Signal Voltage	±150 V ⁱⁱ
Overall Accuracy	±(0.5% reading + 50 μA)

ⁱ*Intentionally low-pass filtered match the DAQ Nyquist frequency; unfiltered response is closer to DC-10 MHz.*

ⁱⁱ*These limits are adjustable depending on choice of shunt and dividing network resistors.*

Testament to the effectiveness of this low-noise symmetric current measurement design, we compare the results obtained from this circuit against the results obtained from off-the-shelf Tektronix components in Figure 3.7. The lower plot in Figure 3.7, attained with the dual-symmetric current sensing circuit, shows significant improvement in the SNR performance. Initially, it was thought that relatively expensive Tektronix probes (P5200 high-voltage 20 MHz active differential probes) would outperform the custom circuit developed, but with 10 times the noise, the Tektronix probes performed rather poorly (in this application). The DC accuracy of the custom low-noise dual-symmetric circuit was tested with Fluke 77III digital multimeter showing overall error of less than 1% (as limited by the Fluke resolution). A non-inductive 3160.3 Ω reference 20-W resistor was used to provide the high-frequency dummy load in Figure 3.7. After significant windowed averaging (using 512 windows, and 50 triangle waveform cycles), the AC accuracy of the Tektronix P5200 probes agreed with the dual-symmetric current sensing circuit to within less than 0.5% (comparing peak-to-peak values). The overall accuracy in Table 3.2 is computed using a standard propagation of errors detailed in Section 3.8.

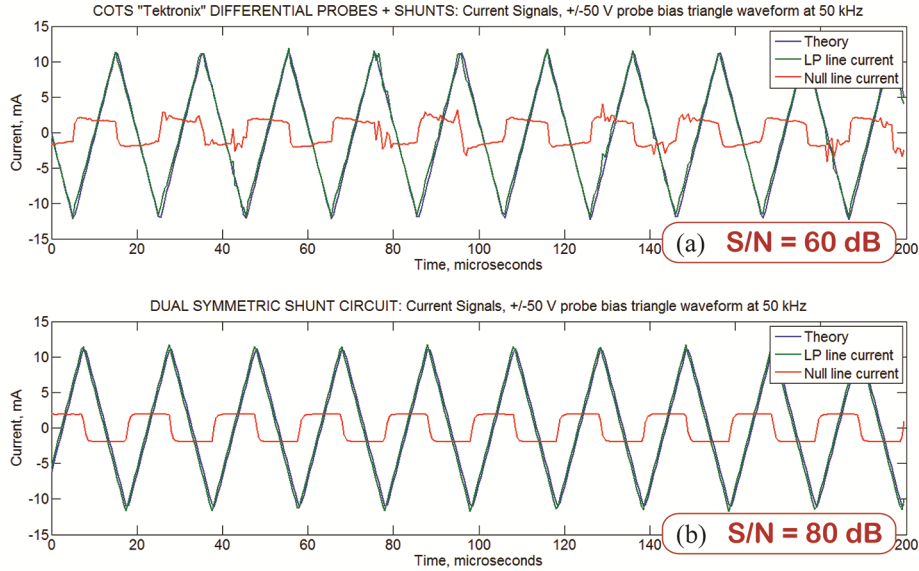


Figure 3.7. COTS current measurement results versus custom current measurement circuit results. The upper trace shows raw current data obtained with “commercial-off-the-shelf” Tektronix P5200 differential high-voltage active probes with SNR of 60 dB.

The lower trace shows raw current data obtained with the custom developed dual symmetric current shunt circuit with SNR of 80 dB. A dummy load 3-k Ω non-inductive power resistor was used in this comparison, and the “Theory” traces correspond to the current expected via Ohm’s law.

The noise level (measured with both the dummy resistive load and with an open circuit) in the dual-symmetrically sensed current is bounded in an envelope 20 μ A wide. Since ion saturation currents (of the probe and plume investigated) are in the range of 1 to 50 μ A, use of the electron saturation current (and not the ion saturation) for plasma density determination is required here as is typical for the HDLP approach (this is explained more fully in Chapter 4). To prevent aliasing, the shunt resistors selected were chosen (in part) to form a low-pass filter with the probe transmission lines with a -3 dB cutoff frequency at $f_{RC} = 1/(2\pi C_s R_s) \approx 1$ MHz, corresponding to the ADC Nyquist frequency.

3.7 I-V Trace "Noise" Vanishing Act

In all plasma measurements, whether from Langmuir probe characteristics or laser-induced fluorescence intensities, noise is omnipresent and often comparable to signal magnitudes in unfiltered signals. In many cases, this noise is the signature of high-speed transient plasma fluctuations such as the Hall thruster breathing mode. Common practice for plasma measurements incorporates extensive application of analog low-pass filters (inline additions or those built into low-frequency analog-to-digital converters), or post-processing techniques such as boxcar averaging, smoothing, or more advanced digital signal processing methods (finite impulse response filters, infinite impulse response filters, etc.).

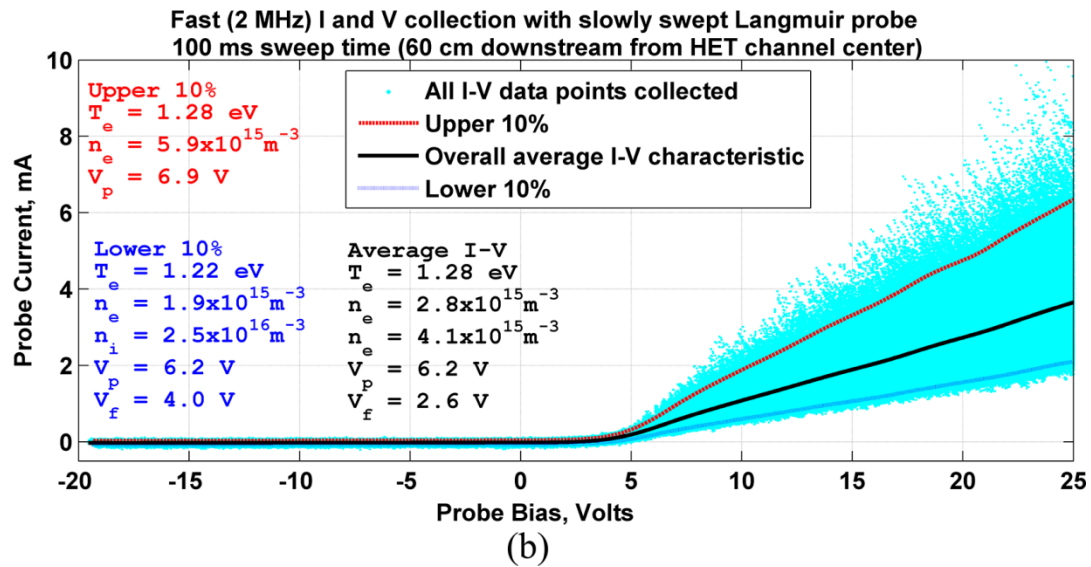
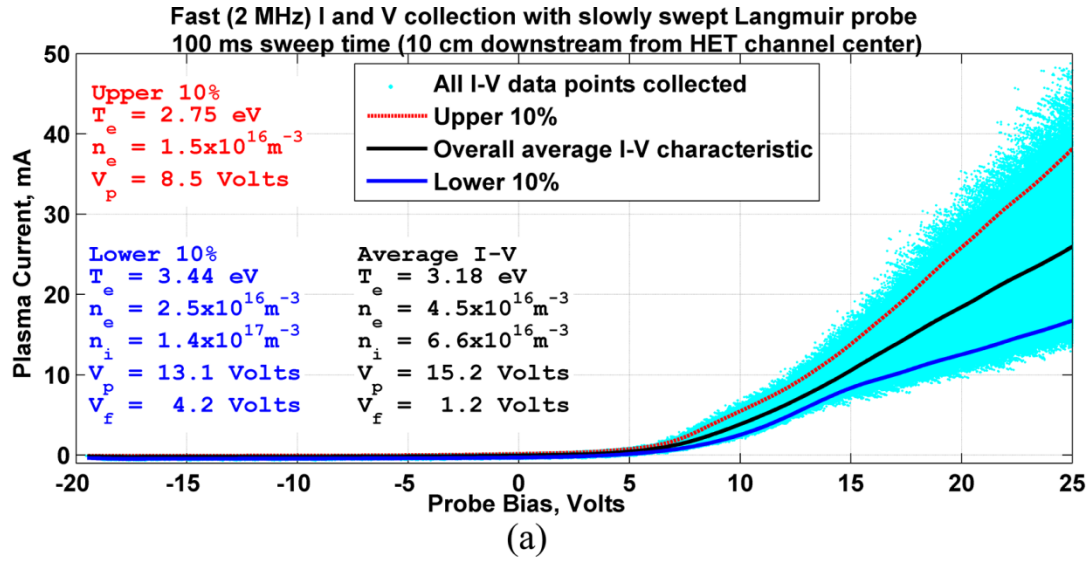


Figure 3.8. Misleading I-V "noise" observed for a slowly swept (100 Hz sweep rate) Langmuir probe taken (a) 10 cm and (b) 60 cm downstream of the HET. The Raw I-V data pairs are sampled at 2-MHz and their resulting scatter is an indication not of poor measurement technique, but of plasma turbulence. A few averaged I-V traces are fitted to the raw I-V distributions to emphasize the arbitrariness of using the time-averaged I-V characteristic.

Once the rate of plasma property probing exceeds the rate of large scale plasma oscillations by more than twice, a vast majority of the "noise" simply vanishes. For Langmuir probe characteristics, this dramatic vanishing act is displayed by comparing Figure 3.3 to Figure 3.8 for two sweep rates: 100 Hz and 100 kHz. The same electronics

and plasma environments give rise to rather distinct I-V characteristics each with varying degrees of "noise." At 100 kHz, the I-V traces are individually quite smooth, while the 100-Hz swept I-V data are riddled with "noise" that arises from 19-kHz HET breathing mode turbulent plasma property fluctuations. The resolving of I-V "noise" as meaningful plasma transients is rather remarkable, and with the HDLP I-V data, direct (unsmoothed) second-derivatives of the electron current are possible providing the capability to acquire time-resolved EEDFs using the HDLP.

3.8 Error Analysis

It is important to point out a shortcoming in the presented HDLP data involving the poor bias voltage (per single trace) resolution. The analog $I(t)$ and $V(t)$ sampling at 2 MHz captures only 20 points in I-V space per single time-resolved trace. This creates gaps of 1-4 V between consecutive bias voltage samples—fundamentally increasing uncertainty in the measurement of $V_f(t)$ and $V_p(t)$, but not necessarily $T_e(t)$ (using inverse slope method) or $n_e(t)$. While linear (or spline) interpolation between points reduces the error in computing $V_f(t)$, the uncertainty in $V_p(t)$ and the energy resolution of an EEDF remain about equal to the spacing of the bias voltage points (since $V_p(t)$ and the EEDF are based on non-constant derivatives with respect to probe bias). Propagation of all measurement errors (prefixed with " ∂ ") is performed in the conventional manner taking special notice to the discrete nature of the ADC measurements. The uncertainty in plasma potential, ∂V_p , is estimated as a combination of the bias uncertainty and the discrete spacing between bias voltages, accounting for the voltage drop across the current sensing shunt as in Eqn. (3.4).

$$\Delta V_{B,step} \Big|_{V_B \approx V_p} = \frac{\Delta V_B}{N_B} \cdot \frac{T_e}{(T_e + I_{esat} R_s)}. \quad (3.4)$$

In Eqn. (3.4) N_B is the number of I-V samples spanning the total bias sweep range ΔV_B (here, $N_B = 20$ and $\Delta V_B = 70$ -V). For ∂T_e , the discrete form of the data is again considered along with averaged I-V values in the range V_f to V_p ; it should be noted that non-systematic T_e uncertainties are reduced by a factor of $1/\sqrt{N_{T_e} - 1}$, with N_{T_e} as the number of I-V points used in the determination of T_e . Thus, a collection of HDLP uncertainties is presented in Eqn. (3.5).

$$\begin{aligned} \partial A_p &= 2\pi \sqrt{(\partial r_p L_p)^2 + (r_p \partial L_p)^2} \\ \partial V_B &= V_B \sqrt{\left(\frac{\partial F_{div}}{F_{div}}\right)^2 + \left(F_{div} \frac{\partial V_{DAQ}}{V_B}\right)^2} \\ \partial I_p &\approx 2I_p \sqrt{\left(\frac{\partial V_B}{I_p R_s}\right)^2 + \left(\frac{\partial R_s}{R_s}\right)^2} \\ \partial T_e &\approx T_e \sqrt{2\left(\frac{\partial V_B}{\Delta V_{B,step}}\right)^2 + 8\left(\frac{T_e \partial I_p}{\Delta V_{B,step} I_{esat}}\right)^2} \\ \partial n_e &\approx n_e \sqrt{\left(\frac{\partial I_p}{I_{esat}}\right)^2 + \left(\frac{\partial A_p}{A_p}\right)^2 + \left(\frac{\partial T_e}{2T_e}\right)^2} \\ \partial V_p &\approx \sqrt{(\partial V_B)^2 + (\Delta V_{B,step})^2} \\ \partial V_f &\approx \sqrt{(\partial V_B)^2 + \left(T_e \frac{\partial I_p}{I_{isat}}\right)^2} \end{aligned} \quad (3.5)$$

Equation (3.5) introduces voltage divider network uncertainty $\partial F_{div} = \pm 0.014$ (for $F_{div} = 11$), probe area uncertainty $\partial A_p = \pm 0.6 \times 10^{-6} \text{m}^2$, and $\partial V_{DAQ} = \pm 2$ mV. In Eqn. (3.5), units are S.I. except for electron temperature in eV. While these uncertainty estimates vary throughout the plume, the relative uncertainties for the data in this thesis range

approximately as $\partial n_e/n_e \approx \partial T_e/T_e \approx 10\text{-}20\%$ and $\partial V_p/V_p = 10\text{-}40\%$. It is worthwhile to note that the uncertainties in Eqn. (3.5) are not inclusive of uncertainties inherent to the applied sheath-limited electrostatic probe theory (typically on the order of 50%). Indeed, as derived in the examination of the HDLP temporal limits (included in Chapter 4), a barrage of additional dynamic effects (sheath displacement current, polarization drift current, etc.) are known to adversely affect the collected plasma current. For the conditions of this research, these effects are anticipated to contribute additional collected current, $|\Delta I_{dyn}|$, on the order of the ion saturation current. Since $|\Delta I_{dyn}| \leq |I_{sat}| \ll \partial I_p$ for the presented data, the preceding equations are largely unaffected, but the accuracy of the floating potential is quite low. Using the slope of the (Maxwellian) electron current near the floating potential, one obtains the final term of the final line of Eqn. (3.5),

$$\partial V_f \Big|_{\text{from } \partial I_p} \approx \partial I_p \Big/ \left(\left. \frac{dI_p}{dV} \right|_{V_f} \right). \text{ When } \partial I_p \approx |I_{sat}|, \text{ the uncertainty in the floating potential}$$

is then approximately $\partial V_f \approx \pm T_e$; however, for the data presented here, the uncertainty in the floating potential is many times the magnitude of T_e since $\partial I_p > |I_{sat}|$ at all locations.

Finally, validation of the HDLP was obtained by several methods. Using the same experimental setup to measure the same plume region and conditions, a slowly swept Langmuir probe (100 sweeps per second) provided time-averaged I-V traces (see black traces in Figure 3.8). Plasma properties from these time-averaged I-V traces versus time-averaged properties from the HDLP (100-kHz) traces exhibit an average difference of about 23%. The subtleties involved in the differences such as systematic under-predictions of electron temperature with the slowly swept Langmuir probe (whose I-V characteristics possess two distinct electron populations: hotter primary and cooler bulk groups) is under continued study. Secondly, the dynamics of the plasma was

qualitatively validated by use of a high-speed (109,500 frames/s) camera that confirmed the existence of visible emission fluctuations from the plasma in direct proportion with the HDLP measurements (included in Chapter 6).[63]

3.9 Typical HDLP I-V processing results

After collection of the HDLP time-resolved I-V traces, the plasma properties are determined using a simple algorithm outlined in Section 4.3. Typical results from this Langmuir probe algorithm are shown in Figure 3.9, while the time-resolved EEDF is included and appears quite Maxwellian (for this case; other cases are often markedly non-Maxwellian), the poor energy resolution ($\Delta E \approx 3$ eV), as discussed in the preceding section, limits the usefulness and accuracy of EEDFs for the presented data.

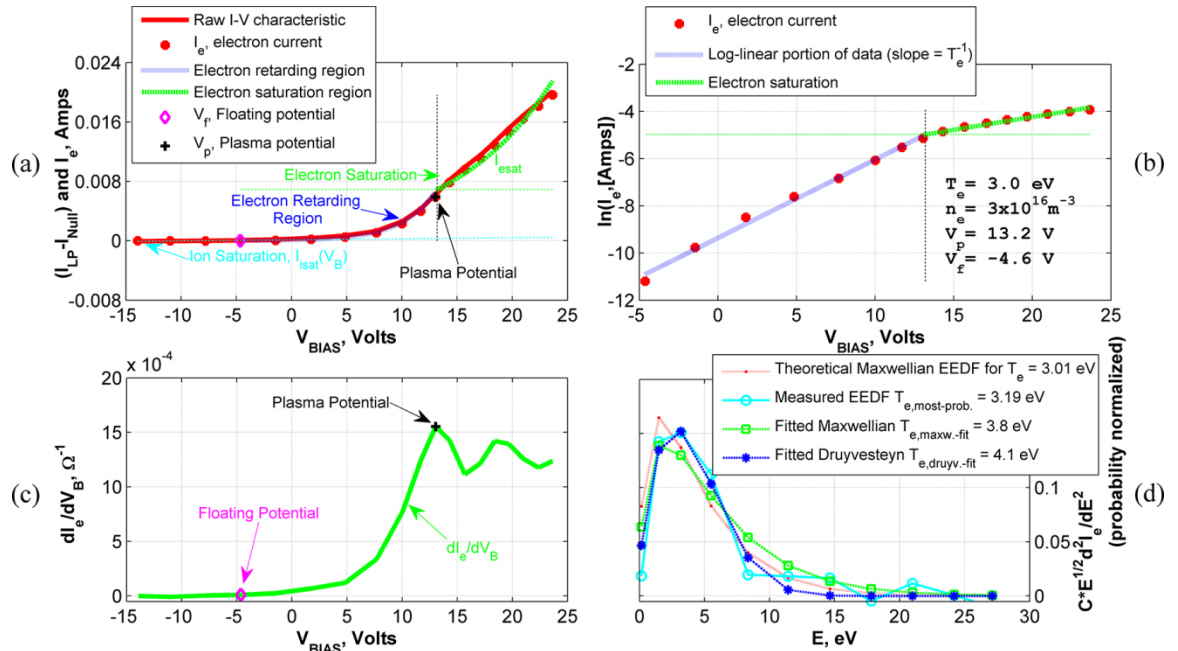


Figure 3.9. Typical single time-resolved (10- μ s) HDLP I-V characteristic with Langmuir probe algorithm results, shown on linear (a) and logarithmic (b) scales. The first (c) and second (d) electron current derivatives used in generating the lower two plots have not been smoothed, and are computed numerically.

3.10 Typical HDLP time-resolved plasma properties

While the majority of HDLP plasma measurement results are presented in Chapter 6, a short time-resolved sequence of (a) electron density, (b) electron temperature, and (c) plasma potential is included in Figure 3.10. The simultaneous thruster discharge current is included in each trace to show how closely related the plasma state is to the thruster electrical power state. Included in these data are error-bars computed according to Eqn. (3.5), demonstrating that the HDLP measured plasma transients are not simply noise due to measurement uncertainty.

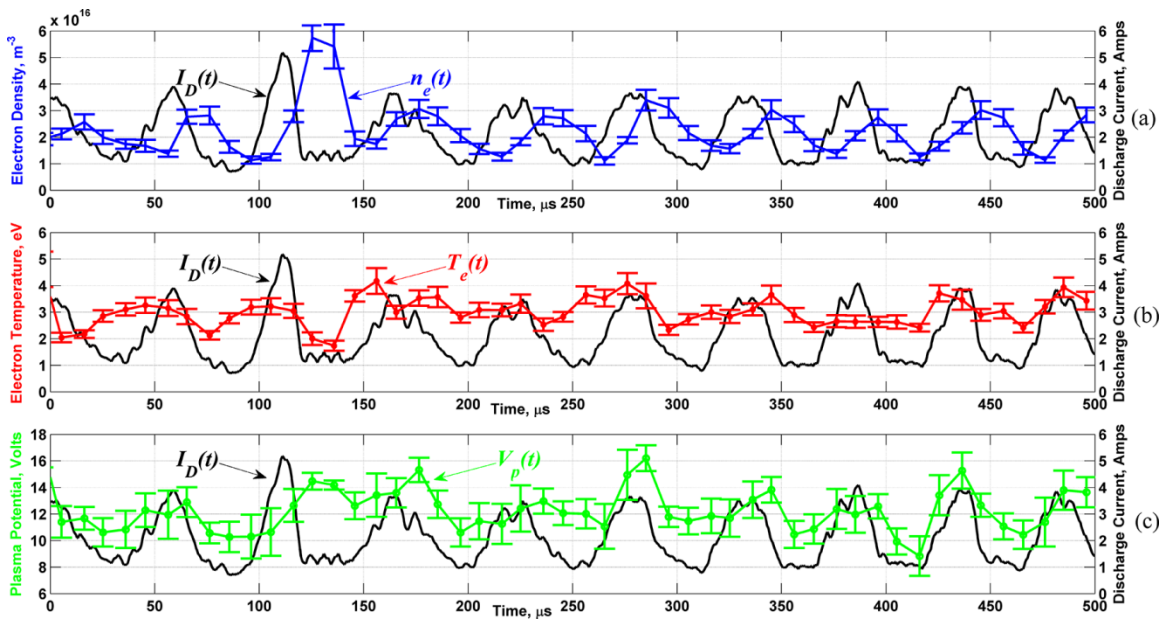


Figure 3.10. HDLP time-resolved simultaneous plasma properties measured 20 cm downstream (channel aligned) from the HET. The black solid signal in (a)-(c) shows the instantaneous thruster discharge current, $I_D(t)$, that is dominated by the 19-kHz breathing mode fluctuation. While electron density fluctuations (a) follow the $I_D(t)$ fluctuations with a short delay ($\approx 20 \mu\text{s}$), $T_e(t)$, (b), and $V_p(t)$, (b), track the fluctuations nearly in-phase. This sequence is a small 0.5 ms portion typical of the 1 sec of data collected at this position (see Chapter 6 for additional results and discussion).

3.11 Conclusions

A novel high-speed dual Langmuir probe was developed for achieving time-resolved measurements near the upper limit of electrostatic probe theory. A null probe,

used to compensate for stray capacitive and EMI effects, proved key in enabling swept bias and plasma property collection rates of 100 kHz. Combined with carefully designed (yet relatively simple) electronics and data acquisition for making high signal-to-noise measurements, plasma fluctuations—setup by the 19-kHz Hall thruster breathing mode oscillation—were observed at all spatial locations within a 31-cm by 50-cm planar downstream region (these results are presented in Chapter 6). Providing high-spatial and -temporal resolution measurements with a simple design and theory of operation, the HDLP is an invaluable diagnostic tool that is bound to play an important role in understanding low-frequency plasma turbulence.

Chapter 4

Temporal Limits and Theory of a Langmuir Probe

The finite, electrostatically-achievable, temporal resolution of plasma properties from a turbulent discharge is limited by an array of effects wherein the theory of Langmuir probes breaks down. This chapter presents formulations for the particle transit-time, sheath formation time, plasma-probe resonance, polarization current, sheath capacitance, stray capacitance, and mutual capacitance effects all evaluated for time-resolved operation of a Langmuir probe. [64] The resulting timescales serve to place a theoretical bound on the maximum rate of a rapidly swept Langmuir probe as analyzed with typical thin-sheath collisionless probe theory. For plasma typical to the plume of a Hall effect thruster (xenon plasma, $n_e = 1\text{-}1000 \times 10^{+15} \text{ m}^{-3}$, and $T_e = 1\text{-}20 \text{ eV}$), upper limits of 0.01-70 kHz are observed for a non-capacitive compensated Langmuir probe. With a High-speed Dual Langmuir Probe (HDLP, a regular probe plus a null compensation probe), the upper probing frequency limits are increased to 0.04-11 MHz - limited by sheath capacitance in the far- and near-field, and polarization effects for closer internal measurements. For a typical Tokamak edge plasma (with HDLP), the thermally equilibrated hotter species (typically $T_e \approx T_i \approx 10 \text{ to } 20 \text{ eV}$) and lighter ions together lend higher limiting rates of ion transit, sheath formation, and sheath-capacitance effects (in excess of 20 MHz), but the fully-magnetized plasma complicates the collected probe current, limiting the allowable sweep rate to $< 1 \text{ MHz}$ (for a magnetic field of 2 T). Thus

we find that the upper rate of Langmuir probe sweeping is in the low MHz range (0.1 - 10 MHz) for both electric thruster and fusion plasma device diagnostics.

4.1 Introduction

All plasmas exhibit transient fluctuations in their properties due to various electromagnetic interactions. For the interest of plasma based space propulsion, fusion devices, and other plasma systems, the largest magnitude oscillations occur at low frequencies < 1 MHz.[16, 65, 66] Time-resolved measurements of these plasma fluctuations are limited due to an emphasis of prior research on the time-averaged plasma properties using DC diagnostic techniques. However, there exists a growing interest in the temporally-resolved nature of plasma discharge properties including: electron density $n_e(t)$, electron temperature $T_e(t)$ (or electron energy distribution function), and plasma potential $V_p(t)$. Anomalous transport in plasma thrusters [20, 32] and Tokamaks [29, 30] alike is often attributed to turbulent plasma oscillations and low-frequency instabilities (as briefly discussed at the end of Chapter 1). Cross-field electron flux leakage to the walls is one of the key containment challenges in modern magnetically-confined fusion reactors and it also occurs in Hall effect thrusters where it can lower thruster efficiency and increase the rate of erosion.

The original theory of electrostatic current collection by Mott-Smith and Langmuir assumes equilibrium conditions for the sheath and particle flux or current measured at each probe bias.[67] The most commonly listed temporal limitations of a single Langmuir probe are the times required to form a sheath and for charge carriers to traverse this sheath.[54, 68] These limitations are common to all manner of Langmuir probing

(single, double, triple, fixed bias or ramped bias), for all are based on electrostatic sheath flux equations.

Strong plasma oscillations are known to distort DC measurements irrevocably—rendering their accuracy as questionable. Taylor expansions of the flux formulations incorporating temporally perturbed plasma and probe properties,[69, 70] show that the DC probe measurements can experience greatly diminished accuracy for large fluctuations (with little adverse effects from small fluctuations).

These issues and others have imparted the need for time-resolved measurements that capture the fluctuating processes. While RF-compensated Langmuir probes and floating (or fixed-bias) double or triple probes can enable time-averaged and time-resolved measurements (without rapidly sweeping the probe bias), they require additional assumptions that can introduce their own problematic issues making them less than ideal for time-resolved measurements in unsteady plasma environments. Finally, the acquisition of direct back-to-back swept Langmuir probe time-resolved measurements—as opposed to phase-averaged measurements (e.g. such as enabled by the commercially available Hiden ESPion Langmuir probe) often made in pulsed plasmas[71]—is required for accurate and meaningful data from plasmas rich in turbulent character.

The following sections provide a nearly complete collection of the various temporal limits one might expect with a traditional swept Langmuir probe within the realm of thin-sheath collisionless theory. These limits are motivated with theory, numerical simulations, as well as empirical findings. The compiled formulas for the limiting probe sweep frequencies provide only order of magnitude accurate upper-bounds to the rates of

plasma property acquisition achievable within the traditional electrostatic framework of Langmuir probe theory.

4.2 Electrostatic Probe Theory

A Langmuir probe is comprised of an exposed conductor (e.g., wire) immersed within a plasma. The theory of interpreting the data acquired from Langmuir probes is well established [54-56, 72, 73] and this same thin-sheath collisionless theory may also be applied to high-speed Langmuir probe experiments (within the limitations explored briefly in this thesis). The foundation of Langmuir probe theory is based on the probe current versus probe bias voltage (I-V) characteristic plot (see Figure 4.1 and also Figure 3.9). For collisionless, magnetic-field-free, thin-sheath probe operation, the basic plasma properties of density, temperature, and potential are derived from the Bohm sheath criterion, a relation that balances the flux of charged particles to the conducting surface of the probe by use of the Poisson equation and other fundamental relations.

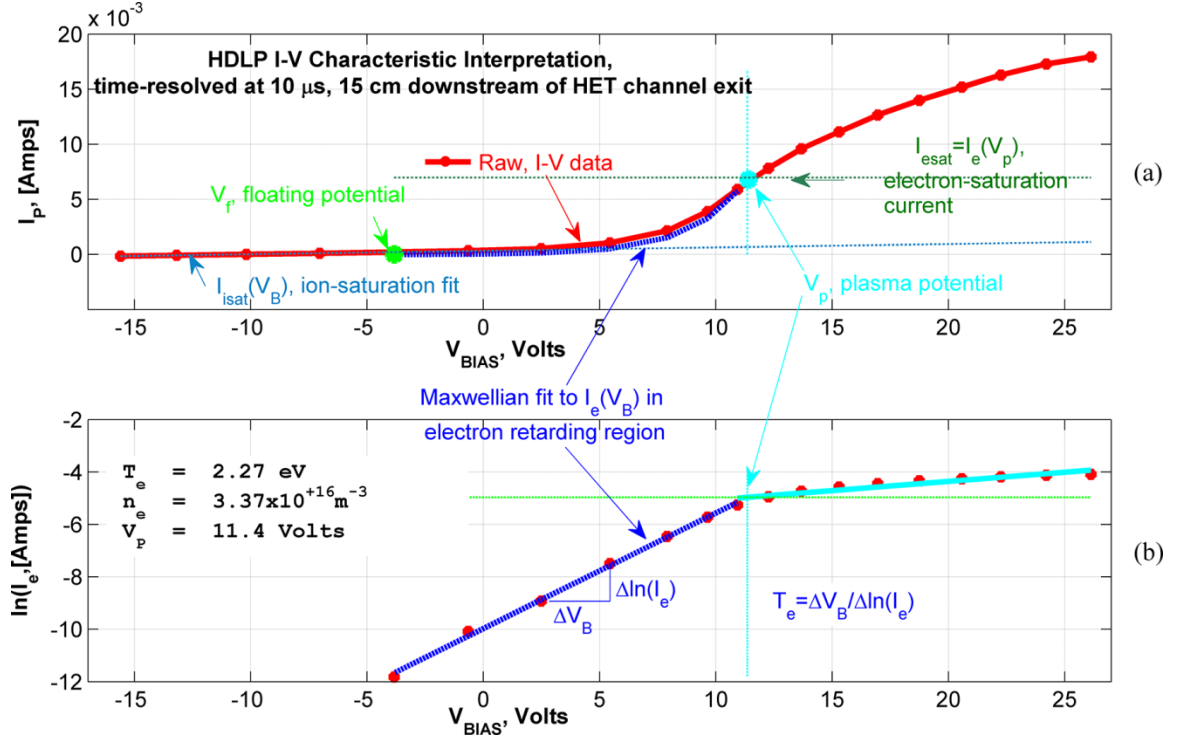


Figure 4.1. The important features of this HDLP I-V characteristic are labeled with the upper trace (a) showing the raw probe current (after null probe correction) and bias voltage while the lower trace (b) displays the effective electron current on a logarithmic scale. No averaging or smoothing has been applied to these time-resolved I-V data, demonstrating the effectiveness of the HDLP.

4.3 Simple Langmuir Probe Thin Sheath Analysis

First, the floating potential (V_f) is taken as the probe bias (V_B , in Volts from chamber ground) at which zero probe current is drawn from the plasma. Second, the electron current is determined using Eqn. (4.1) as the difference between the measured probe current with a linear fit to the probe current (I_p) in the ion saturation region of the I-V trace (where $V_B \ll V_f$) applied at all biases.

$$I_e(V_B) = I_p(V_B) - I_{isat}(V_B) = I_p(V_B) - [m_{isat}V_B + b_{isat}] \quad (4.1)$$

Next, the plasma potential (V_p) is taken as the bias with minimum electron impedance, found at $(dI_e/dV_B)_{max}$. Then, a method of least-squares is employed to

determine the transition region ($V_f < V_B \leq V_p$) log-linear slope used for calculating the electron temperature T_e (in eV):

$$T_e|_{slope-method} = \left(\frac{d \ln I_e}{dV_B} \right)^{-1} = \frac{(V_2 - V_1)}{\ln \left(\frac{I_2}{I_1} \right)} \quad (4.2)$$

$V_{1,2}$ and $I_{1,2}$ represent the probe bias voltage and electron current in the log-linear portion of the transition region. One may also compute the electron temperature by using the V_f and V_p directly with the electron mass, m_e , and the ion mass, m_i : [54]

$$T_e|_{potential-method} = (V_p - V_f) / \ln \left(\sqrt{\frac{m_i}{2\pi m_e}} \right) \quad (4.3)$$

This and the preceding equations rely on assuming a Maxwellian electron velocity distribution. For cases where the plasma may possess a non-Maxwellian distribution (with heuristic motivation [22]) one may define an effective electron temperature by partially integrating the first part of Eqn. (4.2):

$$T_e|_{effective} = \frac{1}{I_{esat}} \int_{V_f}^{V_p} I_e(V_B) dV_B \quad (4.4)$$

For a truly Maxwellian plasma, the prior three equations yield equivalent electron temperatures. Figure 4.2 compares these methods with time-resolved HDLP data 10-cm downstream from a 200-V, 2-A Hall thruster discharge (on the axis of the discharge channel). Ion and electron densities (n_i and n_e) are then estimated with the following formulas: [54]

$$\begin{aligned}
I_{isat} &= -\exp\left(-\frac{1}{2}\right)en_i A_p \sqrt{\frac{eT_e}{m_i}} \\
I_{esat} &= en_e A_p \sqrt{\frac{eT_e}{2\pi m_e}}
\end{aligned}
\tag{4.5}$$

The parameter A_p represents the exposed area of the Langmuir probe with e as the electron charge (all SI units, except electron temperature in eV). The electron saturation current is measured as the current which the probe absorbs with a sufficiently high ion-repelling positive-bias potential, here taken as $I_{esat} = I_e(V_B=V_P)$ (shown in Figure 4.1). The ion saturation current is the current measured when the probe is at a large negative bias that repels all electrons. For I_{isat} , the sheath area is typically used in place of the probe area but to avoid an inevitable iteration process and to keep the analysis simple, the probe area is always used here. As the Debye length (proportional to the sheath size) approaches the probe size (and thin-sheaths no longer persist), the use of probe area in Eqn. (4.5) can give rise to significant errors in the computation of ion density, n_i . For this reason (and others), HDLP data presented will make use only of the electron density as determined using the electron saturation current. Theoretically, a probe biased at the local plasma potential is sheathless, and a thin-sheath is less requisite when density is computed using I_{esat} . However, at the plasma potential the larger probe currents may perturb the local plasma properties. [74]

Thruster Plume Electron Temperature Transients, $V_d = 200$ V, channel aligned 10 cm downstream <DLPtest8/sampleset00018.dat>

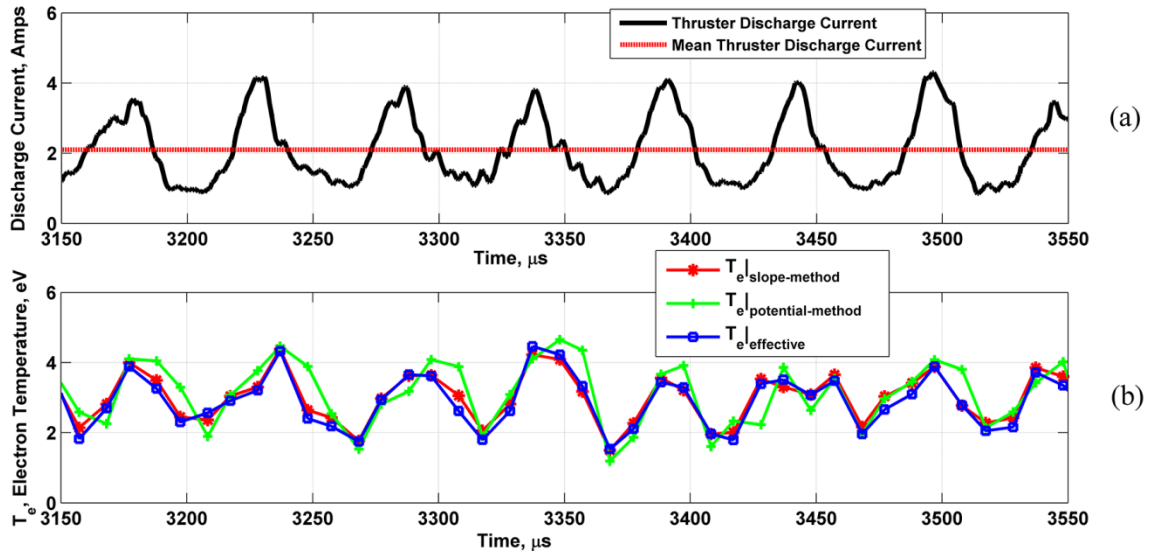


Figure 4.2. A comparison of time-resolved electron temperature formulations using Eqns. (4.2)-(4.4). (a) Temperature fluctuations (at about 19-kHz) appear nearly in-phase (and close in relative magnitude) with simultaneously sampled thruster (b) discharge current fluctuations.

4.4 Temporal Resolution Limits

The ability for the plasma to properly respond to a rapidly changing probe bias is now shown to be limited by at least six temporally constraining issues: 1) sheath transit time, 2) sheath formation time, 3) plasma resonance, 4) polarization drift, 5a) sheath capacitance, 5b) stray capacitance, and 5c) mutual capacitance (5c for the HDLP only).

4.4.1 Sheath Transit Time

The first limiting timescale examined is the transit time a particle requires to traverse the entire sheath surrounding a Langmuir probe immersed in a plasma. A few basic assumptions are needed including planar sheath with dimension on the order of three Debye lengths ($x_s = s\lambda_D = 3\lambda_D$, see Figure 4.3), zero electric field at sheath edge, parabolic spatial potential variation inside sheath $V(x) = V_{p^*} - V_{p^*}x^2/x_s^2$, and (with V_{p^*} as plasma potential relative to probe potential) initial particle velocity at sheath edge

(directed towards probe) as the mean (Maxwellian) thermal speed. Integration then yields the following set of transit times for ions (τ_i) and electrons (τ_e) respectively: [54]

$$\begin{aligned}\tau_i &= \sqrt{\frac{s^2 T_e}{8\pi^2 V_{p^*}} \left(\frac{m_i \epsilon_o}{n_i e^2} \right) \ln \left(\frac{8V_{p^*}}{T_i} \right)} \approx 0.56 \cdot f_{pi}^{-1} \\ \tau_e &= \sqrt{\frac{s^2 T_e}{8\pi^2 V_{p^*}} \left(\frac{m_e \epsilon_o}{n_e e^2} \right) \ln \left(\frac{8V_{p^*}}{T_e} \right)} \approx 0.48 \cdot f_{pe}^{-1}\end{aligned}\tag{4.6}$$

This equation introduces, ϵ_o , the permittivity of free space in Farads/meter, and uses the electron and ion temperatures in eV. The two frequencies included are the ion plasma frequency, f_{pi} , and the electron plasma frequency, f_{pe} . This result shows that ions and electrons traverse the sheath in about one-half of a fundamental plasma oscillation cycle. Most common laboratory plasmas possess electron plasma frequencies in excess of 1 GHz so the collection of electron current during the electron retarding portion of the Langmuir probe I-V characteristic (used to determine T_e) as well as the electron saturation current collection might be relatively uncorrupted for probe sweep rates as brief as a few nanoseconds (neglecting other effects). The ions however, exhibit slower travel across the thin sheaths under analysis, requiring a time that is longer by the factor $\sqrt{m_i/m_e}$ to move from sheath edge to probe surface. In this way, the ion current collected may be under-predicted in the ion saturation region for situations in which the probe bias sweep rate is on the order of the ion plasma frequency (typically exceeding a few MHz).

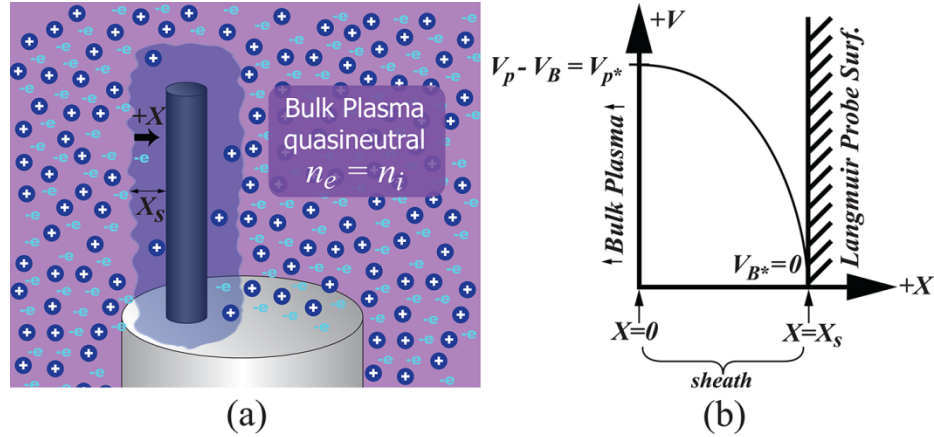


Figure 4.3. (a) Illustration of particles transiting through Langmuir probe sheath (thickness exaggerated). (b) Simple 1D model of the sheath potential. Heavier ions traverse sheath significantly slower.

4.4.2 Complete Sheath Formation

The time required to form a fully steady-state equilibrium sheath is examined next. As the Langmuir probe bias is adjusted (e.g., linearly ramped saw-tooth sweep) adherence to the traditional thin-sheath Langmuir probe theory of current collection depends critically upon the capability of the sheath to change its size and species composition at a rate faster than the rate of probe bias adjustment. While at first glance it may appear that the electron sheath formed at large positive probe bias is able to adjust itself quite rapidly (in a few nanoseconds) due to the large thermal electron velocities, Chen argues [55] that the ions present initially in the formation of the electron sheath must still be displaced before sheath equilibrium is attained. Indeed, numerical studies [75, 76, 77] of the sheath response about rapidly adjusted surface potentials suggest a few (up to 10) ion plasma cycles are required to achieve an equilibrium sheath size:

$$\tau_{sheath-form,simulated} \approx 10 \cdot f_{pi}^{-1} \quad (4.7)$$

Integration of the continuity equation with an unsteady sheath size defined using the Child-Langmuir sheath equation yields the following theoretical estimate for the time to attain a steady-state sheath size: [78]

$$\tau_{sheath-form,Child-Langmuir} \approx \frac{2^{1/4}}{9\pi} \left(\frac{V_p - V_B}{T_e} \right)^{3/4} \cdot f_{pi}^{-1}, \quad V_B \ll V_p \quad (4.8)$$

Yet this formulation and the preceding formulation are only accurate for very high-voltage ion-sheaths typical of ion implantation devices.

Direct exposed electrode experimental measurements of transient sheath formation are confounded by the presence of the many time-dependent effects herein discussed (e.g. transit, sheath capacitance, etc.). Even so, experiments carried out by Oskam, Carlson, and Okuda, [79] suggest that for higher pressure (~ 1 torr) discharges, the charged carrier motion is ion mobility controlled (μ_i), such that the time for charge carrier redistribution is approximately: [54]

$$\tau_{sheath-form,ion-mobility-controlled} \approx \frac{\epsilon_0}{en_i \mu_i} \quad (4.9)$$

Next considered is a modified approach inspired by Loeb's examination of the sheath formation rate, [80] which applies an estimate using the time required for charged-particle thermal fluxes to replenish the volume occupied by the probe (plus sheath):

$$\begin{aligned} \tau_{sheath-form,thermal} &\approx \frac{4V_{sheath-volume}}{(A_{sheath-area} U_{ion-velocity})} \\ &\approx 2 \cdot (r_p + \lambda_D) / \sqrt{eT_e / m_i} \end{aligned} \quad (4.10)$$

Finally, one last consideration to our sheath formation timescale is the effect of plasma flow. While the flow speed, U_∞ , remains well below the thermal speeds for the

individual species, the effects on sheath formation will be minimal. [81, 82] Once the plasma flow or drifting speed is on the order of (or exceeds) the thermal speeds, one might expect from Eqn. (4.10) that the time for sheath formation could be significantly reduced for large effective $U_{ion-velocity}$. To incorporate this effect, here it is proposed to use the flow drift speed as $U_{ion-velocity}$ (as U_∞) in a manner similar to Eqn. (4.10), to obtain (for a cylindrical probe axis perpendicular to the flow) a sheath formation time that includes flow effects:

$$\tau_{sheath-form,flow} \approx 2 \cdot (r_p + \lambda_D) / U_\infty \quad (4.11)$$

It should be noted that for large flow speeds ($U_\infty > \text{Bohm speed, } U_{Bohm} = \sqrt{eT_e/m_i}$) such as the mesothermal plasma of most electric thrusters, a sizable (often dominant since the wake region downstream appears to absorb very little current [81, 83]) "ram" current ion flux is directed to the probe. [82, 84] Adapting this flux to include probe bias dependence (that is negligible for $U_\infty \gg U_{Bohm}$) provides Eqn. (4.12):

$$I_{i,ram}(V_B) = -A_\perp n_i (U_\infty \pm \sqrt{(e|V_p - V_B|)/m_i}) \approx -2r_p L_p e n_i U_\infty \quad (4.12)$$

This expression is only valid for wakeless thin-sheaths with $e|V_p - V_B| \ll \frac{1}{2} m_i U_\infty^2$ and, in general form, shows an increase (+) in ion current $\propto |V_p - V_B|^{1/2}$ for $V_B < V_p$ and a decrease (-) for $V_B > V_p$. The probe area perpendicular to the flow vector, A_\perp , has been evaluated for a flow-transverse-oriented cylindrical probe of length, L_p , and radius, r_p . The flow velocity at which this current flux matches the (non-drifting) probe ion saturation current is $U_\infty|_{I_{isat}=I_{i,ram}} \approx \pi \cdot \exp(-1/2) \sqrt{eT_e/m_i} \approx 2 \cdot U_{Bohm}$. Thus, in

general, to minimize this extra current it is preferred to operate a Langmuir probe in regions where the plasma drifting speed is much less than the Bohm speed ($U_\infty \ll 2 \cdot U_{Bohm}$). Yet, it is often out of the experimentalist's control to ensure low flow velocities, and in this case one can (ignoring sheath effects) correct the collected plasma current by simply subtracting out the extra ion flux that reaches the probe, $I_{i,ram}$ (at all biases below the ion-beam energy, $E_{i,beam}$, in eV). [85] Even without the preceding correction, the electron retarding region (and the electron saturation region in some cases) is largely unaffected by sub- or super-sonic ion drifts (while the electron thermal speed $\gg U_\infty$). [86] For subsonic ion drifts ($U_\infty < U_{Bohm}$, predominant in the *isothermal* plasma of fusion devices [31]) the ion current collected by a thin-sheath Langmuir probe is largely unaffected since the flow merely alters the size of the presheath (shown to disappear [81] as $M_\infty = U_\infty / U_{Bohm} \rightarrow 1$) and that of the Debye sheath, and neither sheath size affects thin-sheath current collection theory. Finally, it is observed that by computing I_e from subtraction of a linear fit to the ion saturation current, as with Eqn. (4.1), the extra "ram" current is conveniently removed (without knowledge of U_∞) as well, but interpretation of I_{isat} must be adjusted, using perhaps the general form of $I_{i,ram}$, given in Eqn. (4.12) when computing the ion density.

4.4.3 Resonance Effects

Plasma resonant probes rely on constructive interference between probe potential oscillations and natural plasma oscillations. At a frequency, $f_{resonant}$, near the electron plasma frequency, f_{pe} , resonance occurs, and a sizable increase in the DC collected plasma current occurs, $\Delta I_{d.c.}$. The theoretical resonant frequency for a spherical electrode is given by Eqn. (4.13). [54]

$$f_{resonant} \approx f_{pe} \cdot \left(1 + \frac{r_p}{5\lambda_D}\right)^{-2} \quad (4.13)$$

To avoid such resonance effects it is necessary to operate Langmuir probes at sweep rates significantly below the resonant frequency, $f_{resonant}$. The nonlinear nature of this extra plasma current ($\Delta I_{d.c.}$) leaves no immediate means to accurately remove this extra current (as one could attempt with extra flowing plasma current in the previous section). Since the electron plasma frequency is typically quite large (> 1 -GHz) this resonance is unlikely to be comparable to the rate of probe sweeping. Resonance near the ion-plasma-frequency does also exist, but the extra current is considerably less pronounced [54] and the magnitude of extra current is rather small, thus ion-plasma-frequency-resonance effects may usually be neglected.

4.4.4 Magnetic-Field Effects

Magnetic fields play crucial roles in many plasma systems including the ionizing closed-drift of Hall effect thrusters and plasma confinement in Tokamaks. In general, the effect of a strong magnetic field upon the collection of current by a Langmuir probe involves the restriction of charged carrier flux to the probe by limited cross magnetic field line charge motion. Now, when the oscillating potential of a rapidly swept Langmuir probe is thrown into a magnetic field, one generates an additional drift current collected by the probe. Theoretically, this extra polarization drift current is evaluated as shown in Eqn (4.14). [87, 88]

$$I_{pol.} = \frac{A_p \cdot (m_i n_i + m_e n_e)}{-B^2} \frac{dE_{\perp}}{dt}$$

$$I_{pol.}|_{V_B=V_f} \approx \frac{A_p n_o}{-\lambda_D B_{\parallel}^2} \left\{ \frac{Z_e m_e}{\left[\frac{m_i}{2\pi m_e} \right]^{-\frac{1}{2}}} + \frac{Z_i m_i \exp(-\frac{1}{2})}{\left[1 + \ln \left(\frac{m_i}{2\pi m_e} \right) \right]^{\frac{1}{2}}} \right\} \frac{dV_B}{dt} \quad (4.14)$$

Here, the magnetic field strength B_{\parallel} is taken as the component parallel to the axis of a cylindrical Langmuir probe; for a magnetic field perpendicular to the probe, the polarization currents on each side of the probe nullify each other. The second line of Eqn. (4.14) is evaluated at the surface of the probe where the electric field (using Poisson's equation with the Boltzmann relation) and thus dE/dt is non-negligible: $(dE/dt)_{surf.} \approx \lambda_D^{-1} dV_B/dt$. Also, a bias near the plasma floating potential is chosen (since the relative effect of the polarization current is greatest when $I_{probe} \approx 0$) to compute the probe-surface electron and ion densities in terms of the bulk plasma density n_o . Lastly, in Eqn. (4.14), the degree of magnetization, $Z_{e,i}$, terms are both zero in the majority of a HET plume since $r_{Li,e}/r_p \gg 1$ (however, very close to the thruster the electrons become magnetized as the electron Larmor radius approaches the probe radius, $r_{Le} \approx r_p$). While the lack of ion-magnetization in HET discharges causes the usually dominant ion polarization drift (often termed the "inertial drift") to disappear, the fully magnetized plasma in a Tokamak ($Z_{e,i} = 1$) is instead dominated by the ion polarization drift since $m_i \gg m_e$.

4.4.5 Capacitive Effects

Swift variations of a conductor potential generate leakage or displacement currents that follow the basic capacitance relation:

$$I \equiv C \frac{dV}{dt}. \quad (4.15)$$

For the rapidly swept HDLP data presented, the large voltages and short microsecond timescales lead to mA of leakage current ($\gg I_{isat}$) from tiny (1 pF to 1 nF) environmental capacitances. For a Langmuir probe, capacitive sources include probe-sheath capacitance to the plasma, probe-line stray capacitance to a ground plane, and probe-line mutual capacitance between neighboring conductors (see Figure 4.4).

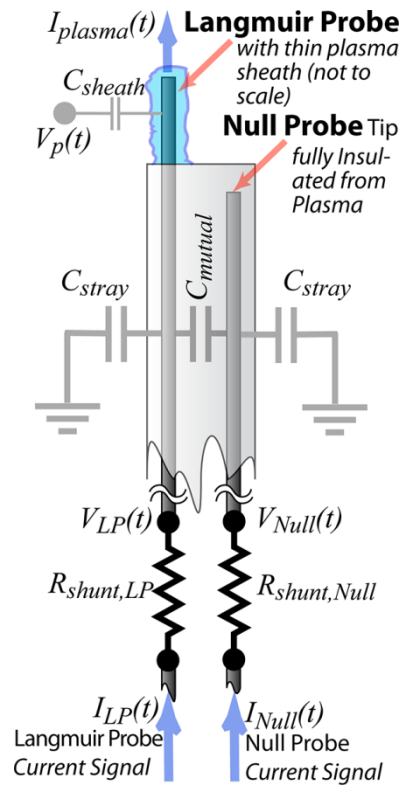


Figure 4.4. Schematic of HDLP configuration including effective sheath, stray, and mutual capacitances. The Langmuir and null probes maintain very close proximity to each other (< 10 -mm separation for over 10-m of cabling). The current measurement shunts are placed near the probe bias amplifier.

4.4.6 Sheath Capacitance

Experiments by Oskam, Carlson, and Okuda, in the early 1960's showed large sheath capacitive displacement currents ($I_{displacement} = C_{sheath} dV_B/dt$) drawn by a

special Langmuir probe for high-pressure (~ 1 torr) Neon and Helium discharges. [79, 89] The conclusions of these works showed that the effective sheath capacitance was greatest at higher plasma densities in agreement with reduced Debye lengths. This finding makes sense, and in a separate work by Crawford and Grard, [90] the sheath capacitance about a planar Langmuir probe was estimated (using two different methods including Child-Langmuir sheath thickness and a Boltzmann treatment) at the floating potential as:

$$C_{sheath}|_{V_B=V_f} \approx \alpha \frac{\epsilon_0 A_{probe}}{\lambda_D} \quad (4.16)$$

The non-dimensional factor, α , ranges from about 0.1 to 1 according to both theoretical treatments and experimental data, so a value of 0.5 is taken as a conservative estimate since the Child-Langmuir sheath thickness is known to under-predict the true sheath size (especially in collisionless plasmas with probe biases only a few factors of T_e below V_p). [91] In any case, within an order of magnitude, the sheath capacitance in Eqn. (4.16) provides a rough estimate of the capacitive effect of the plasma sheath about a Langmuir probe. For many probe/plasma measurements, this capacitance is on the order of a few picoFarads—a sufficiently small capacitance that can generally be ignored as a sweep rate limiter in many cases. However, for low-density ($n_e < 1 \times 10^{15} \text{ m}^{-3}$) and cool ($T_e < 1$ eV) plasma, the sheath capacitance about a swept probe may introduce sizable displacement currents when compared to the ion saturation current.

4.4.7 Stray Capacitance

Often referred to as parasitic capacitance, stray capacitance is formed between a conductor and its environment. Even a suspended bare wire in a vacuum meters away

from any conductive surface possesses nearly 10 pF per meter of length. Stray capacitance exists for every conductor, and while methods exist to minimize the incurred displacement currents, such capacitance cannot be directly eliminated. Estimating stray capacitance from geometry alone is non-practical, thus a direct measurement of the stray capacitance for a given configuration is often required. A measurement of the displacement (or leakage) current present from stray capacitance in a Langmuir probe setup is possible by simply measuring the current voltage characteristic (I-V curve) without any plasma present. For a symmetric triangular sawtooth bias voltage signal the dV/dt is constant during each sweep so that the measured current during each sweep is also constant with either $I_{disp} > 0$ for $dV_B/dt > 0$ or $I_{disp} < 0$ for $dV_B/dt < 0$. The alternative HDLP approach of simultaneously sweeping two closely positioned probes, a Langmuir and a null probe, allows direct measurement of the stray (and some of the sheath) capacitively generated displacement current. Direct numerical subtraction of the two synchronously measured currents yields the true plasma current (ignoring mutual capacitance):

$$I_{plasma}(t)^* = I_{LP}(t) - I_{Null}(t) \quad (4.17)$$

The dual probe configuration employed here is that drawn in Figure 4.4. The preceding removal of displacement current also serves to remove any extraneous noise EMI pickup by the probes since their close proximity ensures identical pickup in each probe—which is identically canceled upon subtraction. It is quite easy to produce leakage currents that exceed the ion saturation current. For example, in Eqn. (4.18), a

moderate 1 nF of stray capacitance (equivalent capacitance from 10 m of BNC cable) and a 100 V of bias sweeping over 1 μ s produces 100 mA of displacement current.

$$I_{leak} = C_{stray} \frac{dV_B}{dt} = (1 \times 10^{-9} \text{ F}) \times \left(\frac{100 \text{ V}}{1 \times 10^{-6} \text{ s}} \right) = 100 \text{ mA} \quad (4.18)$$

This is a large amount of current for most small Langmuir probes, and while its distributed nature will prevent the probe from melting, it may well saturate the probe bias amplifier or the current measurement circuitry. Even with the ability to correct for stray currents, it is important to use low-capacitance wiring (e.g. avoiding shielded wires like BNC cable) and low-capacitance feedthrus in order to keep the displacement currents to a minimum when sweeping rapidly.

4.4.8 Mutual Capacitance

The addition of a null probe (or shielded wiring) may induce mutually capacitive current flow between the separate conductors (C_{mutual} in Figure 4.4). However, since the dual probe configuration ideally involves biasing both probes in an identical manner, the voltage between the probes is zero and thus the current from mutual capacitance is also zero. Yet, in the common configuration using shunt based probe current measurement, the Langmuir probe may be drawing significantly more current than the null probe, which corresponds to a larger voltage drop across the sensing resistor and hence a voltage difference between the probe biases thereby setting up a mutual capacitive current. This effect can be minimized by avoiding shunts (and using split-core Hall current probes) or by using very small shunt resistors. Alternatively, the effect may be canceled out during post processing by adding the Langmuir probe and null probe current signals or by adding some terms to Eqn. (4.17):

$$\begin{aligned}
I_{plasma}(t) &= I_{LP}(t) + I_{Null}(t) - C_{stray} \frac{d}{dt}(V_{Null} + V_{LP}) \\
I_{plasma}(t) &= I_{LP}(t) - I_{Null}(t) + (2C_{mutual} + C_{stray}) \frac{d}{dt}(V_{Null} - V_{LP})
\end{aligned} \tag{4.19}$$

These expressions cancel mutual capacitance with estimations of stray and mutual capacitances and with numerically computed derivatives (capacitance estimation is possible in the ion saturation portion of the I-V characteristic where the Langmuir and null probe currents are closely matched). Generally, mutual capacitance is smaller than the stray capacitance and, in addition, the inter-probe dV/dt (the last term in Eqn. (4.19)) is smaller for the mutual capacitance current, thus in many cases mutual capacitive effects may be neglected altogether.

4.4.9 Alternative Capacitance Cancellation Technique

Another method of rapid sweeping, nearly as effective as the HDLP approach, is to employ double-shielded cabling (e.g. triaxial BNC cabling). In this configuration (common with space plasma measurements [92]) the inner-shield (or guard) and the central conductor are both simultaneously biased while a shunt resistor in-line with the center conductor provides a measure of current with virtually zero stray line capacitive current. In theory, this should provide better capacitance correction than the HDLP, yet in practice the rather large capacitance (1 nF is typical) between the guard-shield and outer-shield can destabilize or saturate many high-speed bias amplifiers. Also, extra attention is needed to eliminate or minimize capacitive sources such as feedthrus (a triaxial vacuum feedthru is required) and measurement circuitry since this configuration does not allow for measuring stray capacitance from sources other than the probe transmission line.

4.5 Summary of Temporal Sweeping Limits

The discussion in the preceding sections (4.4.1-4.4.9) is now distilled into a set of effective frequencies at which the particular effect occurs or creates a current equivalent to I_{isat} :

$$\begin{aligned}
 f_{transit} &\approx 2 \cdot f_{pi} \\
 f_{sheath-formation} &\approx \pi \cdot \left(3 + \frac{r_p}{\lambda_D}\right)^{-1} \cdot M_\infty f_{pi} \\
 f_{resonant} &\approx \left(1 + \frac{r_p}{5 \cdot \lambda_D}\right)^{-2} \cdot \sqrt{\frac{m_i}{m_e}} \cdot f_{pi} \\
 f_{polarization} &\approx \frac{2\pi \exp(-\frac{1}{2}) \cdot e \cdot B_{\parallel}^2 \cdot \lambda_D^2 \cdot \Delta V_B^{-1}}{Z_e m_e \sqrt{\frac{m_i}{2\pi m_e}} + \frac{Z_i m_i \exp(-\frac{1}{2})}{\sqrt{1 + \ln\left(\frac{m_i}{2\pi m_e}\right)}}} \cdot f_{pi} \\
 f_{sheath-capacitance} &= 4\pi \exp(-\frac{1}{2}) \left(\frac{T_e}{\Delta V_B}\right) \cdot f_{pi} \\
 f_{stray-capacitance} &= 2\pi \exp(-\frac{1}{2}) \left(\frac{A_p \epsilon_o}{C_{stray} \lambda_D}\right) \left(\frac{T_e}{\Delta V_B}\right) \cdot f_{pi} \\
 f_{mutual-capacitance} &= 2\pi \exp(-\frac{1}{2}) \left(\frac{A_p \epsilon_o}{C_{mut.} \lambda_D}\right) \left(\frac{T_e}{\Delta V_B}\right) \cdot f_{pi}
 \end{aligned} \tag{4.20}$$

Simplified by using the Debye length and the ion plasma frequency, $2\pi f_{pi} \equiv \sqrt{n_i e^2 / (m_i \epsilon_o)}$, this collection of sweep rate limits is quite similar, though more complete, to an analysis by Chiodini. [60]

The ion Mach number, $M_\infty = U_\infty / U_{Bohm}$, is included in the sheath formation frequency to incorporate the effect of a flowing plasma (for non-drifting plasmas with $U_\infty \leq U_{Bohm}$, set $M_\infty = 1$, as ensured by the presheath). Also, the bias sweep rate terms in Eqn. (4.20) have been evaluated for symmetric sawtooth probe bias signals using $(dV_B/dt)_{max} =$

$\Delta V_B f_{max}$, with f_{max}^{-1} equal to the time taken to slew ΔV_B , the peak-to-peak amplitude of a single probe bias sweep; for a sinusoidal sweep $(dV_{B,sin}/dt)_{max} = \pi \Delta V_B f_{max}$. In maintaining a probe sweep rate much lower than each of these limiting frequencies, one shall remain within the realm of conventional electrostatic Langmuir probe theory as expressed in Eqn.(4.21) .

$$f_{sweep} \ll \begin{cases} f_{transit}, f_{sheath-formation}, f_{resonant}, \\ f_{polarization}, f_{sheath-capacitance}, \\ f_{stray-capacitance}, f_{mutual-capacitance} \end{cases} \quad (4.21)$$

The first three limiting frequencies (transit, sheath-formation, and resonant) are rigid requirements that cannot be avoided. The later four limits (polarization and capacitive) are less restricting (e.g. with a HDLP, the stray capacitive limit is revoked) since the probe sweep rate may approach—or even exceed to some extent—these frequencies by only incurring minimal I-V trace distortion manifested primarily in the loss of I_{sat} and V_f accuracy. In some cases this I-V distortion can be removed; for example, by sweeping faster than the plasma variations (such that T_e and n_e are slowly varying constants) an estimate of the plasma capacitance *at each probe bias* is possible by comparing two consecutive (and opposite sign) bias sweeps.

For plasma conditions typical of a Hall thruster plume and Tokamak edge region, the computed tabulation of frequency limitations is presented in Table 4.1. A single Langmuir probe without capacitance compensation is unswepable at and beyond about 0.01-70 kHz for typical HET plasma conditions. Sweeping a single probe this fast will generate stray capacitive current to the probe on the order of the ion saturation current, which will distort the I-V characteristic. However, the addition of a null probe, in *using a*

HDLP, increases the maximum rate of sweeping by orders of magnitude, enabling sweep rates for both HETs and Tokamaks in the low-MHz range.

Table 4.1. Tabulation of Langmuir probe frequency sweep limits for typical Hall effect thruster and Tokamak conditions (near-wall and Scrape Off Layer (SOL) conditions are common Langmuir probe-able regions while the core is too hot to probe but included to show continued trends).

Typical Case	n_e [m ⁻³]	T_e [eV]	B [T]	f_{pi} [MHz]	$f_{transit}$ [MHz]	$f_{sheath-form}$ [MHz]	$f_{resonant}$ [MHz]	$f_{polariz.}$ [MHz]	$f_{sheath-cap.}$ [MHz]	$f_{stray-cap.}$ [MHz]	$f_{mut.-cap.}$ [MHz]
HET _{far-field}	10 ⁺¹⁵	1	2x10 ⁻⁴	0.6	1.2	7.1	140	∞	0.04	1x10 ⁻⁵	3x10 ⁻⁴
HET _{near-field}	10 ⁺¹⁶	5	0.001	1.8	3.7	8.6	350	∞	0.7	3x10 ⁻⁴	0.01
HET _{very-near-field}	10 ⁺¹⁷	10	0.01	5.8	11.6	11.8	516	4.2	4.4	0.005	0.11
HET _{internal}	10 ⁺¹⁸	20	0.02	18.3	36.6	14.3	559	10.6	28	0.07	1.5
TOKAMAK _{wall}	10 ⁺¹⁹	10	2	467	934	21	136	0.8	356	3.7	87
TOKAMAK _{SOL}	10 ⁺²⁰	20	2	1476	2952	30	93	0.5	2250	52	1224
TOKAMAK _{core}	10 ⁺²¹	2x10 ⁺³	2	4668	9336	813	17677	168	7x10 ⁺⁶	2x10 ⁺⁴	4x10 ⁺⁵

In Table 4.1, stray and mutual capacitances are calculated for 10-m of BNC cabling and parallel ribbon cabling (1 cm conductor-separation 0.5 mm wire O.D.) respectively with $\Delta V_B = 100$ V and $A_p = 16$ mm². Far- and near-field HET plasma is completely non-magnetized, while only the electrons are magnetized for very-near-field and internal cases. The usage of a HDLP removes the effect of stray capacitance (and mutual capacitance with proper setup) that otherwise limits the bias sweep rate to low-kHz values. For a HDLP in the far- and near-field of a HET, the temporally limiting feature is actually the probe sheath capacitance, which limits the sweep rate to about 0.04 to 1 MHz. In very-near-field and internal HET measurements, the magnetization of the electrons introduces an electron-only polarization drift that instead serves to limit the HDLP sweep rate to 4-11 MHz. For typical Tokamak edge-conditions, the lighter species along with the hotter and denser thermalized plasma suggest that one could sweep a HDLP at rates > 20 MHz, yet the fully magnetized plasma near the probe is affected

with a large polarization drift current that exceeds the ion saturation current at sweep rates $> 500\text{-}800$ kHz.

4.6 Conclusions

An exploration of seven temporally limiting features inherent to electrostatic Langmuir probe thin-sheath theory has significantly refined the estimate for the smallest-attainable temporal-resolution beyond the often-quoted limit of f_{pi}^{-1} . While the inverse ion plasma frequency is indeed a fundamental limiting timescale, the additional analysis herein detailed shows swept-probe capacitance effects distort the I-V characteristic at frequencies orders of magnitude below f_{pi} . However, use of a HDLP governed by relatively simple electrostatic thin-sheath theory enables one to sample the plasma properties of electron temperature, electron density, and plasma potential at near-microsecond timescales for a variety of HET and Tokamak plasma conditions. HET plume measurements with a 100-kHz HDLP show dramatic plasma fluctuations characteristic of a natural HET ionization instability (the so-call thruster "breathing mode" introduced in Section 1.5) and these results are detailed in Chapter 6, demonstrating the viability of the diagnostic and the limiting frequencies thus examined.

Chapter 5

Method of Spatiotemporal Data Fusion

One of the key advantages with Langmuir probes is the capability to perform measurements at excellent spatial resolution on the order of the probe dimension (typically a few mm). With time-averaged measurements, one can collect single-point (time-averaged probe I-Vs) measurements throughout large spatial grids, and then create spatially detailed contour maps of the plasma properties of electron density, electron temperature, and plasma potential. However, this is not *directly* possible with single-point non-averaged time-resolved High-speed Dual Langmuir Probe (HDLP) measurements collected throughout a large spatial grid, since the data span the domains of both time and space. While the time-domain data are fully uncorrelated, the frequency-domain data do possess meaningful information about the turbulent statistics of the plasma that one may compute correlations from. Specifically, a matrix collection of empirical discrete-time transfer functions is formed between the thruster discharge current (input) signal and the measured (output) electron density signals, thus estimating the thruster-plume system. Applying a fixed input signal measurement, the two-dimensional time-resolved response of the plume may be examined—revealing the structure and evolution of the plasma discharge. By employing this technique to HDLP data, discrete turbulent bursts of plasma are visually examined as the Hall thruster

exhales breaths of ionized propellant at velocities in excess of 12 km/s. [93] In effect, fusion in both the spatial and time domains is being used in this novel application.

5.1 Introduction

The full influence of breathing mode oscillations on thruster performance and lifetime is not well understood, and while the goal of this research does not directly assess these parameters, a method of visualizing the temporally resolved plasma flow field is achieved, providing unique and *unprecedented insight* into the HET discharge process. Key to enabling these visualizations are the newly developed HDLP (described in Chapter 3) diagnostic (for the measurement of electron density at 100 kHz) and the method of fusing together multiple single-point measurements into a single temporally-coherent 2D grid, which is the focus of this chapter.

5.2 Application of Spatiotemporal Fusion for Plasma Flow Visualization

In the field of fluid dynamics, various diagnostics enable direct 2D measurements of instantaneous flow field properties and fluid motions including: PLIF (planar laser-induced fluorescence), PIV (particle induced velocimetry), and LDA (laser doppler anemometry). However, in the turbulent rarefied flow of HET plasmas, these diagnostics have yet to be operated in a planar time-resolved manner, and are thus often limited to single-point time-averaged property and velocity measurements [94]. Thus, presented in this work, visualization of the plasma properties in a 2D time-resolved manner is investigated through data fusion of conventional single-point measurements. First, in Section 5.3, the experimental setup is summarized, then, in Sections 5.5-5.9, the applied theories of signal transformation (standard Fourier methods) are discussed in addition to their limitations and accuracy. A description of the employed algorithm is also presented

to detail the signal processing path followed to achieve the typical results shown in the final Sections 5.11 and 5.12. These results include single-point temporal and spectral signals as well as fully-fused 2D time-resolved frames of the plume electron density at different moments during a typical "breathing mode" type plasma oscillation. Additional results using this method of spatiotemporal fusion are included in Chapter 6.

5.3 Experimental Configuration Summary

The Large Vacuum Test Facility at the University of Michigan (see Section 2.1) provides the 6 m by 9 m low-pressure testing environment for a 600 W Hall thruster (see section 2.2) operated with a 200 V, 2 A, 2.6 mg/s xenon discharge (as in Figure 5.1).

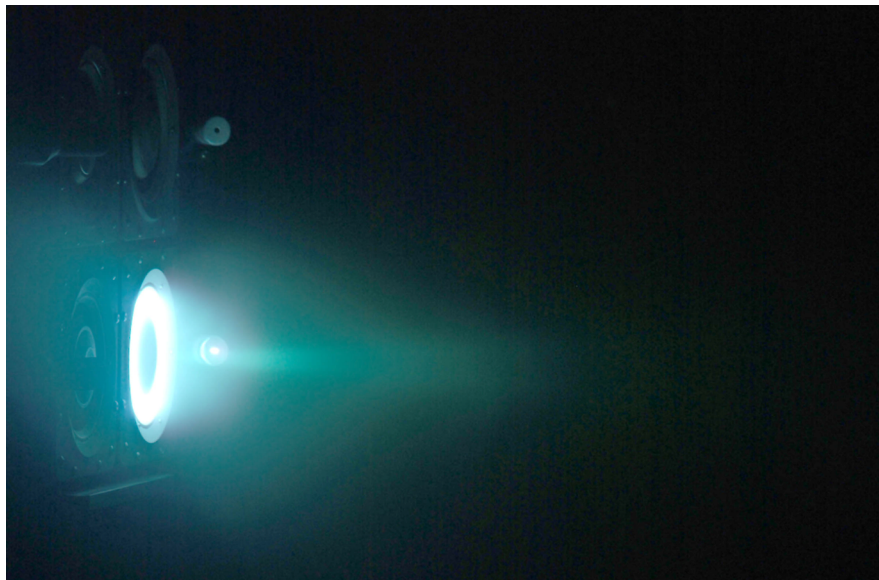


Figure 5.1. Photograph (1/2 sec exposure) of the Hall thruster plume discharged under vacuum conditions. Deceptively stable to the human eye, the exhausted plasma in this photo is violently oscillating at 19 kHz with signal peak-to-peak magnitudes nearly 100% of the DC mean. The thruster is part of a 4 engine cluster, but only single thruster operation is analyzed in this chapter (clustered results are included in Chapter 6).

Thruster discharge current, $I_D(t_p)$, is measured using a F.W. Bell NT-5 magnetoresistive current probe with a DC-100 kHz full-signal bandwidth and a DC-2 MHz small-signal bandwidth. Measurement of the plasma electron density, $n_e(t_p)$, is

performed using the HDLP (detailed in Chapter 3) with an effective bandwidth of DC-100 kHz. Comprised of a traditional cylindrical Langmuir probe along with a null (compensation) probe, conventional thin-sheath probe theory (examined in Chapter 4), is applied to attain estimates of the electron density, electron temperature, and plasma potential within typical accuracies (roughly $\pm 50\%$). A schematic of the experimental configuration was presented Figure 2.5, where digitally networked PCs automate the collection of data for a planar region in the plume measuring 31 cm by 50 cm. One PC controls a pair of positioning tables which move the Langmuir probe through each of the 352 grid points. At each grid point, another PC, interfaced to a high-speed DAQ system, collects 1 second of analog data, sampling simultaneously 4 independent channels of 16-bit 2-MHz A/D conversion (see Section 2.5). Table motion and DAQ for all grid points requires 3.5 hours and the collected raw binary data exceeds 10 GB (per thruster test condition).

5.4 Turbulent Statistics

The stochastic turbulent nature of the plasma oscillations within the plume of a Hall thruster limits the usefulness of time series data. However, by collecting a large sequence of time-domain data one should be able to estimate the statistically dominant features of the observed plasma oscillations. This empirical description of the plasma flow will be gathered throughout a 2D spatial grid, resulting in a set of statistical behavior data that serve to model the entire thruster plume system, both spatially and temporally. A single experimentally collected signal will then be fed as input to this model and the system response in a fully 2D and time-resolved manner will be simulated.

While other studies of turbulent flow structures have employed a method of analysis termed "phase averaging" for visualizing flow fluctuations [95, 96], here a different approach is taken and a set of empirical discrete time transfer functions are determined for which a single input allows estimation of the entire flow-field response. A severe limitation of common phase averaging techniques is their reliance on a single type of oscillation (one fixed-frequency) that is representative of the most probable fluctuation. Since phase averaging typically occurs in the time domain, a considerable amount of higher (and lower) frequency content is averaged away. The end result can reveal smooth turbulent structures, but these lack one-to-one correspondence to real instantaneous structures which retain their true stochastic turbulent nature.

5.5 Fourier Analysis

Strictly speaking, few (if any) turbulent flow fields can be fully described as linear time-invariant systems since the very definition of turbulence as a random non-linear chaotic-flow process contradicts such classification. However, at spatial length scales much larger than those of the non-linear turbulent dissipation, periodic structures may exist. For a collisionless HET plasma flow, the accelerated ions travel along approximately linear trajectories, and in the absence of strong applied magnetic and electric fields, such flows are quite amenable to linearized descriptions. In the plume region studied in this work, the weak electric and magnetic fields together with the collisionless or free-molecular ionized particle motion encourage the description of the flow as linear time-invariant with stationary stochastic statistics. Periodicity of the "breathing mode" oscillations in a narrow band about 18.6 kHz and the large degree of

similarity between different cycles of this mode help justify the assumption of stationary statistics.

It should be noted that in the very-near-field of the Hall thruster, where ionization collisions exist along with strong electric and magnetic fields, a Fourier description of the flow will likely lose considerable accuracy, and methods such as empirical mode decomposition via the Hilbert-Huang transform may provide a more useful description [97]. However, prior studies of the time-averaged HET plume properties (including electron density and thrust) in the same region investigated here, have revealed accurate linear super-positioning results (within a few percent) with the addition of extra thruster plumes [39,44]—again supportive of a linear assumption for the plasma flow process.

Thus, the application of a Discrete-time Fourier Transformation (DFT) may be realized as an accurate description of the flow in frequency (or wave number, k) space. Decomposing our discrete-time-series turbulent flow density into a mean DC component and a fluctuating component (with *random and periodic content*) we have:

$$n_e(x_n, y_m, t_p) = \overline{n_e(x_n, y_m)} + n_e'(x_n, y_m, t_p) \quad (5.1)$$

The fluctuation electron density, $n_e'(x_n, y_m, t_p)$, is the temporally dependant portion of the signal at distinct and discrete time-steps, t_p , for each of the spatial grid points x_n and y_m . Now, before applying a discrete Fourier transformation one needs to ensure the periodicity of this time series. To enforce this periodicity requirement, a Hann window is applied to the sequence. Defining for N consecutive and equally spaced time series data a set of N complex Fourier coefficients, $A(k)$, one may compute the DFT according to Eqn. (5.2).

$$A_{n_e}(n, m, k) = \sum_{p=0}^{N-1} n_e'(x_n, y_m, t_p) e^{-2\pi i k p / N} \quad (5.2)$$

For the data considered in this work, the indices range as: $n = 0, 1, \dots, 31$; $m = 0, 1, \dots, 10$; $k, p = 0, 1, \dots, N$. These indices correspond to evenly spaced radial positions from thruster centerline of -21 to 10 cm, axial positions downstream from the thruster of 10 to 60 cm, and $N = 2 \times 10^6$, respectively (for density signals upsampled to the rate of $I_D(t_p)$ collection). The resulting 32 by 11 matrix of Fourier coefficients contains nearly one billion discrete and complex valued elements. A 64-bit version of Mathworks MATLAB software is used to process these large data sets and perform the fast Fourier transformations. The limits of summation in Eqn. (5.2) are taken from $p = 0$ to $N - 1$, but for each different spatial location (e.g. x_n, y_m compared to x_{n+1}, y_{m+1}) this time sequence is offset by a finite and unknown amount due to the single-point scheme of data collection.

5.6 Empirical Transfer Function Estimation

The ratio formed by two sets of simultaneously sampled output and input discrete time Fourier transformed (using Eqn. (5.2)) signals represents the transfer function between these signals:

$$H(k) = \frac{A_{output}(k)}{A_{input}(k)}, \text{ for } k = 0 \text{ to } N - 1 \quad (5.3)$$

For each position, x_n and y_m , within the plume, one may compute an averaged sequence of transfer function coefficients:

$$\overline{H(n, m, k)} = \frac{1}{Q} \sum_{q=1}^Q \left[\frac{\sum_{p=\frac{(q-1)N}{Q}}^{\frac{qN}{Q}-1} n_e'(x_n, y_m, t_p) e^{-2\pi i k p Q/N}}{\sum_{p=\frac{(q-1)N}{Q}}^{\frac{qN}{Q}-1} I_D'(x_n, y_m, t_p) e^{-2\pi i k p Q/N}} \right] \quad (5.4)$$

where Q is the number of sets to average, for smoothing out the uncertain turbulent form of the flow-field statistics.

The linear nature of Fourier analysis prevents modeling the fully chaotic turbulent features of the plasma flow, however, as discussed in Section 5.4, one may estimate correlations in the linearly behaving "breathing mode" fluctuations with transfer functions of the form given by Eqn. (5.4). By averaging many sets of Fourier coefficients, some of the chaotic features of the flow are effectively averaged out of the empirically modeled thruster-plume system. Yet this averaging retains most of the originally measured transient behavior (See Figure 5.2)—suggesting that the plume flow is only weakly chaotic which supports earlier assumptions including stationary statistics. However, it is important to realize this formulation contains statistics for a wide bandwidth of possible plasma oscillations (nominally DC-100 kHz) and what might be thought of as chaotic when viewing the time-domain data may actually have statistical significance in the frequency domain. Thus, the averaging employed in Eqn. (5.4), removes (or attenuates) the truly chaotic signal features that may, for example, have been caused by one-time events such as a nearby lightning strike briefly disrupting the electronic signal level of the analog measurements.

In practice, for the data in this study, $Q = 10$, which cuts each N -point data sequence into $N/Q = 2 \times 10^5$ elements. This type of averaging is the simplest method of attaining a statistically accurate empirical estimation of the system of discrete-time

transfer functions. Averaging transfer function coefficients in this manner coarsens the discrete frequency resolution to $\Delta f = \frac{Q}{N} \Delta t^{-1}$ (the resolution is 10 Hz for datasets included with sample-rate $\Delta t^{-1} = 2$ MHz) but the low- and high-frequency structures—defined with widths >10 Hz in frequency space—are well preserved. It may appear unusual that in Eqn. (5.4) the fluctuating component of the discharge current signal, $I'_D(x_n, y_m, t_p)$, is specified for each location in the data collection grid, since the effective position of this current input signal is fixed at the position of the thruster. Yet in order to estimate the empirical transfer function at each point, a pair of *simultaneous* input and output signals are required, thus this notation is used to specify this temporally matched pair of signals.

Again, another thing to notice is that the discretized temporal sequence t_p is arbitrarily offset for each positional pair of n_e and I_D since the manner of sampling each pair of single-point measurements involves considerable delays >30 sec between each instance of high-speed analog signal collection. Fundamentally, the purpose of these averaged transfer functions is to produce a set of n_e and I_D for all spatial locations that share a common temporal sequence t_p^* that is devoid of incoherent offsets.

5.7 Limitations of the Estimated Transfer Function

Although the input signal to the system under identification is easily measured, it is not directly controllable. Physically, the power supply driving the Hall thruster plasma discharge is operated in voltage-control mode maintaining a fixed electrostatic ion accelerating anode potential. The breathing mode oscillations (≈ 19 kHz in this work) dominate the form of the generated discharge current signal that is taken as the input to the empirical thruster-plume system. The energy of this signal is predominantly

distributed at the DC end of the spectrum and in a narrow (full-width at half-maximum of about 1 kHz) band centered on the breathing mode frequency. Thus, by only exciting the system at one frequency, the identified system may contain considerable uncertainty at other frequencies where the input power spectral density is low. Resolution of this issue is possible through a combination of very large, multi-million element data sets (averaged as in Eqn. (5.4)) and high signal-to-noise ratio analog measurements (SNR > 80 dB, see Sections 2.5 and 3.6). Thus, the computed matrix of empirical transfer functions will provide accurate responses to inputs similar in spectral content to those which generated the transfer functions. This implies that one should not use this empirical model to evaluate the response of generic artificial input signals (e.g. a square-wave Heaviside response). Therefore, by only using an original measured input discharge current signal as input, one may effectively and accurately measure the system response to a signal that is properly modeled by the system.

Regarding control of the input signal, it is noted that while attempts have been made with closed-loop feedback control of these breathing mode oscillations (see reference [98]) in real-time, they appear to play a key role in the discharge process that, while not fully understood, may lead to improved thruster performance. Active dampening or amplification of the breathing mode oscillations is challenging due to the high-speeds (10-60 kHz), high-voltages (100-600 V), and non-linear nature of the very-near-field discharge process.

5.8 Fourier Synthesis of Data

Once a complete matrix of empirically estimated transfer functions is computed for the entire planar set of grid-points, a single input is applied and response computed in wave number (or frequency) space as:

$$A_{n_e}|_{synth}(n, m, k) = \overline{A_{I_D}^*(n^*, m^*, k)} \cdot \overline{H(n, m, k)} \quad (5.5)$$

where the indices n^* and m^* are constants and refer to the measured discharge current at a *fixed* position while the bar over this set of Fourier coefficients implies averaging similar to Eqn. (5.4). This single sequence $\overline{A_{I_D}^*(k)}$, is multiplied against each distinct empirical transfer function (k^{th} element by k^{th} element for $k = 1$ to N/Q), such that the computed matrix of Fourier coefficients $A_{n_e}|_{synth}(n, m, k)$ is a set of wave space responses to a single input. This thereby simulates the entire thruster plume response, to a specific set of originally discretely sampled analog discharge current values $I_D^*(t_p^*)$. This synthetic sequence will contain N/Q elements and thus with transfer function averaging (Eqn. (5.4), for $Q > 1$) the sequence will be an integral factor shorter. Finally, with the application of inverse discrete Fourier transformations, one obtains a set of two-dimensional time-aligned and time-resolved electron density measurements using Eqn. (5.6).

$$n_e'|_{synth}(x_n, y_m, t_p^*) = \frac{Q}{N} \sum_{k=0}^{N/Q-1} A_{n_e}|_{synth}(n, m, k) e^{\frac{2\pi i k p Q}{N}} \quad (5.6)$$

$$n_e|_{synth}(x_n, y_m, t_p^*) = \overline{n_e(x_n, y_m)} + n_e'|_{synth}(x_n, y_m, t_p^*)$$

Here, the measured time-averaged mean electron density at each grid-point is included to complete the synthetic reconstitution of the signal.

5.9 Accuracy of Synthesized Signals

The dualism inherent to the Fourier transformation, \mathcal{F} , ensures that in the absence of signal filtering, a synthetic signal will exactly match the initial signal, thus:

$$\mathcal{F}^{-1}\{\mathcal{F}\{n_e(t_p)\}\} = n_e(t_p) \quad (5.7)$$

However, this equality does not hold when averaging is performed as in Eqn. (5.4). For the turbulent plasma data measured, the application of averaging reveals the main periodic flow structures while suppressing the more chaotic turbulent features. Additionally, noise potentially introduced in the determination of the temporally resolved plasma electron density may not be negligible. Indeed, the absolute accuracy of a conventional Langmuir probe is typically $\pm 50\%$ (Section 3.8 propagated the uncertainty of the HDLP to about $\pm 20\%$). Thus, the application of averaging the flow statistics in frequency space is critical for ensuring that the fluctuating component of electron density is associated with the plasma flow, and not uncertainty and measurement noise.

The quality of a synthesized electron density signal obtained with Eqn. (5.6) is demonstrated in Figure 5.2:

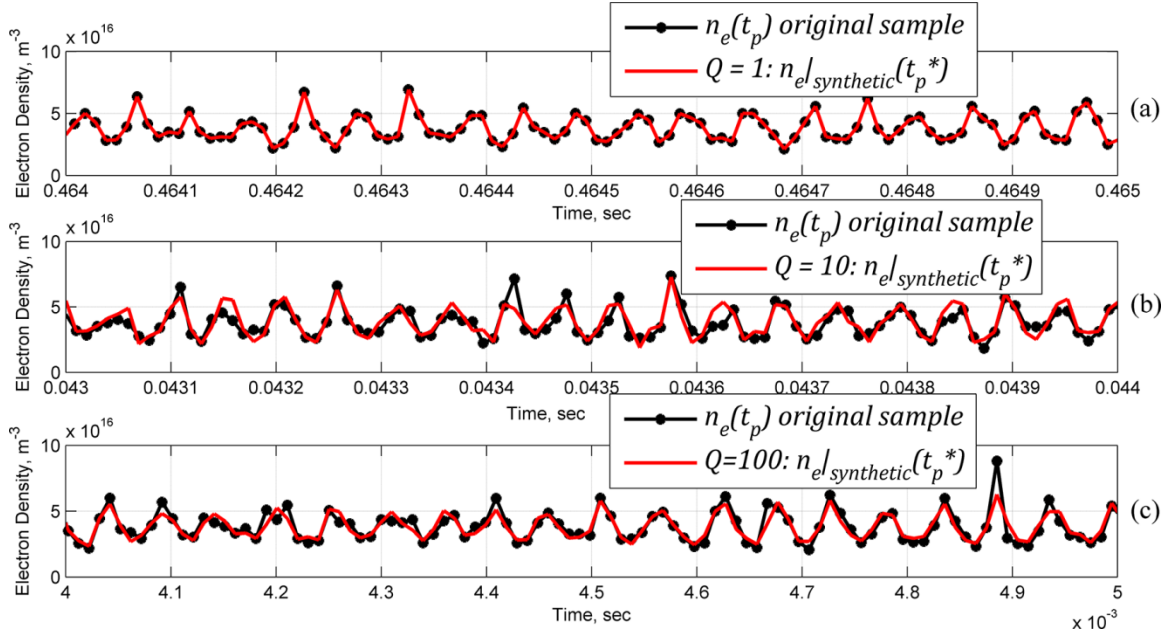


Figure 5.2. Quality of synthetic signals versus original signals for three different degrees of transfer function averaging: (a) no averaging, $Q = 1$, (b) $Q = 10$, and (c) $Q = 100$. *Due to sample length reduction by Q , a different portion of the signal is evaluated in each plot.* The synthetic result is taken from the $n_{e|synth}(x_n^*, y_m^*, t_p^*)$ position so that a direct comparison with original data may be shown.

The method of applied transfer function averaging appears to preserve the important features of the signal whilst losing spurious aspects that may originate from chaotic flow behavior or from measurement noise. The characteristics of the synthetic signals for $Q = 10$ and $Q = 100$ appear very similar; thus, to ensure a sufficient length of time series data, $Q = 10$ averaging is used, providing 10,000 samples of synthesized time-series data (spanning 100 ms, when originally 1 sec at 100 kHz was collected). The uppermost data in Figure 5.2(a) exhibit the exact duality of Fourier analysis which occurs when the transfer function is un-averaged ($Q = 1$).

5.10 Overview of Signal Processing

In anticipation of turbulent flow fluctuation analysis, large seamless multimillion element raw analog sample-sets are collected at each plume grid-point. Namely, 100,000

full I-V traces are conducted back-to-back over 1 second to ensure the gathering of enough information regarding the turbulent flow statistics. Complete post-processing, from raw analog to digital data, to fully synthesized 2D time-resolved results (as in Eqn. (5.6)), is computationally intensive, requiring in excess of 100 hours to process 352 grid-points (20 GB of binary data) with a 64-bit OS on an 8-core 3-GHz PC. About 4,000 lines of parallelized MATLAB code were written to perform this post-processing.

The first task, after converting raw binary data into respective probe voltages and currents, is to remove the stray capacitance current (and EMI) from the Langmuir probe signal. This step entails a direct point-by-point subtraction of the Null probe measured current from the Langmuir probe measured current at each 0.5 μ s time-step, using Eqns. (3.1) and (3.3). The time-resolved plasma properties are then determined using a developed MATLAB function capable of processing about 300 I-V characteristics per second. Corrected probe plasma current and voltage signals are chopped into individual I-V trace sets (with one or two edge points clipped out and symmetry correction applied) and time-stamped at their center. The I-V characteristics are then interpreted using standard collisionless non-magnetized thin-sheath Langmuir probe theory found in standard texts [52-56] and outlined specifically for the HDLP in Section 4.3.

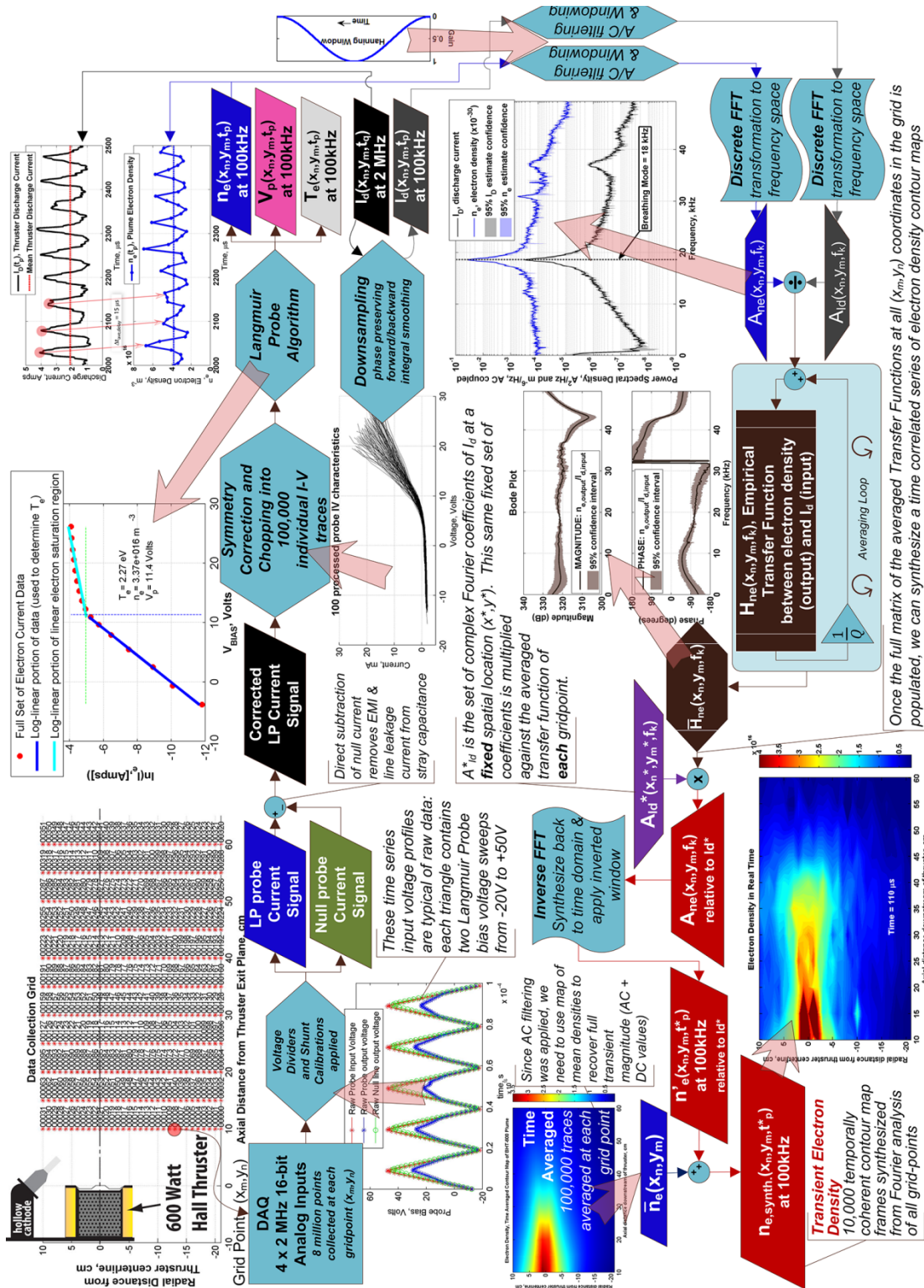


Figure 5.3. Flowchart of signal processing steps from raw ADC in upper-left to (clockwise) 2D time-resolved density.

Displayed in Figure 5.3 is an overview of the various signal processing steps taken in the method of spatiotemporal data fusion herein described. The upper-half of this

figure details the conversion of raw voltage signals into meaningful signals including the thruster discharge current (in Amperes) and the plume electron density (electrons/m³). At this point, the data streams can all be upsampled to 2 MHz (rate of $I_D(t_q)$ collection) or downsampled to 100 kHz (rate of $n_e(t_p)$ collection). Since the bandwidth of our current probe was between DC-100 kHz (full signal bandwidth) and DC-2 MHz (small signal bandwidth), upsampling is not entirely necessary to prevent significant loss of signal information. However, for the data presented in this work, upsampling has been applied to all signals in order to align a third independently measured 109.5 kHz high-speed camera signal that is occurring simultaneously with the other signals (FASTCAM see Section 2.4). The finer temporal grid at 2 MHz serves then to reduce the interpolation uncertainty between the various multi-rate signals. The upsampled signals are all fitted (without smoothing) to piecewise cubic-Hermite interpolating-polynomial spline representations and these are then evaluated along a linear time grid (with 0.5 μ s spacing) with the continuous-time (piecewise-interpolated) polynomial terms. An added benefit of this higher rate is that constructed video animations of the plume may be encoded at standard NTSC rates with 30 frames/sec. This frame-rate results in more visually appealing frame transitions that reduces the visual cycle of the 19 kHz thruster breathing mode plasma oscillation to about 16 breaths per minute (coincidentally, the human average). The lower-half of Figure 5.3 details the estimation of the thruster plume system model (discussed in Section 5.6) and subsequent synthesis of two-dimensional time-coherent electron density contour maps (lower-left).

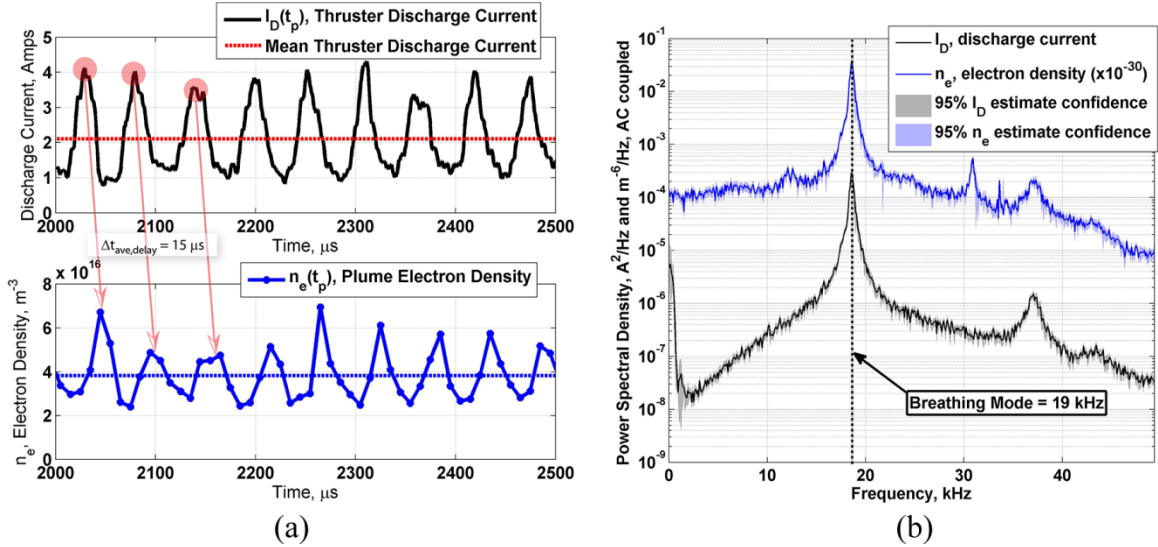


Figure 5.4. (a) Time domain discharge current and electron density transients (measured with HDLP) and (b) the respective power spectral densities of these signals in the frequency domain ($Q = 100$ in (b) data). Position is 15 cm downstream from the 600 W HET for both (a) and (b).

5.11 Data Fusion Results

After converting raw time-series data to signals of time-resolved current and electron density, long sequences of data are obtained, and 0.5 ms of these data are presented in Figure 5.4(a). The strong correlation in discharge current and electron density fluctuations is critical to the success of this data fusion method. With poor correlation between the input and output signals, the system model created by the collected matrix of empirically estimated transfer functions would be meaningless. The existence of strong plasma density fluctuations at 18 kHz is made clear in the time domain with examination of single-point time-series signals, but examination of the collective plume behavior requires application of the aforementioned Eqns. (5.4)-(5.6). A matrix collection of estimated empirical transfer functions is used to model the thruster plume system and the Bode plot from one element belonging to this set is displayed in Figure 5.5. The relatively flat magnitude response in the 10 to 37 kHz band describes a

nearly constant linear relationship between fluctuations in the discharge current and electron density signals. The phase provides the temporal relationship between the signals, and for the breathing mode oscillations, at 18.6 kHz, we find $\Delta t_{delay} = \frac{\phi}{2\pi} \frac{1}{f} = \frac{105^\circ}{360^\circ} \frac{1}{18.6\text{kHz}} = 15.7 \mu\text{s}$ a result in direct agreement with Figure 5.4(a). An important characteristic of the Bode plot averaged transfer function is the low-scatter of points in the vicinity of the 19 kHz breathing mode frequency. As was discussed in Section 5.7, this comes about through the breathing mode role as the system input and with a majority of the signal energy (see Figure 5.4(b) PSD plot) deposited in this mode, the estimation confidence of the system response for this band is quite accurate.

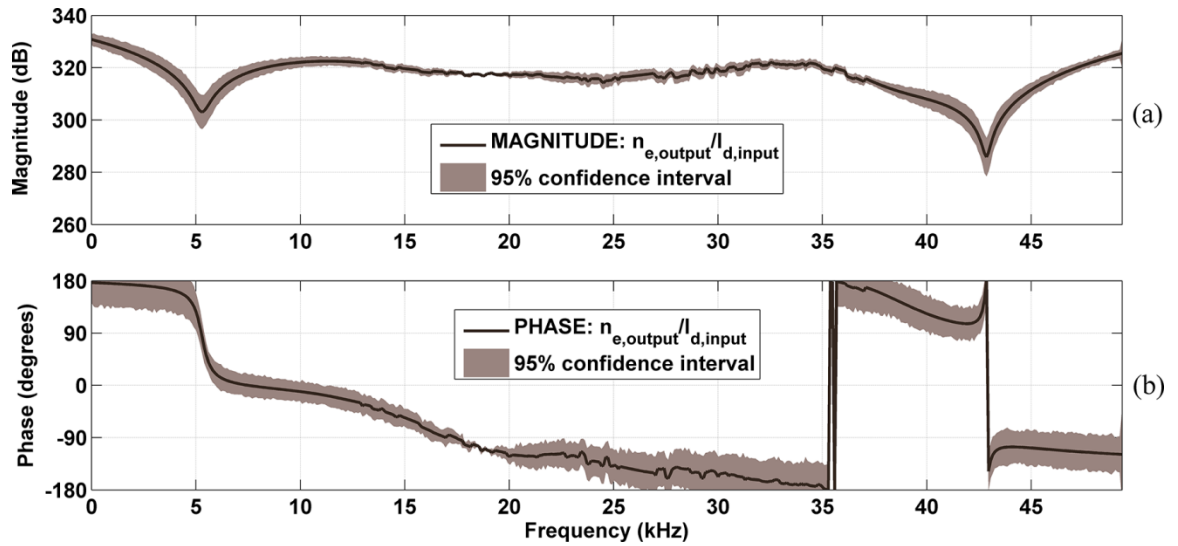


Figure 5.5. Bode plot of a single-point (15 cm downstream) transfer function from the thruster plume empirically estimated system showing (a) magnitude and (b) phase between discharge current and electron density. Smoothing has been applied.

The dominance of breathing mode oscillations in the operation of the investigated 600 W Hall thruster is remarkable. To put their magnitude into perspective, the power contained in a 400 Hz band centered on the peak in the discharge current PSD at 18 kHz is computed next in Eqn. (5.8).

$$\begin{aligned}
Power|_{breathing-mode} &= V_D \cdot I'_{breathing-mode} \\
&\approx V_D \cdot \sqrt{PSD(18 \text{ kHz}) \cdot \Delta f_{FWHM}} \\
&\approx (200V) \cdot \sqrt{2.9 \times 10^{-4} A^2/Hz \cdot (400 \text{ Hz})} \\
&\approx 68 \text{ Watts}
\end{aligned} \tag{5.8}$$

This represents a significant fraction, namely $\sim 15\%$, of the total thruster power since for this operational condition the total DC power drawn by the thruster was measured as 420 Watts (for thruster discharge voltage, $V_D = 200 \text{ V}$). In the preceding power estimate, the fluctuating current amplitude was approximated by considering the area under the peak maximum value with the frequency band, Δf_{FWHM} , as the full width at half maximum. Complete integration of discharge current signal power at all frequencies above DC reveals 88 Watts. Finally, it is noted that evaluation of the non-AC-coupled non-windowed discharge current signal upholds Parseval's theorem with total signal power matching total thruster power.

In terms of thruster efficiency, the residence of this large signal power at the breathing mode emphasizes its importance. A clear correlation between the power in this modal feature and its effect on thruster performance has yet to be quantified; however, qualitative performance is often improved for certain magnitudes of breathing mode current oscillation. [16, 27] The improvement may result from the breathing mode role in the propellant ionization process as well as its effect on cross-field electron transport inside the thruster.

5.12 Typical Spatiotemporally-fused Density Contour Maps

The method of data fusion presented in this chapter was developed for the purpose of constructing time-resolved two-dimensional maps of the thruster exhausted electron

density. While most results with this method are included in the following Chapter 6, a typical time sequence of electron density color-contour maps is presented in Figure 5.6.

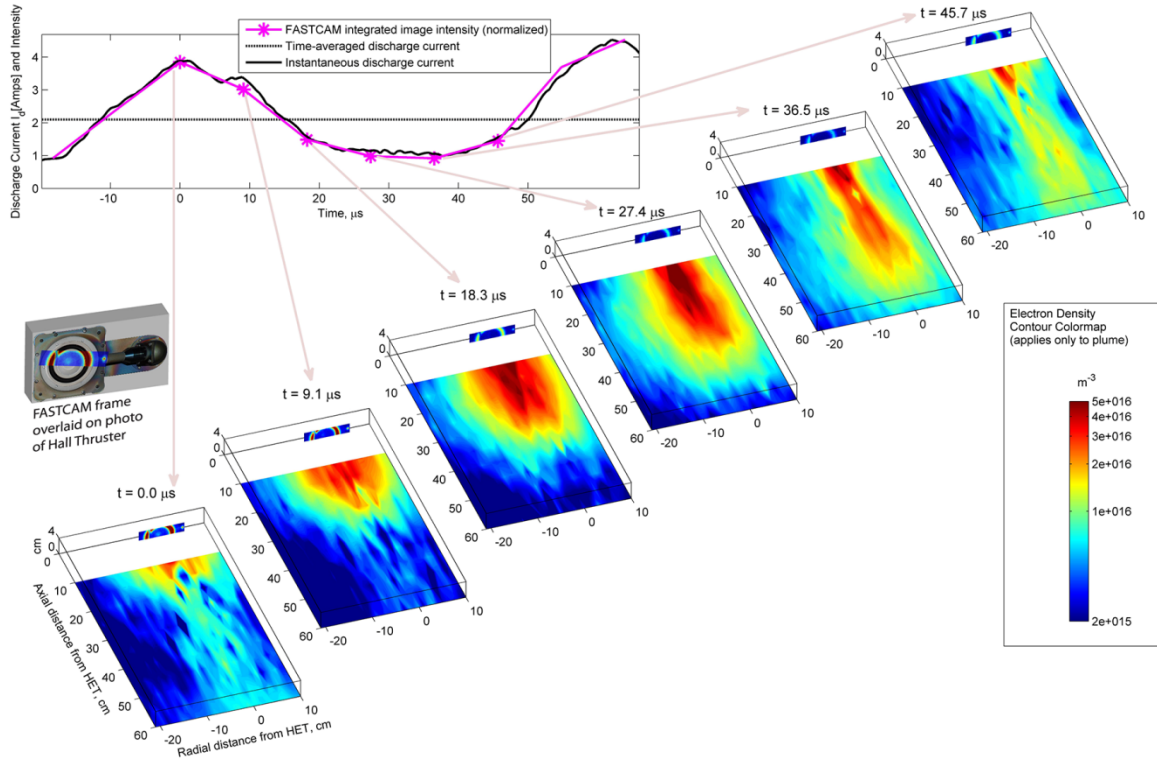


Figure 5.6. Typical data fusion results for time-resolved two-dimensional electron density contour maps in the plume downstream from a Hall thruster. This 46 μs sequence of the plasma evolution was synthesized from an empirically estimated transfer function model of the measured thruster plume system using Eqns. (5.4)-(5.6). Simultaneously acquired FASTCAM high-speed photographs of the HET are included for each density frame.

These frames show a single period or "breath" of the breathing mode oscillation occurring at 19 kHz. In Figure 5.6, the coordinates $x = 0 \text{ cm}$ and $y = 0 \text{ cm}$ refer to the fixed thruster location. The exhausting of the plasma into vacuum undergoes a rapid decay in density (proportional to $1/r^2$, with r as distance to thruster) as the jet expands due to natural thermal diffusion. Thus, a logarithmically scaled contour colorbar is used to better track the emitted breathing mode density waves. Even so, the enormous ion speeds, ranging from 10 km/s to nearly 13 km/s, enable turbulent bursts of ejected plasma to reach the edge of the planar measurement region as fully intact structures.

In addition to the thruster discharge current and electron density, a third signal (magenta trace in upper left of Figure 5.6) is included that corresponds to the plasma photo-emissive integrated image intensity measured at the thruster. Both the photo intensity and discharge current are signals that physically exist centralized near the location of the thruster, placing them in phase with each other. The spatial motion for a breath of ionized plasma is well portrayed in this brief temporal series of 2D electron density contours. Combining thousands of consecutive frames into density contour map animations produces a dramatic visualization of the Hall thruster breathing mode oscillation. The unique plume response to each unique cycle of the discharge current oscillation is testament to the effectiveness of the applied methods of Fourier analysis, empirical transfer function estimation, and the final synthesis of time-coherent multi-dimensional data. In the linear sense, longer discharge current cycles set up longer and wider bursts of plasma density, while higher amplitude current signals affect larger magnitude electron density levels. The capacity of the Fourier transformation for describing the non-sinusoidal character of the measured temporal waveforms (as seen in Figure 5.4(a)) through frequency distributed phase and magnitude information, results in accurate thruster-plume system estimation. This allows specific frequency features to travel faster (or slower), which the Bode plot non-linear phase profile may suggest (but the uncertainty from turbulence and noise is too great to be certain).

5.13 Method of Data Fusion Conclusions

Starting with a set of high-speed single-point measurements of the plasma density in the plume of a Hall effect thruster collected individually throughout a planar region, fusion of these temporally incoherent spatial measurements was attained by synthesizing

the response of the thruster plume system modeled with a matrix collection of empirically estimated discrete transfer functions. The resulting time-resolved two-dimensional visualizations of the plasma exhaust from the HET show large turbulent plasma structures ejected at nearly 13 km/s. Additional results from this method and HDLP data along with full discussion is included next in Chapter 6.

Chapter 6

Time and Space Resolved Plume Measurements

Hall thrusters and many other plasma discharges are known to exhibit fluctuations that predominantly reside in the low-frequency band 1 kHz to 1 MHz. [16, 65, 66] A great many of these observations are made by analyzing the fluctuations of floating (or fixed-bias) electrostatic probes [18, 99] or simply by examining the voltage and current signals maintaining the plasma discharge. Yet quantitative fluctuation measurements of plasma properties include density, electron temperature and plasma potential are less common. This chapter begins with a brief examination of the nature of fluctuations observed visually and within the discharge current driving a Hall effect thruster, and then goes on to explore the nature of similar fluctuations observed within the downstream plasma plume in unprecedented spatial and temporal detail. These measurements shall reveal a plume rich in oscillatory behavior dominated by the Hall thruster breathing mode. The observed dynamics of the breathing mode may in part serve to increase thruster performance by making use of hotter ionization waves whilst maintaining relatively cool time-averaged electron temperatures.

6.1 Deceptively Smooth HET Operation

To the human eye, a nominal Hall effect thruster (HET) discharge appears quiescent and steady, and the discharge voltage and current readings displayed on the power supplies running the thruster encourage this viewpoint. In Figure 6.1 a series of

photographs taken with identical exposure settings reveal a smooth plume structure emanating from the thruster.

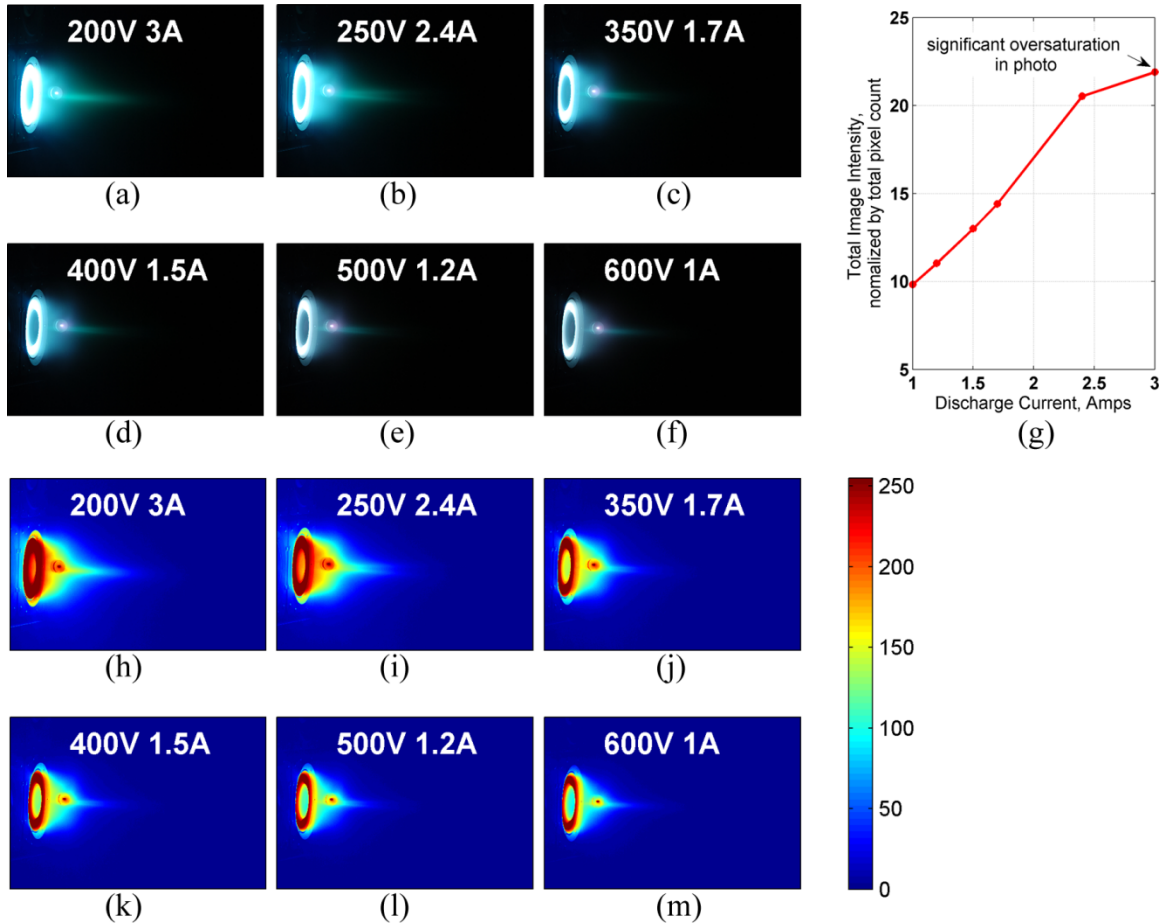


Figure 6.1 Sequence of visual (a)-(f) non-filtered optical photographs (color-scaled for (h)-(m)), taken with Nikon D80 camera using a 300 mm lens stopped down to f/13 and exposed for 1/3 s at each of the 600-W Hall thruster discharge voltage and mean discharge current settings listed. (g) Shows the integrated total image intensity for each photograph, which is seen to scale roughly linearly with the mean discharge current.

Deceptively stable at these camera settings and to human eye, the exhausted plasma in these photos is violently oscillating at more than 15 kHz with signal peak-to-peak magnitudes nearly 100% of the DC mean. All Hall thrusters exhibit some degree of breathing mode oscillations, but even so, the optimization and design process used to develop HETs is based largely on time-averaged measurements and modeling results.

6.2 Visual HET Startup Sequence

With its high frame rate, the FASTCAM high-speed imaging system (see Section 2.4) permits detailed non-intrusive time-resolved views of transient phenomena in Hall thrusters. Imaging a portion of the HET discharge channel (shown in Figure 6.2), Figure 6.3 displays a dramatic sequence of optical intensity data acquired during the first millisecond of thruster startup in voltage-control mode. Each color-scaled photo is time-stamped with the time from the activation of the discharge power supply. The optical image intensity (obtained by integrating total photo pixel intensities) and corresponding discharge current signals are in phase and fluctuate with similar relative magnitudes. Following the initial 15-A current spike, the HET breathing mode oscillations are readily visualized in both the optical intensity and discharge current data. In addition, these optical images indicate the presence of azimuthal asymmetries present in the discharge channel at orbit frequencies of a few kilohertz. Affectionately termed "gerbils," these azimuthal fluctuations or "spoke instabilities," [16,] appear related to the Hall current inside the discharge channel. The capability of these gerbils to set up azimuthal electric field fluctuations (\tilde{E}_θ as in Eqn. (1.9)) leads to a cross-magnetic-field electron drift in the axial direction. [20]

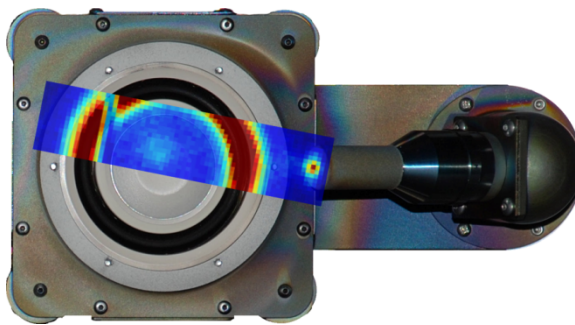


Figure 6.2. Overlay of color-scaled FASTCAM frame, showing the imaged portion of the 600-W HET discharge channel.

While indications of gerbils or spokes have appeared in other HET experiments [18, 100] and are under continued study for their possible role in cross-field flux, the only appearance they make in this work is in Figure 6.3, due to their localization to the very-near-field and internal discharge regions that are not captured with the HDLP positioned in the downstream plume. Future internal HDLP measurements would certainly help illuminate the behavior and origin of these azimuthal asymmetries.

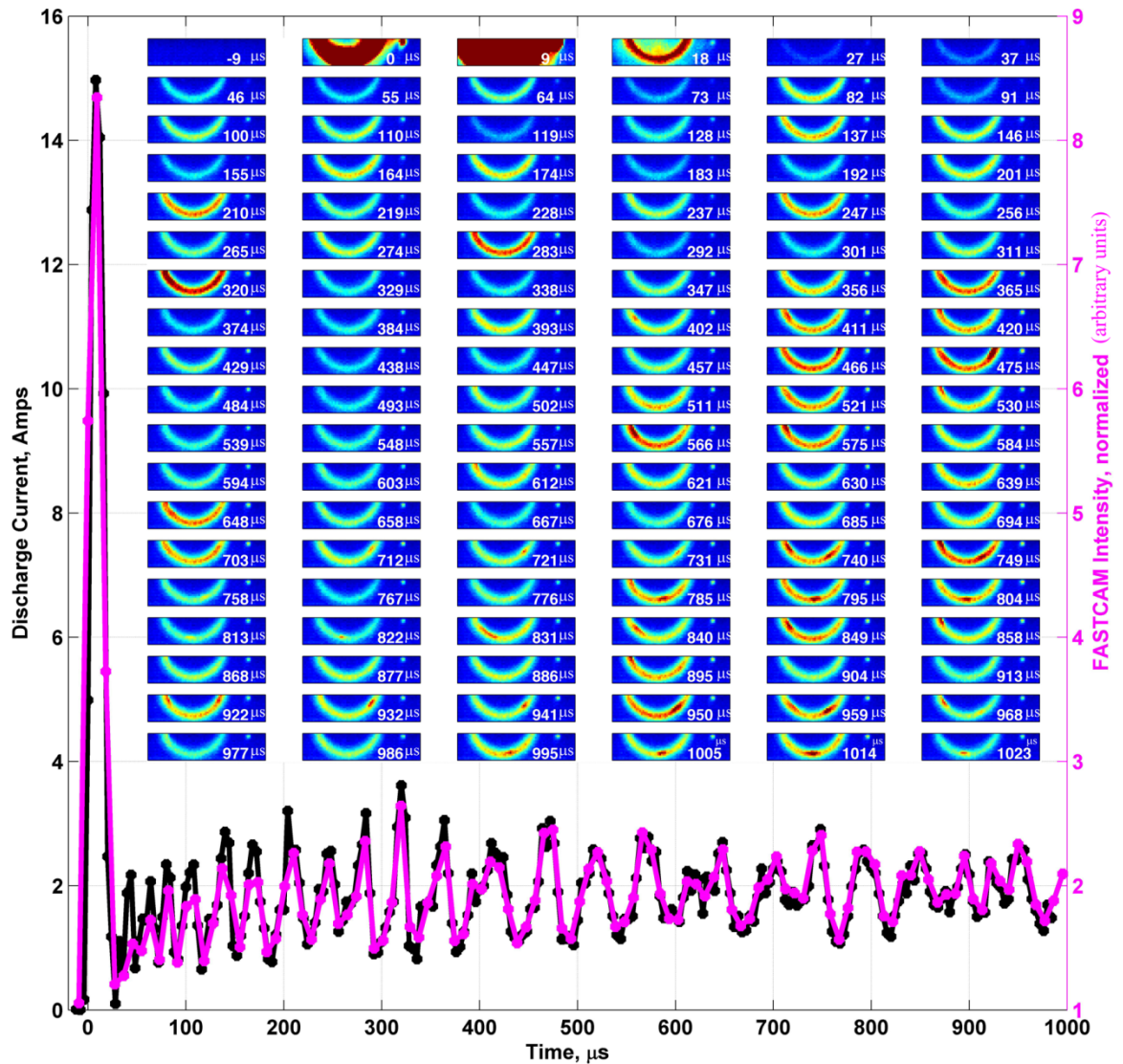


Figure 6.3. startup at 300-V, 2-A discharge. The high-speed optical images, limited to half of the anode as well as the entire cathode, are time-stamped (in microseconds following start of discharge) and presented as intensity plots with warmer colors corresponding to higher intensities.

While the data in Figure 6.3 are typical for powering up a HET, there does exist dependence of the startup sequence upon the characteristics of the discharge power supply. Namely, the finite voltage slew-rate of the supply (about 100 V/ms here) will prevent instantaneous electrical response to the commanded discharge settings, and this effect is apparent in the initial startup transient seen in Figure 6.3. In some thruster operation configurations the power supplies are slowly ramped up to the desired set point, a practice performed partly to avoid transients such as in Figure 6.3. Yet, slowly ramping the voltage may not actually be helping a given thruster's long-term lifetime since the longer durations at the very-low-voltage settings (where thruster losses are greatest), may actually increase transient-startup erosion of the thruster walls. Time-resolved erosion measurements could perhaps help determine the most effective manner in which one should startup a Hall thruster. Steady-state operation of the HET thruster sequence shown in Figure 6.3 occurs within about 10 ms corresponding to the response time of the discharge power supply. Yet this so-called steady-state operation still exhibits a strobe like optical emission behavior due to the breathing mode oscillations. However, in this steady-state, the magnitudes and periods of the individual fluctuations stabilize. Thus far, no effort has been made to quantify the FASTCAM high-speed image intensities. The camera detected a broad (unfiltered) light spectrum predominantly in the visible spectrum, and the use of line specific filters to isolate specific Xe states [101] was avoided to ensure sufficient light transmission to the camera. Qualitatively, however, the camera confirms the existence of the plasma optical emission transients that are in close relation to the observed discharge current oscillations. In this manner, the unsteady

emission of photons appears to be the result of increased atomic state transitions associated with the bursts of ionization characteristic to the HET breathing mode.

6.3 Hall Thruster Discharge Current Oscillations

Measurements of the Hall thruster discharge current oscillations are abundant [102, 103, 104, 105, 106, 107, 108] in the literature of HET research. Less common are studies of thruster performance versus the magnitude of these oscillations. Early Russian literature [27] has implied the avoidance of highly oscillatory regimes (oscillations often will diminish with increasing magnetic field strength) when operating a HET. However, this approach may not result in the most efficient thruster performance since the critical magnetic field settings generally observed to have the highest performance are generally accompanied with the largest amplitude discharge current oscillations. [27, 16] In a study by Hofer and Jankovsky, peaks in thruster efficiency were typically observed when the discharge current oscillation magnitudes also peaked. [102] While the performance effects of breathing mode and other low-frequency oscillations are under continued study, the prevalence of these oscillations in the high-efficiency ($> 50\%$) modern HETs such as the 600-W HET used in this study, suggests that they play some role (likely temporally enhanced ionization) in enhancing performance for certain operating conditions.

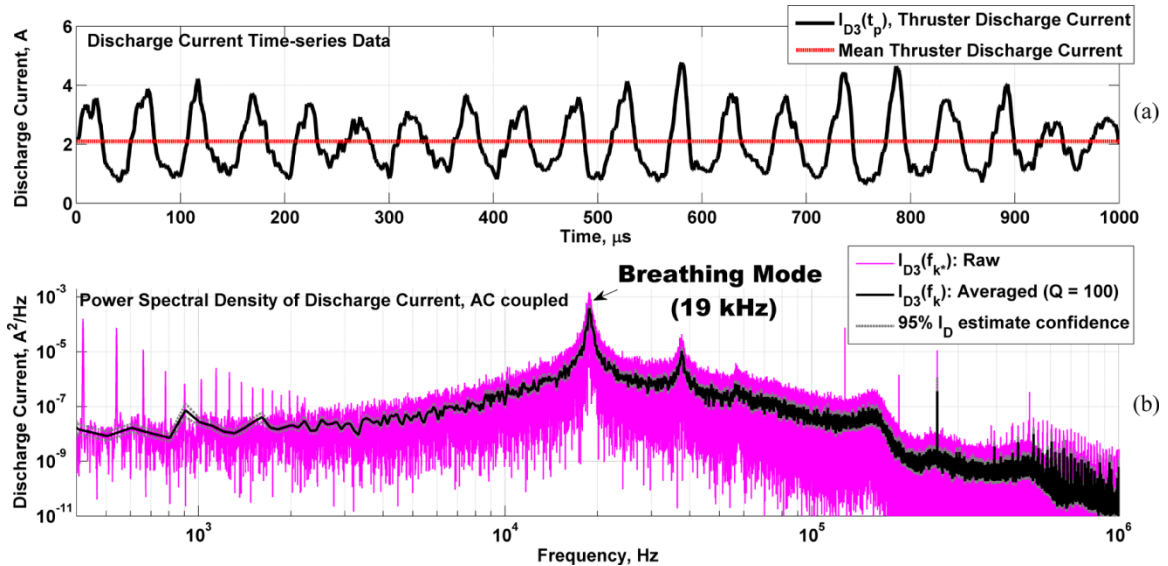


Figure 6.4. Thruster discharge current signal in (a) time domain and (b) frequency domain. 95% confidence interval shown for power spectrum estimate with $Q = 100$ terms averaged. 200 V 2 A thruster settings.

In Figure 6.4, typical discharge current data are presented both in the (a) time domain as well as (b) the frequency domain using the FFT of the time series data properly scaled to the Power Spectral Density (PSD) units of A^2/Hz . While the time series form of the discharge current signal, $I_{D3}(t)$ appears to follow a somewhat regular sinusoidal form, the PSD unveils a more complex distribution of oscillatory energy. In Section 5.11 or Eqn. (5.8), the amount of electrical power in a narrow gap about the 19 kHz breathing mode frequency worked out to about 68 W, while 88 W was observed at all frequencies above DC. Since the total thruster power measured about 420 W for this case, the electrical energy input to these oscillations is a non-negligible fraction. But this is not necessarily an efficiency loss since these oscillations may be improving the overall ionization efficiency through transient ionization rate bursts.

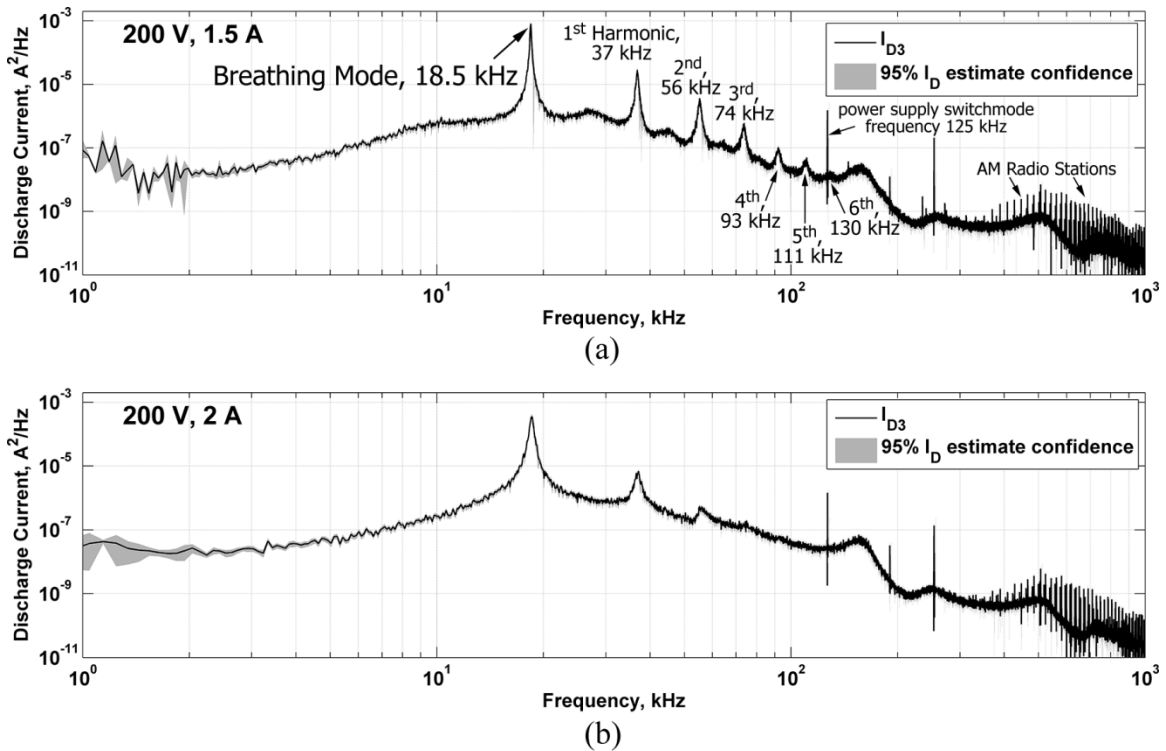


Figure 6.5. PSD of thruster discharge current for two thruster conditions: (a) 200 V 1.5 A and (a) 200 V 2 A discharge voltage and time-average discharge current. Both (a) and (b) use $Q = 100$ terms averaged.

In Figure 6.5, two different thruster operating-conditions are compared, and while the lower trace (b) appears identical to the data in Figure 6.4(b), it was acquired separately. The strong similarity is an indication that these spectral features (or turbulent statistics) are stationary. This was an important assumption required to enable the method of spatiotemporal data-fusion presented in Chapter 5, and the data in Figure 6.4(b) and Figure 6.5(b) help validate that unique method. The lower current 1.5 A 200 V thruster setting in Figure 6.5(a) appears very similar to the 2 A case (b) especially in the low-frequency bands from 1-10 kHz and from 150-1000 kHz. However, within these bands the peak breathing mode feature at $f_B = 18.5$ kHz is accompanied by a collection of 6 harmonics at the frequencies labeled from $2f_B = 37$ kHz to $7f_B = 130$ kHz. Half as many harmonics are visible in the 2 A case (b). The 1D breathing mode frequency estimation

in Eqn. (1.8) suggests that an increase in the velocity of the neutrals, U_n , (inside the discharge channel) should cause an increase in f_B that is proportional to $U_n^{1/2}$. The peak values corresponding to f_B in Figure 6.5(a) and (b) do indeed show a very slight increase from 18.5 kHz to 18.6 kHz between the 1.5 A and 2 A cases respectively—indicating the 33% increase in average discharge current appears primarily manifested in increased neutral density (not neutral velocity) within the discharge channel. For these data, the use of a 2 MHz raw rate of ADC sampling for $I_{D3}(t)$ in the collection of 2 million contiguous samples combined with the use of 100 averaged FFT terms, provides a PSD frequency resolution of $\Delta f_B = 100 \cdot (2\text{MHz}) / (2\text{MS}) = 100\text{Hz}$. This 100-Hz resolution along with the approximate 2-kHz width of the breathing mode peaks, bury the very fine the differences between the data in Figure 6.5. As an aside, the higher frequency content ($f > 400$ kHz) appears to contain AM radio broadcast signals given the discretized 10 kHz band gaps. This part of the spectrum is highly susceptible to EMI pickup, and since this pickup magnitude is too minute to affect thruster performance, no special care was employed to cancel out these signals (as was performed with the HDLP where these levels can become significant). The ability to measure these tiny signals in the noise-floor of the data is a direct result of having high-bandwidth high-SNR electronics and data collection hardware as well as employing the proper methods of spectral analysis (e.g. windowing and averaging very large sample-sets as outlined in Chapter 5).

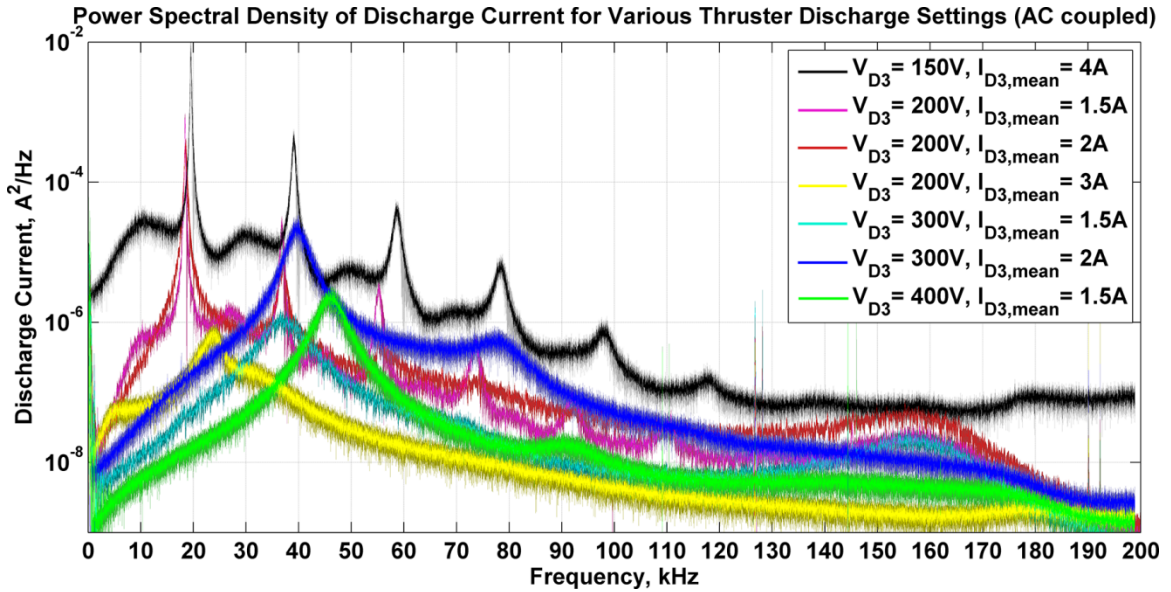


Figure 6.6. Discharge current spectra for various 150 V to 400 V thruster discharge voltage settings. The breathing mode peak frequency dominates each operating condition with harmonics visible in most traces. The shaded region behind each spectral trace is the 95% confidence interval of the power spectral density estimates shown (each estimate uses several million samples).

Zooming in on the frequency band DC-200 kHz and examining a wider assortment of thruster settings, Figure 6.6 portrays a more complex view of the spectral variability of the 600 W HET studied. One unique trace included in the PSD collection of Figure 6.6, is the 150-V 4-A case, where total (to date) thruster operation at this point is only around 30 minutes due to the far-from-nominal discharge current (at twice the cathode designed current). The other cases herein presented were run for up to an hour before data collection to ensure stationary statistical behavior. In fact, it is believed that the 150-V 4-A data are experiencing a so-called post-atmospheric "start transient," [103] in which water may be outgassing from the thruster, adding additional particles to the plasma that are known to alter thruster dynamics (producing strong discharge current oscillations) in the first 10's of minutes (for post-atmospheric exposure) thruster operation.

At the lower discharge voltages (150 V and 200 V), at least 5 harmonics of the breathing mode fundamental frequency are observed in frequencies up through 100 kHz, as was also seen in Figure 6.5. The presence of these harmonics is an indication that the fundamental breathing mode oscillations are not pure sinusoids, and in the time-domain these signals often possess steeper (than a sinusoid) edges and flatter peaks and/or troughs. However, neither the extreme transient fluctuations in Figure 6.3 or the more typical transients of Figure 6.4(a) are true sinusoids due to the relatively wide breathing mode frequency-space peaks (~ 2 kHz wide) and additional higher-frequency plasma dynamics appear to exist in the discharge current signal. Namely, the low-amplitude ripples in Figure 6.4(a) appear to correspond to a 160 kHz peak (visible in Figure 6.6 as the wide hump at the end of the 200-V 2-A and 1.5-A traces). These higher frequency modes are certainly of interest in the study of HET dynamics, but the focus of this work is to study the breathing mode oscillations that almost unanimously carry the largest magnitude plasma oscillations. In addition, the 100 kHz measurement rate of the HDLP diagnostic limits the measureable plasma dynamics to the band DC-50 kHz (as limited by the Nyquist frequency). Thus, these high frequency dynamics will require a faster version of the HDLP, and given the limits discussed in Chapter 4, a 1 MHz HDLP could feasibly quantify the HET plasma behavior of these higher frequency modes.

Another observation to make from these data is the general increase in the breathing mode frequency with the discharge voltage, with the 150 V 4 A case at 20 kHz to the 400 V 1.5 A case at 47 kHz. Similarly, for fixed voltages, consistent, but small, increases are observed with increased mean discharge current. The trends tend to encourage the applicability of the simple breathing mode model presented in Section 1.6.

[23] An attempt to fit Eqn. (1.8) to the data in Figure 6.6 is shown next in Figure 6.7. One drawback of this simple model is the constant form of the ionization zone length, L_i . One possible approach is to use the length of the acceleration zone, L_a , instead. But the lengths and locations of these zones, $L_{a,i}$, are not the same at all thruster settings [109] and depend quite strongly on the magnetic field structure. The thruster operating conditions used in Figure 6.6 were optimized in terms of thruster performance (see Appendix A). This optimization led to the selection of differing magnetic field settings for each of the different discharge voltage data in Figure 6.6. An estimation of the acceleration length scaling is presented in Eqn. (6.1): [3]

$$L_a \approx \frac{3U_n}{n_e \langle \sigma_i U_e \rangle}. \quad (6.1)$$

This expression includes the propellant ionization cross-section, σ_i , and results from using the continuity equation to solve for a length that contains 95% of the neutrals ionized. Since the thermal electron velocities, U_e , increase as T_e tends to increase with discharge voltage (using the empirical heuristic $T_e \approx \frac{1}{10} V_D$ [3]), Eqn. (6.1) indicates a proportional decrease in the length of the acceleration zone. Including this estimate of the acceleration zone length with the 1D breathing mode model in Section 1.6 should improve the accuracy of the estimate:

$$f_B \approx \frac{1}{3} n_e \langle \sigma_i U_e \rangle \sqrt{\frac{U_i}{U_n}} \quad (6.2)$$

This relationship is used as the "Theoretical Estimate" in Figure 6.7(a) where the measured discharge current breathing mode oscillation frequencies are also plotted.

Agreement is actually fairly decent for the constant cross-section and thermal (400K) neutral velocity inputs used.

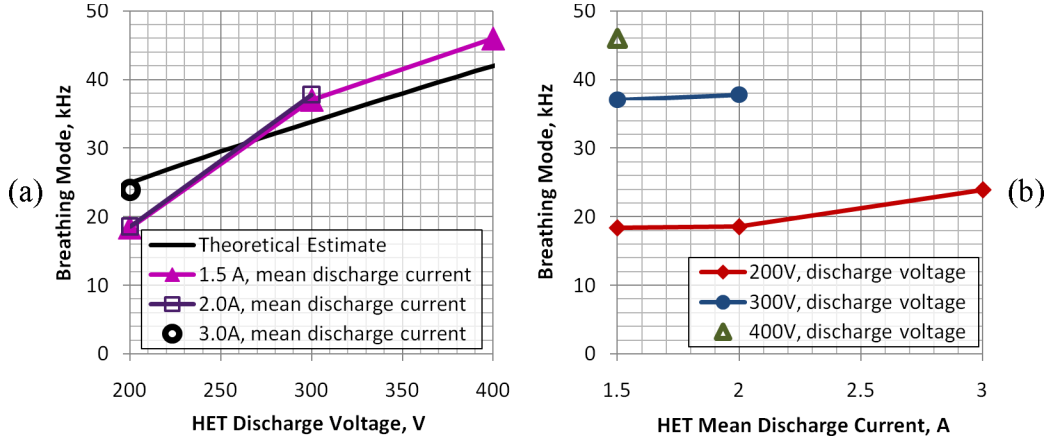


Figure 6.7. Breathing mode frequency variation with discharge voltage and mean discharge current operation of a 600-W Hall thruster. While both V_D and I_D effect the frequency of the thruster breathing mode, the discharge voltage plays a stronger role. Theoretical estimate from Eqn. (6.2)

The breathing mode trends in Figure 6.7(b) show very small variation changes in the thruster discharge current for a give voltage level. From Eqn. (6.2), a constant discharge voltage suggests that f_B scales with $n_e/U_n^{1/2}$, which then appears in the present data to be a slowly increasing function of the discharge current.

6.4 Single-point Plasma Property Fluctuations

While useful and easy to measure, the thruster discharge current signal is not providing a measurement of how the plasma properties of electron density, electron temperature, and plasma potential are fluctuating within the thruster plume. The HDLP diagnostic (discussed in Chapter 3) allows one to probe these properties throughout time and space. To begin this analysis, a time-series of plasma properties 10 cm downstream (near-field) from the 600-W HET are examined (Figure 6.8).

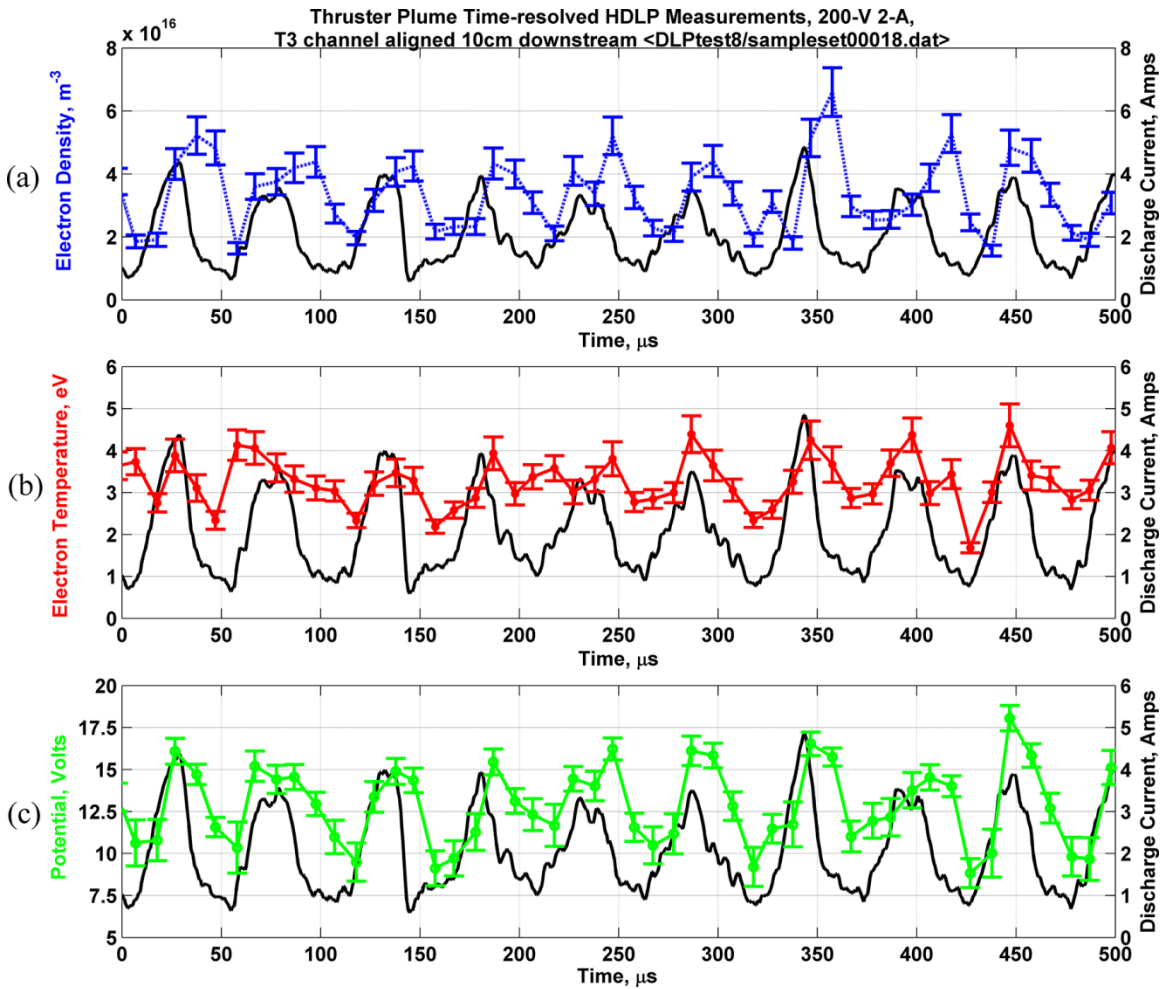


Figure 6.8. Time-resolved near-field HET fluctuation measurements using the HDLP: (a) $n_e(t)$, (b) $T_e(t)$, and (c) $I_d(t)$ (with included uncertainties).

All signals are sampled simultaneously, for $n_e(t)$, $T_e(t)$, and $V_p(t)$, are all determined from fully swept I-V traces acquired in brief 10 μs intervals. An additional ADC sampling of the thruster discharge current is also included with each time-resolved property to help accentuate similarities and differences in the oscillatory waveforms. At this near-field location the short ion transit time, 12.4 μs here, (see next Subsection 6.4.1 for example calculation) is about the same as the HDLP rate of plasma property collection at 10 μs . Accordingly, only very slight phase lags (if any) appear in these data. In Figure 6.8, the device uncertainties are included using the HDLP error analysis in

Section 3.8. All of the observed near-field plasma properties exhibit fluctuations well in excess of the diagnostic uncertainties, and with clear correlation of the thruster discharge current signal. In the next section, a variety of different thruster settings are explored in the same manner, and this important finding—that the discharge current correlates almost linearly to the measured plasma properties—will again be seen, thereby placing greater value in the easily measured discharge current signal.

6.4.1 Ion Transit Delay

The delay between initial spikes in discharge current $I_D(t)$ and corresponding fluctuations in the electron density $n_e(t)$ (as in Figure 6.8) quite accurately matches the expected ion transit times for Xe⁺ ions originating from the thruster discharge channel. Generally, the bulk (>95%) of the ion acceleration occurs within two thruster diameters of a HET (mean channel or diameter here is approximately 5 cm). As the precise length of the acceleration zone is unknown for this thruster, an estimate of the theoretical transit time, $\tau_{i,t}$, is made as the integrated time to accelerate (in the axial direction, x , with $x = 0$ at the thruster exit-plane) to the expected propellant ion velocity, U_i (based on discharge potential, V_D), in two thruster diameters plus the time at this speed to reach the point of interest:

$$\tau_{i,t}(x) = \frac{m_i U_i L_a}{e \eta_V V_D} + \frac{x - L_a}{U_i} = \frac{x + L_a}{U_i}, \quad x \geq L_a, \quad (6.3)$$

and, $\frac{1}{2} m_i U_i^2 = e \eta_V V_D \rightarrow U_i = \sqrt{2e \eta_V V_D / m_i}$

A constant electric field is assumed throughout the acceleration zone ($L_a = 10$ cm) with a voltage utilization efficiency (η_V) of 80% (for singly-charged xenon ions with mass m_i and charge e). While the selected length of the acceleration zone is much larger

than is typically measured, it is the one value that works with a variety of data at different positions and thruster operating settings. The simplicity of the theory applied in Eqn. (6.3), does not allow for accounting of the many effects observed in real thrusters, but with $L_a = 2D_{HET}$, the match to the presented data is consistent. Thus at 10 cm downstream (as in Figure 6.8) we find $\tau_{i,t}(10 \text{ cm}) = 13.1 \mu\text{s}$.

By looking at the phase, ϕ_d , between the discretely transformed Fourier coefficients (using Eqn. (5.4)) of the discharge current and electron density at the breathing mode frequency, f_B , one may compute an accurate (most statistically probable) value of this delay, τ_d , using Eqn. (6.4).

$$\tau_d(x) = \frac{\phi_d(x)}{2\pi \cdot f_B} \tag{6.4}$$

$$\tau_d(10 \text{ cm}) = \frac{90.6^\circ \pm 4^\circ}{360^\circ \cdot 18.65 \text{ kHz}} = 13.4 \pm 0.6 \mu\text{s}$$

The "uncertainty" in this phase measurement is taken as the 95% confidence interval for a narrow 100-Hz wide band about f_B . Since this phase measurement is taken as the effective average phase between about 19,000 breathing mode peaks in $I_D(t)$ and $n_e(t)$, the "uncertainty" here is an indirect measure of the turbulence level that causes some ion bursts to travel faster (-) or slower (+) than the most probable travel time. A proper estimate of measurement uncertainty is taken as the measurement resolution divided by the square-root of the number of samples: $10 \mu\text{s} / \sqrt{19,000} = \pm 0.07 \mu\text{s}$. For this case at 10 cm downstream, the simple 1D theory and phase measurement agree within 0.2%. For the entire axial profile ($x = 10$ to 60 cm) aligned with the radial center ($r \approx 3$ cm) of the accelerating discharge channel, Figure 6.9 is constructed by dividing x by each

Eqn. (6.3) and (6.4) resulting in an average difference of 2.3%. The large turbulent uncertainty in phase apparent at 0.3 m downstream is likely caused by the initially toroidially shaped (inside the annular discharge channel) breathing mode ion wave achieving thermally expanded closure. Using the inner HET channel diameter (≈ 4 cm), Eqn. (6.3) for average transit velocity ($\bar{U}_{i,t} = x/\tau_{i,t}$), and an average electron temperature of 2.9 eV closure (upon the channel-aligned x-axis in Figure 6.9) should occur near:

$$\begin{aligned}
 x_{closure} &\approx D_{inner,HET} \cdot \bar{U}_{i,t} / U_{Bohm} \\
 &\approx D_{inner,HET} \cdot \sqrt{2\eta_V V_D / T_e} - L_a = 0.32 \text{ m}
 \end{aligned}
 \tag{6.5}$$

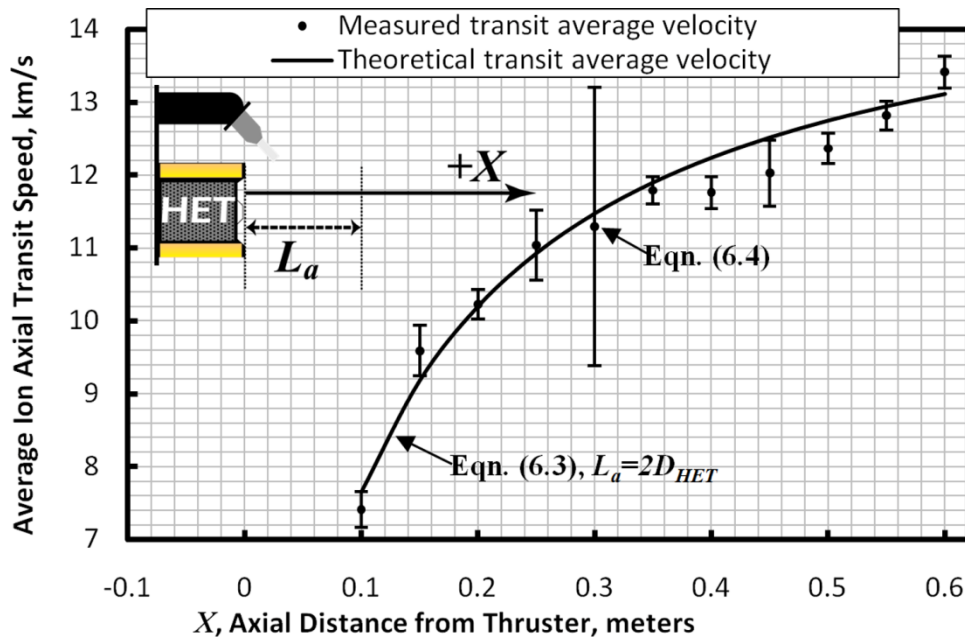


Figure 6.9. Average axial ion transit speeds, measured versus (1D) theoretically expected values. The "error"-bars included span the 95% confidence intervals of the phase measurements and thereby indicate the level of turbulent uncertainty in phase at each location. Data from 200 V 2 A thruster setting

Another different explanation of this "closure" event is to notice that the near-field plume directly in front of the thruster (on the thruster discharge channel axis of symmetry) is relatively hollow, containing lower-density plasma than exists directly

downstream from the radial center of the discharge channel. Next, the finite plume divergence (e.g. an exhaust cone of 20°) angle will achieve closure (or crossover) at some downstream location. Finally, the plasma interactions at the time of "closure" could involve an ion-ion two-stream instability [110] or an ion-acoustic shock since the radial ion-acoustic Mach number of plasma inside the ion wave can reside in the $1 < M_{i,radial} < 1.6$ range requisite for shock formation. [87]

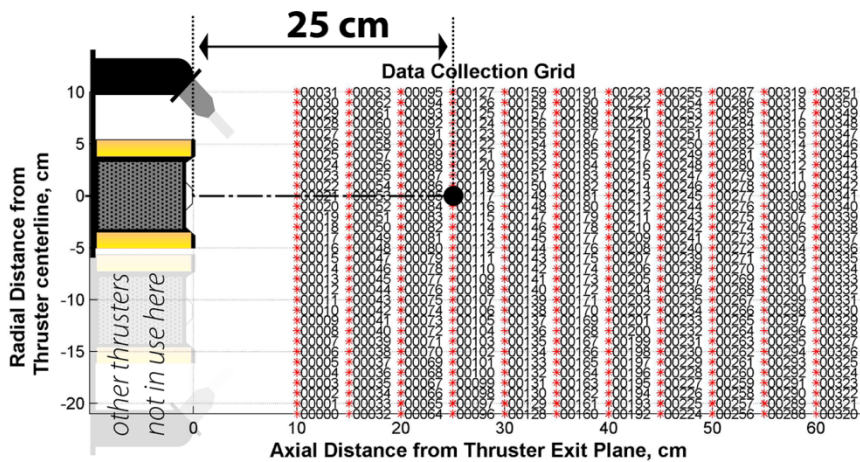


Figure 6.10. Position of HDLP data collection for Sections 6.4.2 and 6.5.1.

6.4.2 Variations with Thruster Settings

Next, the temporal nature of the plasma is investigated at fixed position of 25 cm downstream (illustrated in Figure 6.10) for three different discharge voltages 200 V, 300 V, and 400 V, and two different mean discharge current discharge currents (1.5 A and 2 A). [111]

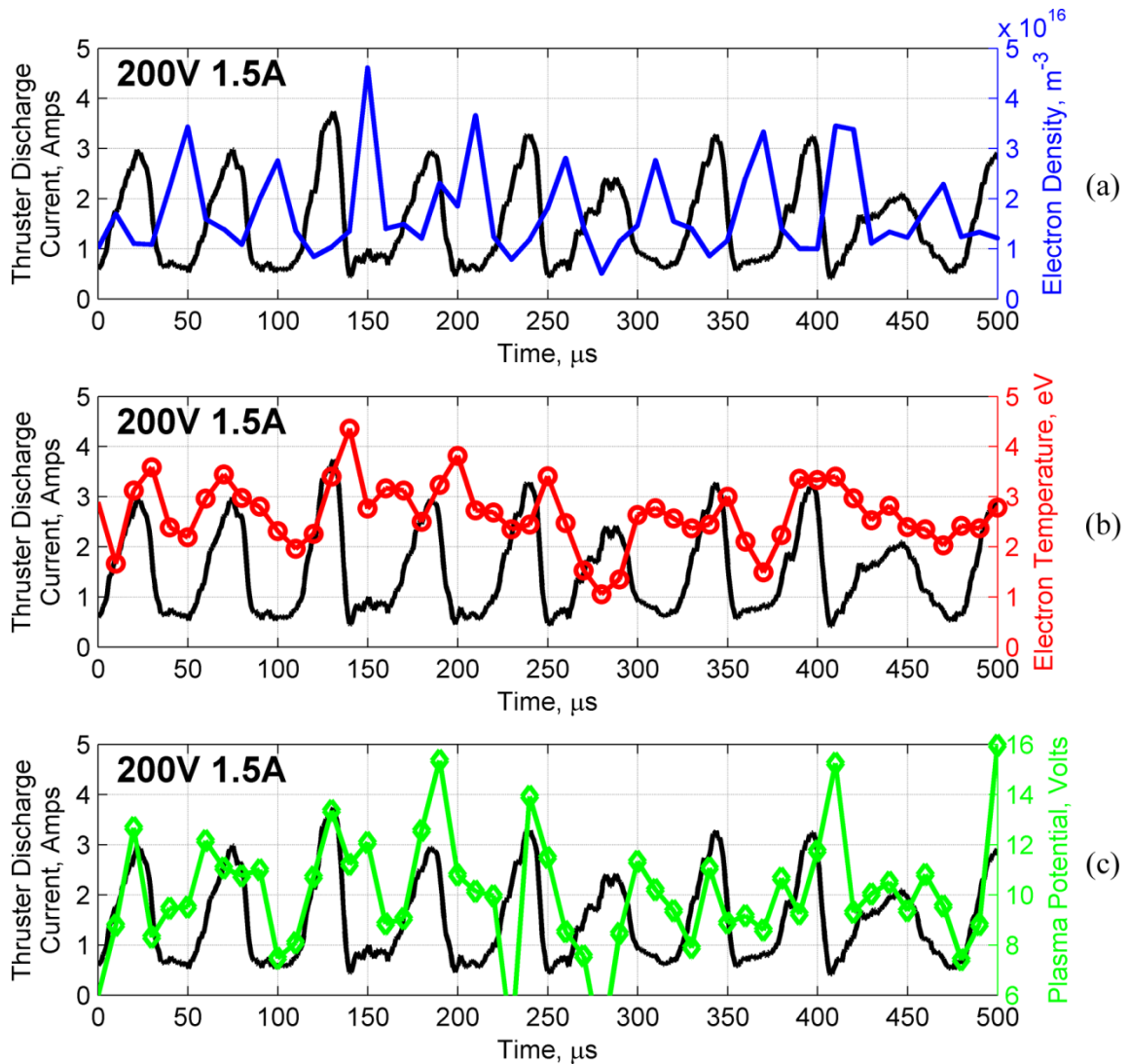


Figure 6.11. HDLP time-resolved plasma properties for a 200-V 1.5-A discharge measured 25 cm downstream from HET exit plane (aligned on thruster centerline).

At this distance of 0.25 m downstream from the thruster, very noticeable ion transit time delays are visible between discharge current fluctuations (in black) and electron density fluctuations (in blue) for Figure 6.11(a). The measurement of these delays in time-domain traces (as in Figure 6.11) is not a very practical method, especially with the 10- μ s discretization of the HDLP plasma measurements. In frequency-space however, these transit-time delay measurements can be attained with relative ease and excellent accuracy as demonstrated in Eqn. (6.4).

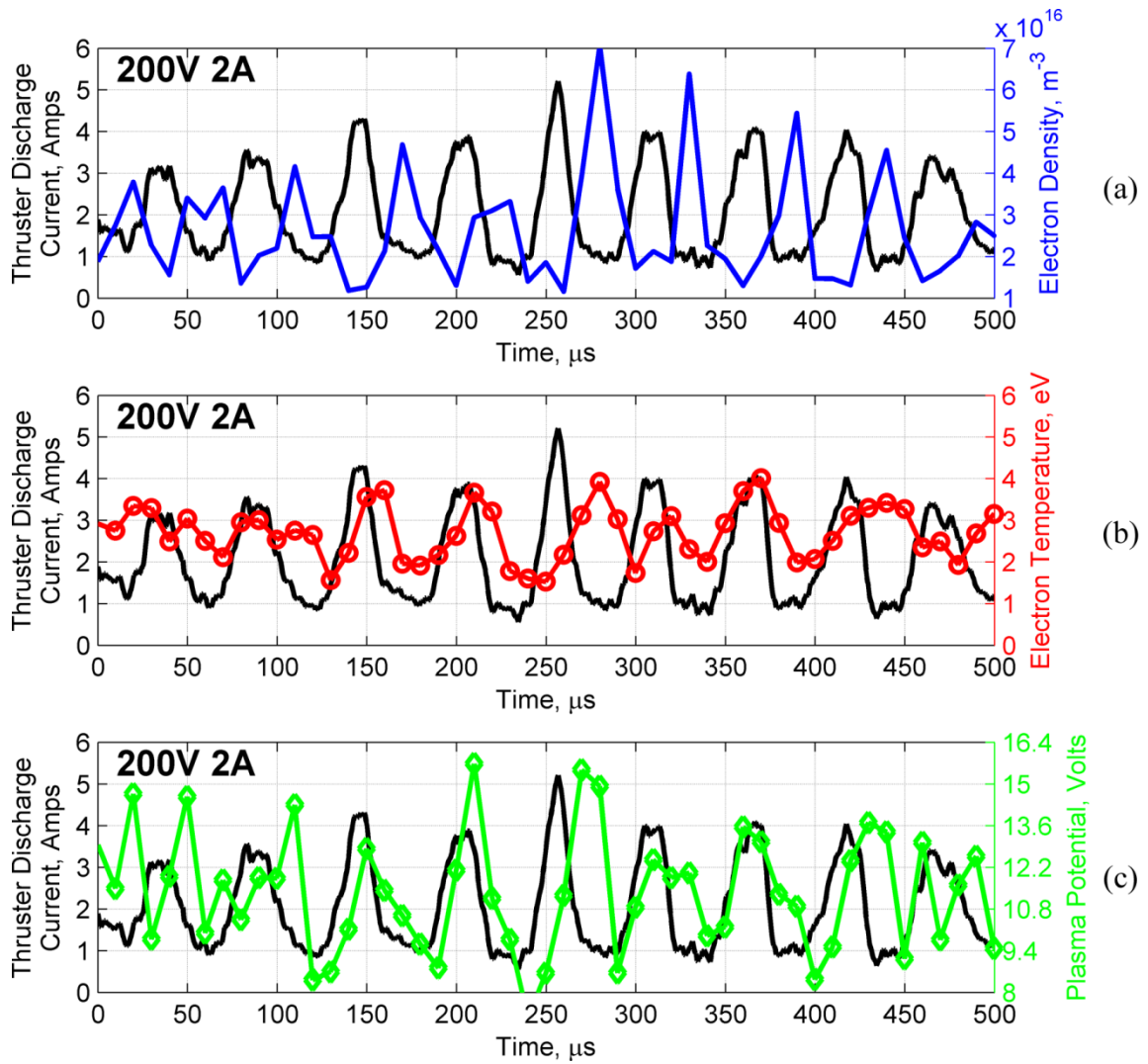


Figure 6.12. HDLP time-resolved plasma properties for a 200-V 2-A discharge measured 25 cm downstream from HET exit plane (aligned on thruster centerline).

Following the present series of time-resolved data, a collection of the delays computed from these data, using Eqn. (6.4) is shown in Figure 6.16. The 33% higher current 200 V discharge data in Figure 6.12 show temporal fluctuations very analogous to the previous Figure 6.11. Perhaps the only difference is the increase in the electron density where an approximate 33% increase in the average levels is observed. While error bars are not included for this series (Figure 6.11 through Figure 6.15) of data, the uncertainty is $\pm 10\text{-}20\%$ for n_e and T_e and $\pm 10\text{-}40\%$ for V_p as seen in Figure 6.8.

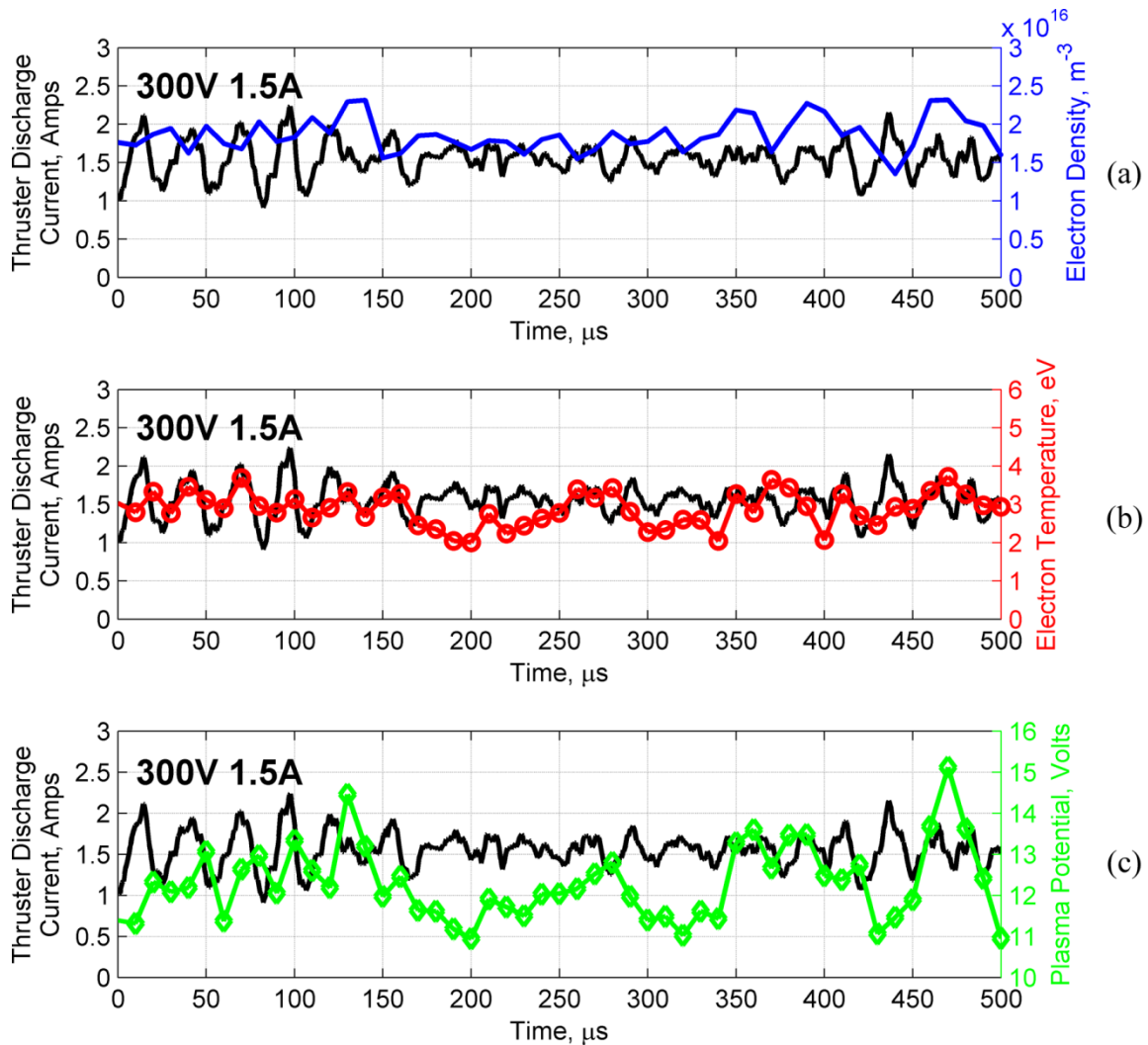


Figure 6.13. HDLP time-resolved plasma properties for a 300-V 1.5-A discharge measured 25 cm downstream from HET exit plane (aligned on thruster centerline).

The next cases in Figure 6.13 (for 1.5 A time-averaged discharge current) and Figure 6.14 (2 A) examine the 300 V discharge voltage setting. Unfortunately, the growth of the HET breathing mode frequencies here to 37 kHz (300 V 1.5 A) and 40 kHz (300 V 2 A) move close to the HDLP Nyquist frequency (50 kHz) and thus the captured plasma fluctuations are less defined having only two or three points per breathing mode cycle. However, by comparing these data to the instantaneous discharge current waveform included in each trace, the 300 V 1.5 A discharge simply is not breathing in a regular

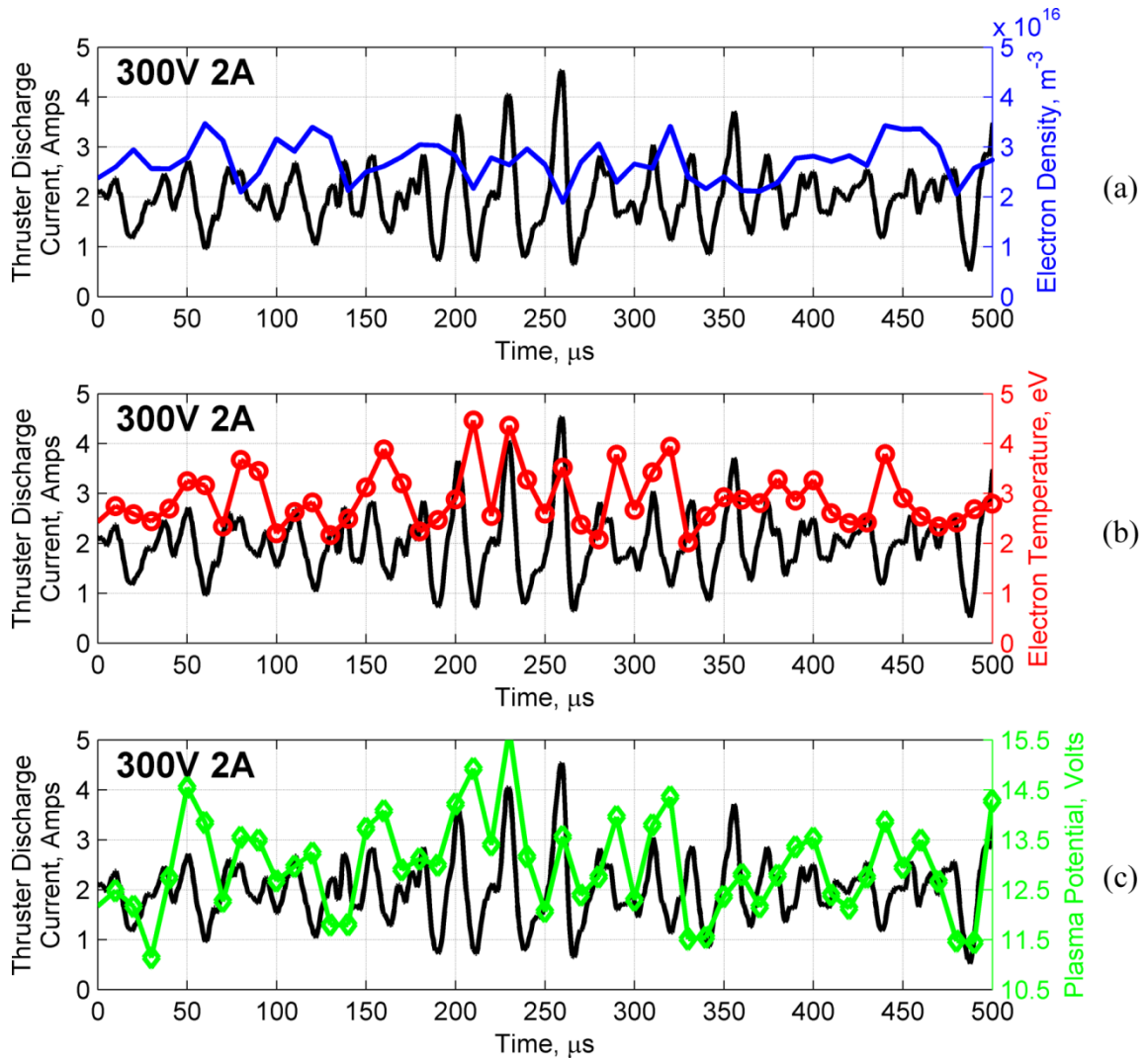


Figure 6.14. HDLP time-resolved plasma properties for a 300-V 2-A discharge measured 25 cm downstream from HET exit plane (aligned on thruster centerline).

manner. When the fluctuations in $I_D(t)$ in the temporal gap from about 175 μs to 250 μs are relatively quiescent (peak-to-peak amplitudes ≈ 500 mA), the fluctuations in $T_e(t)$ (Figure 6.13(b)) and $V_p(t)$ (Figure 6.13(c)) almost vanish. It is not known why the magnitudes of the fluctuations for the 300 V 1.5 A setting are reduced but this is also quite apparent in the PSD magnitude for this setting (see Figure 6.6). Comparing with the 300 V 2 A case in Figure 6.14, there exists a fluctuation magnitude difference (peak-to-peak Amperes over peak-to-peak Amperes) of about 4-5. In the PSD data the f_B

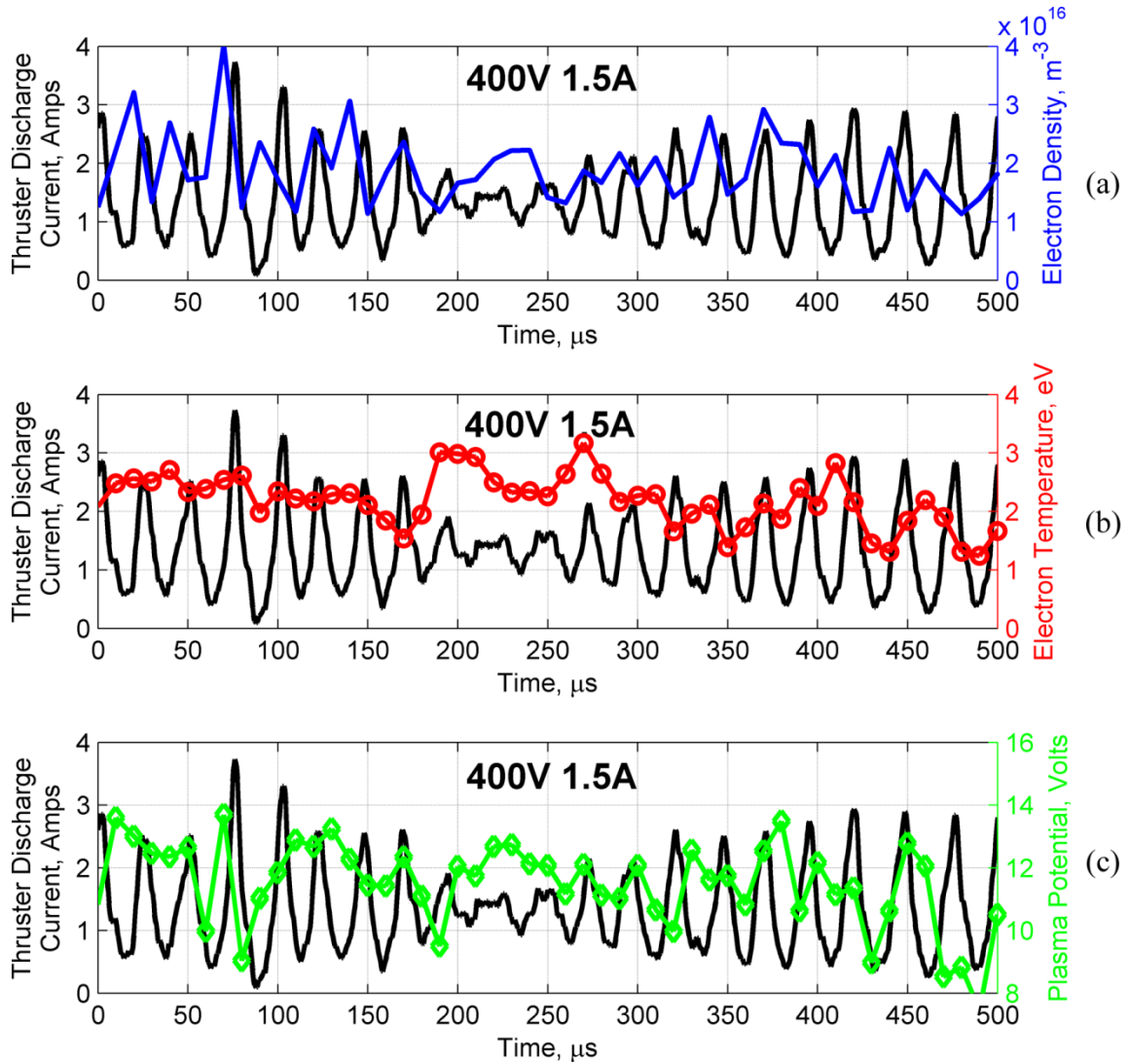


Figure 6.15. HDLP time-resolved plasma properties for a 400-V 1.5-A discharge measured 25 cm downstream from HET exit plane (aligned on thruster centerline).

peaks are different by a factor (A^2/A^2) of 20. The very broad structure of the 300 V PSD breathing mode peaks indicates that the oscillations are not strongly localized to the aforementioned breathing mode frequencies, and indeed measurements of the full-width and half-maximum yield $\Delta f_{FWHM}|_{300V,1.5A} = 8 \text{ kHz}$ and $\Delta f_{FWHM}|_{300V,2A} = 5 \text{ kHz}$. These broader spectral forms of the breathing mode at 300 V imply that the breathing mode oscillations are less like the fixed frequency harmonic oscillators than the 200 V data exhibits. One additional problematic feature of data fluctuating near the Nyquist

frequency is the effect that these oscillations can have on the rapidly acquired I-V Langmuir probe characteristics. If the plasma state is changing significantly during the acquisition of an I-V trace then the resulting interpretation of the data will be affected and this may play a role in the noisier appearance of the $T_e(t)$ and $V_p(t)$ data for 300 V and 400 V HET settings. Using a faster HDLP would avoid this issue and it is recommended here that for the HDLP diagnostic, the sample rate should exceed the highest expected (large amplitude) plasma oscillation by a factor of five (as exists for the 200 V data).

The final 400 V discharge voltage set of single-point plasma temporal data in Figure 6.15 should be oscillating really close to the HDLP Nyquist frequency with a breathing mode centered at 46 kHz according to Figure 6.6. But after examining the PSD trace from this data, a lower-frequency breathing mode was discovered (39 kHz); and this resulted from the use of off-nominal electromagnetic settings. Interestingly, these utilized settings are the same as the nominal settings used for the 300 V conditions, and the resultant breathing mode frequency of the data in Figure 6.15 of 39 kHz is a value quite close to the 300 V breathing modes (37 kHz and 40 kHz for 300 V 1.5 A and 2.0 A cases respectively). Even so, well correlated oscillations in $I_D(t)$ and $n_e(t)$ are seen with a delay of 14.5 μs ($\pm 4.7 \mu\text{s}$). Comparing this delay to the ion transit delay seen at 200 V and 1.5 A, where the delay measures 24.1 μs ($\pm 1.5 \mu\text{s}$) a fractional difference of 1.67 is observed. It might be expected that the difference would more closely match the factor of 2 difference in discharge voltages, but this factor neglects changes in the thruster discharge efficiencies and in the length of the acceleration zone.

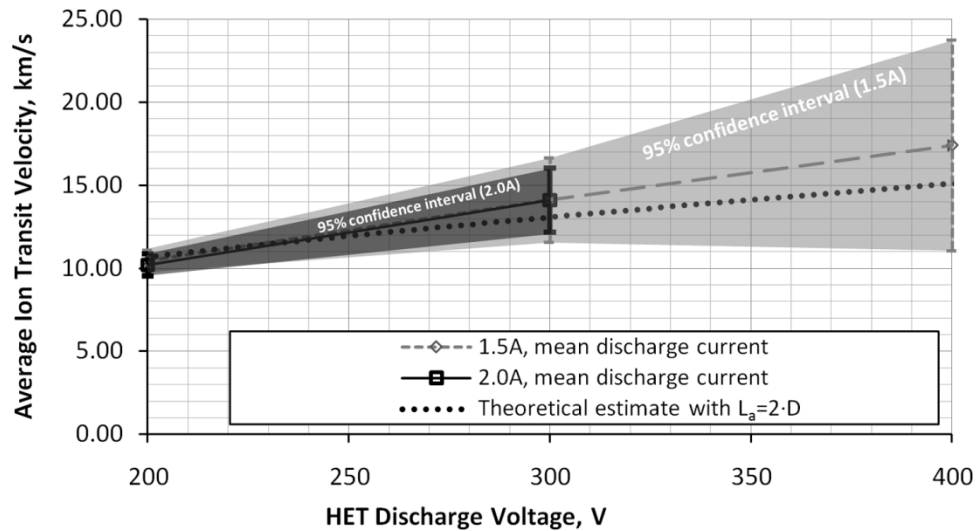


Figure 6.16. Average ion transit velocity for 200-400V operation with 1.5-A and 2.0-A HET discharge. The linearly expanded confidence intervals contain 95% of the collected transit delay measurements suggesting either more experimental-error or more chaotic breathing mode fluctuations.

By dividing the 0.25 m position of the HDLP measurements by the measured ion-transit delays for the data in Figure 6.11 through Figure 6.15, the average ion transit velocity is presented in Figure 6.16. In this figure, the 95% confidence intervals for the measurement of phase (see Section 6.4.1) are included to show an interesting ballooning effect in the turbulent uncertainty of the measurement. While it seemed safe to attribute these "error-bars" as turbulent uncertainty due to different types of fluctuations observed for the low-voltage (200 V) thruster settings, the high-voltage cases possess a breathing mode peak frequency centered near the Nyquist frequency of the HDLP. It seems probable that this could disrupt the accuracy of the delay measurements, and in this way contribute to measurement uncertainty (and not provide an indication of the turbulence level). Another possible explanation for the ballooning effect in Figure 6.16 uncertainty is that the "closure" point estimated by Eqn. (6.5), is moving closer to the thruster and the position of the HDLP for these data. An estimation of $x_{closure}$ for the 300 V and 400 V

data suggests the same 0.3 m closure distance, but the accuracy of this estimation is not too high due to the simplifications involved in its definition.

A tabulation of statistics from the time-resolved plume plasma properties for the cases in Figure 6.11 through Figure 6.15 is given in Table 6.1. The "~" properties are the standard deviation of the full sets of time-resolved HDLP data obtained at this location (see Figure 6.10). Similarly the "-" properties are the time-averaged values from the full sets of time-resolved HDLP data at 25 cm. As these data are each averaged from 100,000-4,000,000 time-resolved measurements, their statistical accuracy is significant.

Table 6.1. Tabulation of time-averaged and fluctuation standard deviation plasma properties 25 cm downstream (on thruster centerline) of a 600-W HET.

V_D [V]	\bar{I}_D [A]	\tilde{I}_D [A]	\bar{n}_e [m^{-3}]	\tilde{n}_e [m^{-3}]	\bar{T}_e [eV]	\tilde{T}_e [eV]	\bar{V}_p [V]	\tilde{V}_p [V]
200	1.55	0.89	1.7E+16	9.4E+15	2.61	0.60	9.8	2.5
200	2.10	0.97	2.4E+16	9.7E+15	2.71	0.56	11.2	1.9
300	1.52	0.24	1.9E+16	3.6E+15	2.94	0.54	12.4	1.3
300	2.02	0.68	2.7E+16	6.2E+15	2.94	0.61	12.9	1.4
400	1.53	0.77	1.9E+16	6.9E+15	2.11	0.48	11.5	2.0

Examination of the trends in terms of the fluctuation standard deviation over mean values brings about the following intriguing result:

$$\left(\frac{1}{2} \frac{\tilde{I}_D}{\bar{I}_D} \approx \frac{1}{2} \frac{\tilde{n}_e}{\bar{n}_e} \approx \frac{\tilde{T}_e}{\bar{T}_e} \approx \frac{\tilde{V}_p}{\bar{V}_p} \right)_{25 \text{ cm, HET at } 200\text{-}400 \text{ V, } 1.5\text{-}2 \text{ A}} \quad (6.6)$$

This result directly relates easily measured discharge current fluctuations to corresponding (and more difficult to measure) plume plasma property fluctuations. Only a single plume position is considered in Table 6.1, but somewhat similar ratios are observed at most plume locations measured in this study. Specifically, for the 200 V 2 A

thruster setting, the relationship in Eqn. (6.7) is observed by averaging over the entire plume (the average difference in this value is also shown).

$$\left. \frac{\tilde{I}_D}{I_D} \right|_{200 \text{ V } 2 \text{ A}} \approx \left\langle \frac{\tilde{n}_e}{\bar{n}_e}, \frac{\tilde{T}_e}{\bar{T}_e}, \frac{\tilde{V}_p}{\bar{V}_p} \right\rangle_{31 \text{ by } 50 \text{ cm HET plume}} \approx 53.3\% \pm 9.8\% \quad (6.7)$$

Comparing to Eqn. (6.6), the only difference is that the temperature and potential fluctuation standard deviation over mean ratios increase to roughly match the discharge current and electron density ratios. However, the far-field uncertainties in electron temperature and plasma potential are increased (seen during the analysis in Section 3.8) and therefore these data may be increasing the standard deviation in Eqn. (6.7) due to diagnostic uncertainty and not due to turbulent breathing mode fluctuations.

6.5 Electron Temperature and Plasma Potential Fluctuations

Comparing the instantaneous measurements of thruster discharge current, electron temperature, and plasma potential, a near zero phase difference in the breathing mode oscillations is seen, in general, for the proceeding figures. For the electron temperature, one might expect the delay to be set by the electron thermal motion—and for 3 eV bulk electrons travelling at around one million meters per second, this delay ($\approx 0.25 \mu\text{s}$, at 25 cm) is well under the $10 \mu\text{s}$ temporal resolution of the HDLP system. Since the HET discharge circuit closes between the inner discharge channel anode and externally mounted cathode, the burst of ions generated with each breathing mode cycle produces an equivalent burst of electrons from the cathode. This in-rush demand for more electron current from the cathode may be met in part by increased electron heating inside the cathode (as well as inside the ionizing closed-drift Hall current) thereby generating the

peaks in $T_e(t)$ (seen in Figure 6.11 through Figure 6.15) that occur nearly simultaneously with $I_D(t)$ peaks.

With each ionization burst, a rapid buildup of plasma density in a narrow localized region (with axial width on the order of ion-acoustic speed multiplied by the time from burst beginning or $U_{Bohm}t_b$) produces a pressure gradient pushing the more mobile (nonmagnetized in the plume) electrons outward into the surrounding space, a process that leads to a rapidly (again at electron thermal velocity) lowered plasma potential at distances downstream. But, it is not quite this simple because these electrons represent a hotter population and, if their thermal-pressure overcomes the density-pressure, the plasma potential downstream of the ion burst would then increase to balance out the pressure with an electric field. From the data in Figure 6.11 through Figure 6.15, it seems that both effects may be occurring since not all the peaks in both $I_D(t)$ and $V_p(t)$ line up.

Another complicating effect that occurs once the density wave reaches a given downstream location is the convected properties of the plasma therein contained. It seems likely that the electrons carried by the wave may be cooler since the hotter ones are the first to react to the density pressure losses, and this in combination with the potential set up to balance the density gradient pressure force, leads to a higher plasma potential inside the traveling density wave. Altogether, the electron physics here is not captured with the simple Boltzmann relation and a more complete description demanding perhaps an alternate form of the time-dependent (non-linearized) Boltzmann equation is needed to understand the constantly shifting nature of electron equilibrium within this fluctuating plasma plume.

6.5.1 Plasma Fluctuations in Frequency Space

In this section, the same 200 V 1.5 A and 2 A data in the preceding section is examined, but here signals are transformed into the frequency domain. Again, the fixed position 25 cm downstream and on HET centerline (Figure 6.10) is the location of the HDLP used to make these measurements.

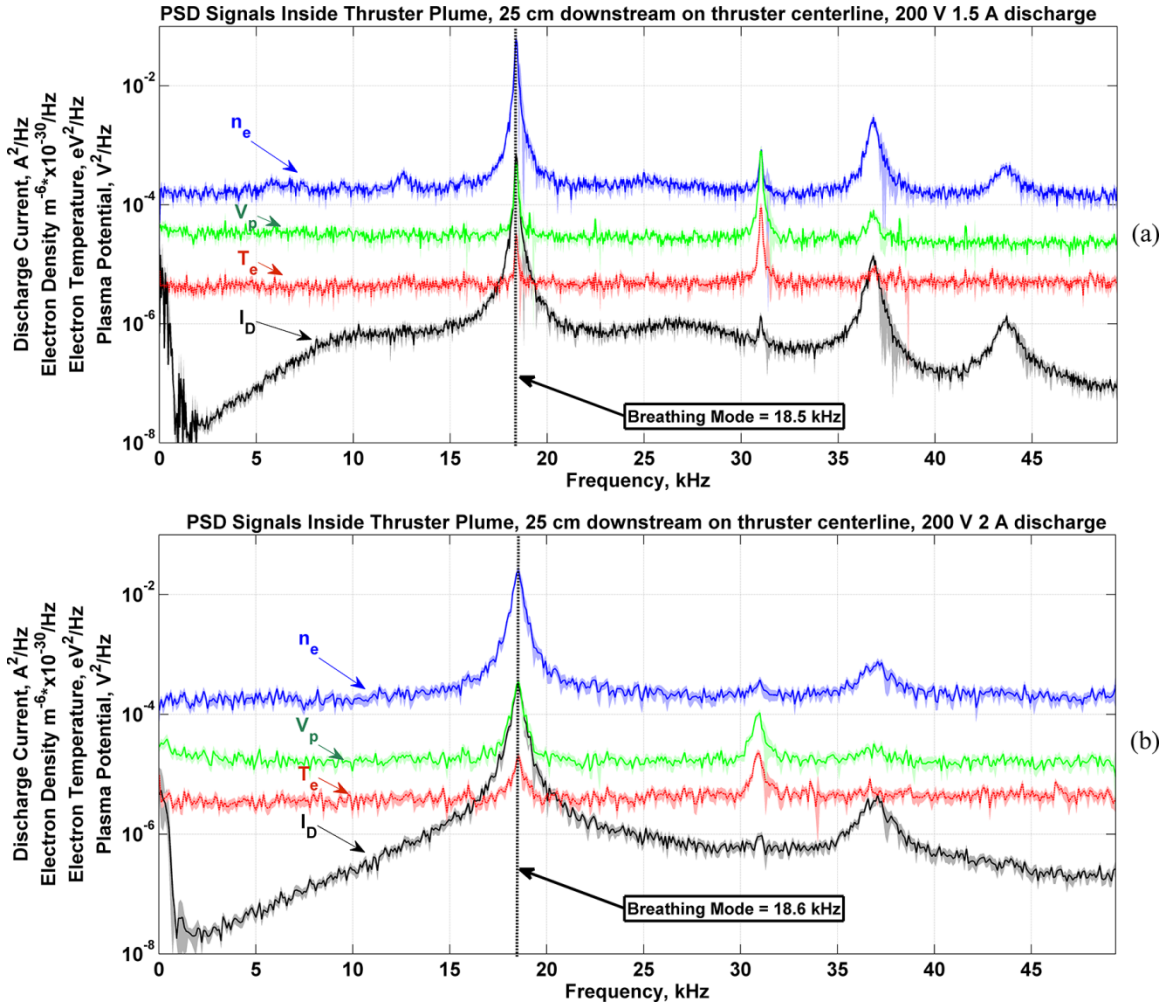


Figure 6.17. Power spectral densities of plasma properties 25 cm downstream from HET for (a) 200 V 1.5 A and (b) 200 V 2 A discharge settings.

In Figure 6.17, the PSD traces for discharge current (in black) and electron density (in blue) are very similar to one another. Each case features a central dominant breathing mode peak centered about 18.5 kHz (a) or 18.6 kHz (b) and one slightly weaker harmonic

of this fundamental centered near 37 kHz. The 200 V 1.5 A case in Figure 6.17(a) also contains an additional peak near 44 kHz that is not a harmonic of the breathing mode, and is of unknown origin. The narrow peak at 31 kHz while present for both discharge current cases is also of uncertain origin, but exists for all spectral signals in Figure 6.17.

6.6 Space and Time Resolved Thruster Plume

Next presented are results from an exploration of the time-resolved plasma throughout the two-dimensional (2D) plume region interrogated. These results will focus on electron density measurements, but similar trends are also observed for the other plasma properties of electron temperature and plasma potential as was seen in the preceding single-point data.

6.6.1 2D Maps of Time-averaged and Fluctuation Amplitude Electron Density

Figure 6.18 expands the result seen in Eqns. (6.6) and (6.7) to the entire two-dimensional plume by comparing planar maps of the mean electron density contours to the average peak-to-peak amplitude in electron density fluctuation contours (the average peak-to-peak amplitude is used to these maps keep on an identical color-scaling, but peak-to-peak amplitude is generally proportional to standard deviation; for sinusoidal waves the proportionality is just $2\sqrt{2}$). The similarity of all electron density contour maps (a), (b), (c), and (d), in Figure 6.18, is striking, yet since these data are all for the same mean value of 2-A discharge current, the time-averaged results are expected to be similar. The slight decrease in electron density average (peak-to-peak) fluctuation amplitude is manifested as a slight radial narrowing of the plume field. Shown later in Section 6.7.3, very similar results are seen when two Hall thrusters are operating at the same time in a clustered configuration. [112]

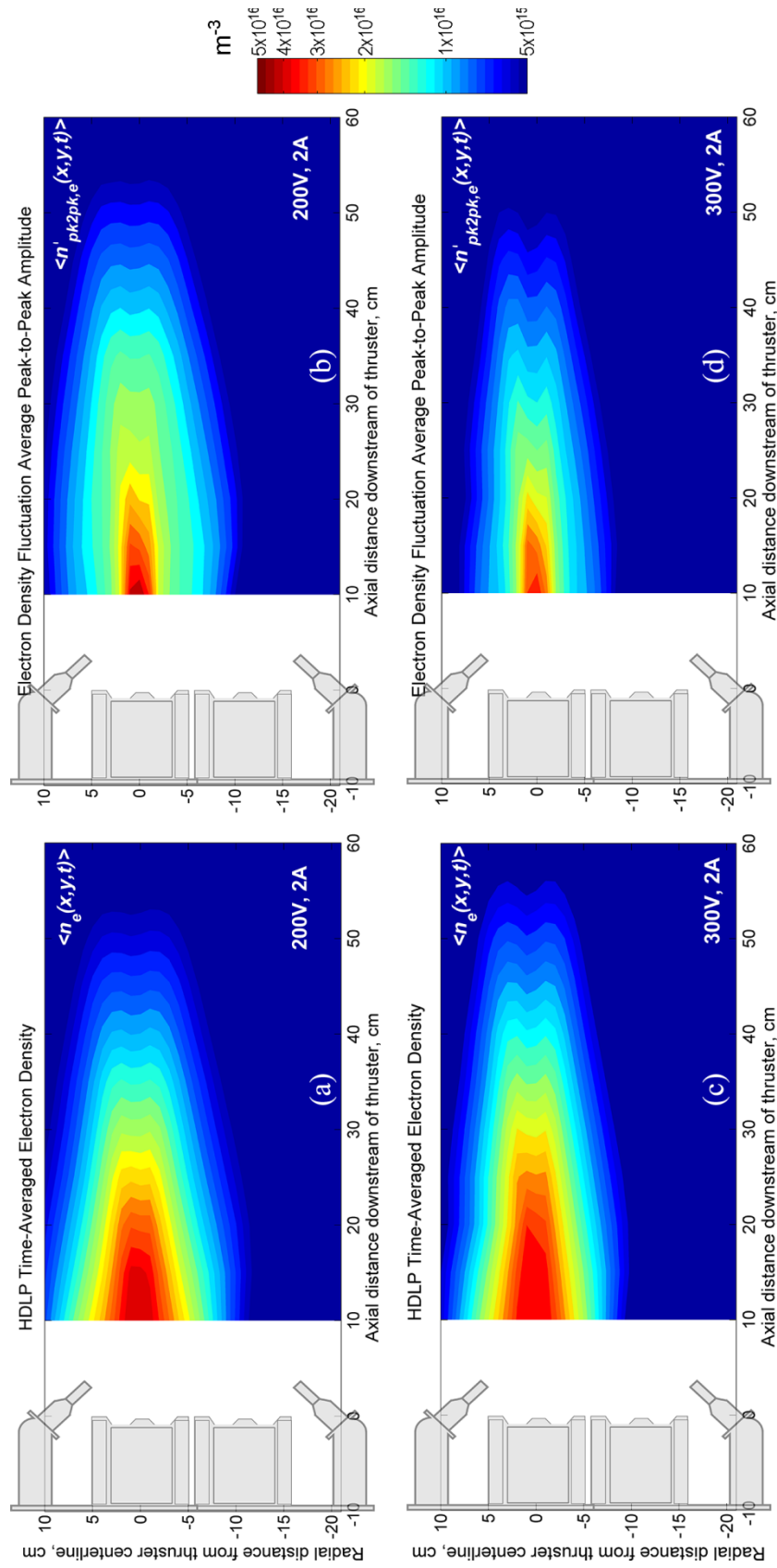


Figure 6.18. Collection of planar time-averaged electron density $\langle n_e(x,y,t) \rangle$ and fluctuation average peak-to-peak electron density amplitude $\langle n_{e,pk2pk}(x,y,t) \rangle$. These averaged planar fields are computed by using all 100,000 time-resolved (with HDLP) electron density measurements obtained at each of the 352 grid points.

6.6.2 Two-dimensional Time-resolved Thruster Plume

Finally, in Figure 6.19, a series of fully time-resolved planar density contour maps are presented for the 200-V 2-A and 300-V 2-A thruster discharge settings (for the 31-cm by 50-cm plume region as shown in prior figures). The method by which single-point HDLP time-resolved measurements are combined into two-dimensional time-resolved frames utilizes the unique spatiotemporal data fusion technique presented in Chapter 5. The left column (c) in Figure 6.19, includes six density frames, each separated by 10- μ s, thus portraying just about one complete breathing mode cycle (the 200-V breathing mode period is typically about 54 μ s). The right column (d) shows six equally spaced (by 10- μ s) density frames for the 300-V 2-A discharge case, but since the thruster completes over two full breathing mode cycles in the 50 μ s series and since 300-V oscillations are lower in magnitude, the plasma field density oscillations appear less distinct. To the side of each column are the corresponding sequences of simultaneous measured thruster discharge current oscillations with an "*" denoting the time-stamps for the planar frame series. The large amplitude discharge current oscillation visible in the 200-V case (from 1-A to 4.0-A back down to 0.5-A) is typical for this thruster setting, and this very clearly generates a corresponding burst of plasma density that is ejected from the thruster at a velocity exceeding 10 km/s (see Section 6.4.1 more ion-wave velocity results).

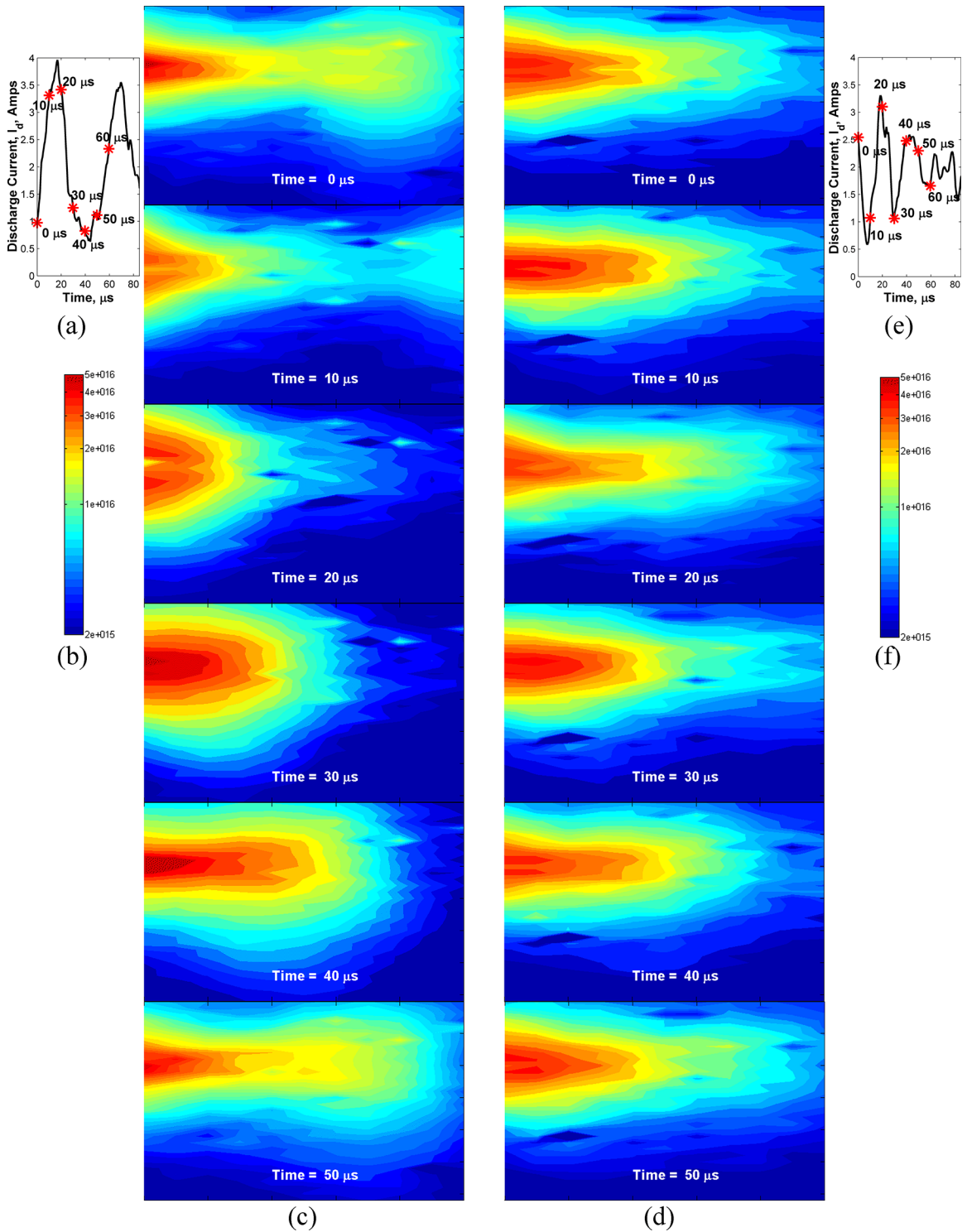


Figure 6.19. Series of time-resolved two-dimensional electron density contour maps for (a)-(c) 200 V 2 A and (d)-(f) 300 V 2 A HET discharge settings. The lower-frequency and slower-propagating breathing mode waves at 200V (18.6 kHz and 10-13 km/s) provide additional oscillation cycle detail with the 10- μ s frame-rate attained by the HDLP.

6.6.3 Traveling Ion Waves in the Plume

To examine the HET ion waves more clearly, a 3D data representation is provided in Figure 6.20. Identifying the radial density profile as having a narrow Gaussian shape, and adding the additional axis for time, a clear set of waves are seen to propagate past this axially fixed strip at a rate of 19 kHz—one wave for each “breath” of xenon the thruster draws.

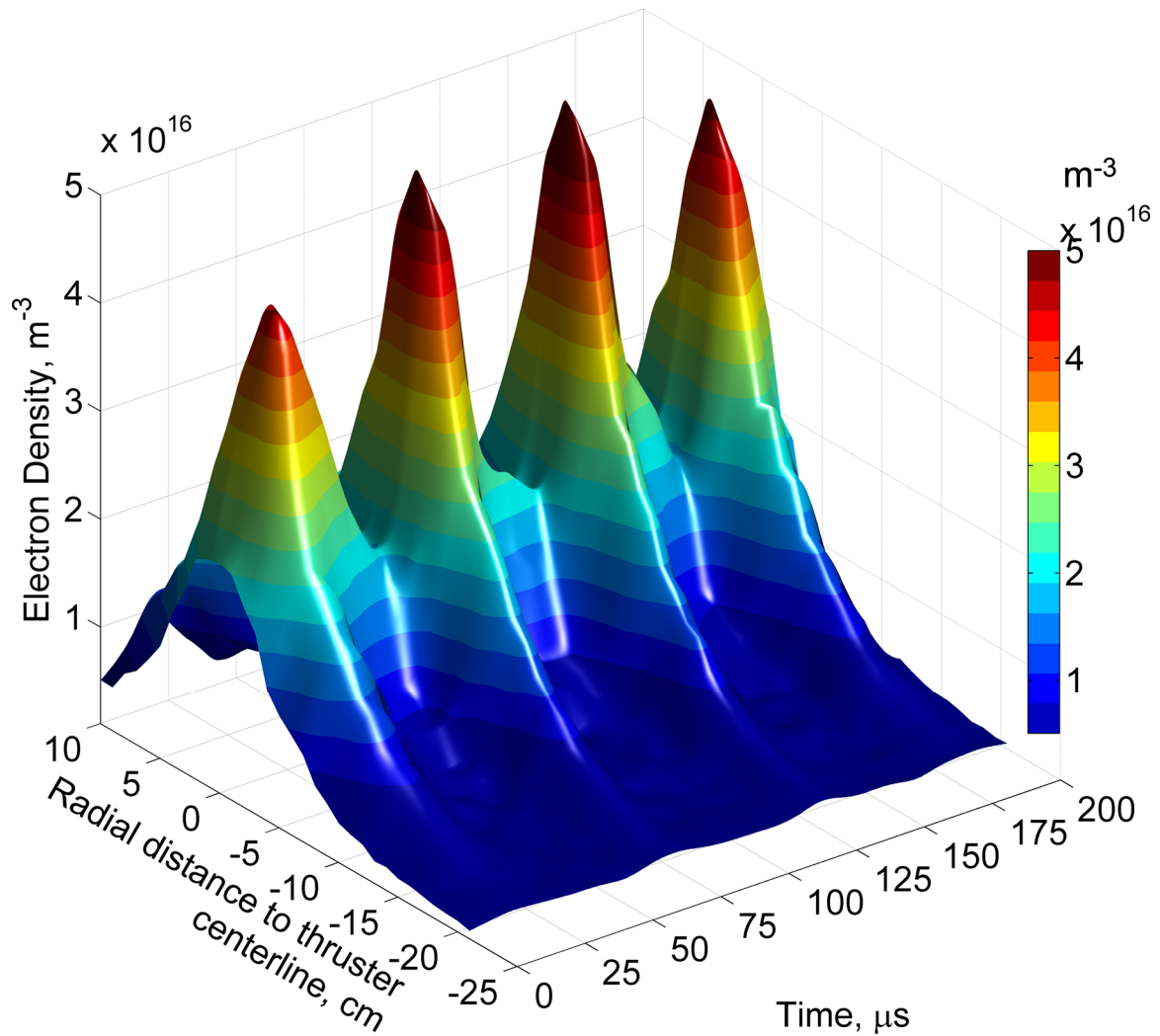


Figure 6.20. 3D plot ($z = n_e$, $y =$ radial-position, $x =$ time) of radial profile transient axially travelling plasma density waves. The 31 cm wide radial profile is at a fixed position 25 cm axially downstream from the 200 V 2 A HET discharge exit-plane.

The four mountains of density shown in Figure 6.20 exhibit 21 μs delays with corresponding HET discharge current breathing mode oscillations due to ion transit time to this position 25 cm downstream. The density scaling in this figure is linear (unlike the previous two figures that were logarithmic) and this scaling really emphasizes the magnitudes of the travelling ion wave as it propagates from the thruster.

Considering the temporal evolution of a single axial profile of electron density at a fixed radial position aligned approximately with the middle of the left side of the discharge channel (opposite of cathode), Figure 6.21 may be constructed. The three axes in this figure represent x = axial position, y = time, and z = electron density, discharge current, and FASTCAM intensity. The color-mapped surface plot clearly displays a series of four distinct plasma waves emitted by the HET at an average velocity of 13 km/s. A series of 23 FASTCAM photos are positioned at their respective times of acquisition as well as the actual position of the thruster exit plane (e.g., axial position of 0 cm). These originally monochromatic photographs have been colorized on the same relative scale as the electron density surface contours, but with arbitrary units. A pair of traces representing the measured discharge current (in Amperes) and integrated FASTCAM intensity (in normalized arbitrarily units) signals are included to emphasize how the fluctuations of these well correlated signals produce corresponding fluctuations in the plume electron density axial profiles. Each breath of xenon creates a density wave that takes about 45 μs to travel the full axial extent of the grid (measuring from spike in FASTCAM intensity at 0 cm to center of the density ripple at 60 cm), which gives an average ion velocity of about 13 km/s for the axial region from 0 to 60 cm.

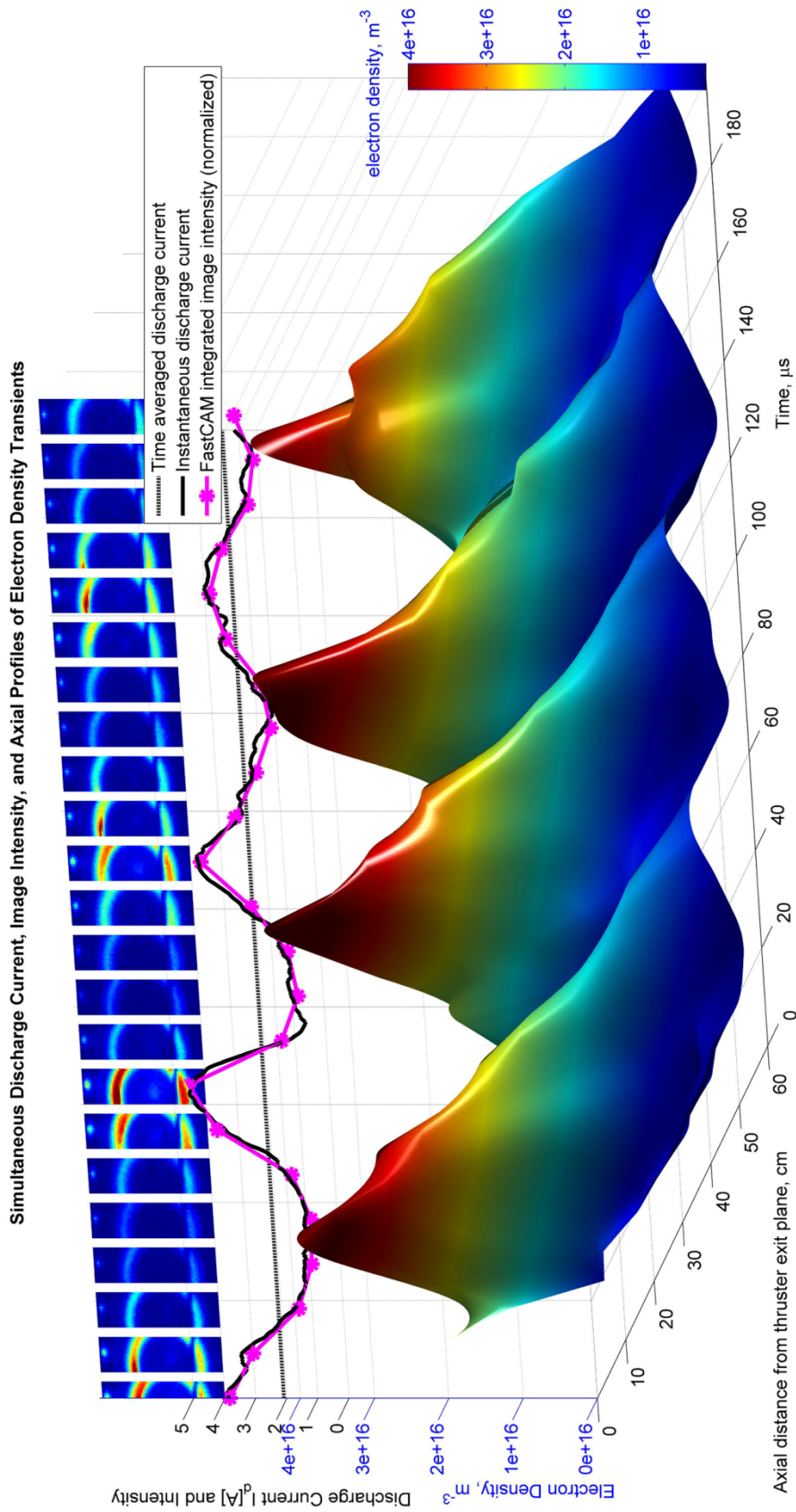


Figure 6.21. Travelling waves of plasma exhausted by a 600-W HET depicted in three simultaneously sampled signals. The upper series are of video frames are acquired by the FASTCAM camera at a frame rate of 109,500 fps (with separate colormap scaling of 10-bit intensity). The middle traces (in black and magenta) show instantaneous discharge current and integrated FASTCAM frame intensity. And the lower surface plot of the electron density tracks temporally evolving waves as they propagate axially downstream from the thruster at 13 km/s. Each wave is a “breath” of xenon characteristic of the breathing mode phenomena inherent to Hall thruster operation; the breathing mode frequency for this 200-V, 2-A discharge is 19 kHz.

6.7 Space and Time Resolved Results for Clustered HETs

Using the High-speed Dual Langmuir Probe system (HDLP, described in Chapter 3) and a high-speed camera, measurements of 19.6-kHz waves of ionized propellant emitted by the unsteady ionization process or “breathing mode” from a cluster of Hall thrusters are presented in this Chapter. [112] Two 600-W, low-power Hall thrusters were operated together in close proximity with 200-V, 2-A xenon discharges, producing the plume examined in this study. Large amplitude plasma oscillations, with peak-to-peak magnitudes approaching 100% of the DC level, are observed in the near- and far-field plume electron density, optical intensity, and thruster discharge current. The HDLP system acquired the plume electron density in a planar grid measuring 0.31 m radially, centered on cluster centerline (with 10-mm spacing), and 0.5 m axially downstream (with 50-mm spacing). The structural evolution of the exhausted plasma density fluctuations was resolved for this entire grid at a rate of 100 kHz (using spatiotemporal fusion with the HDLP data) while a high-speed camera imaged the two discharge channels at a rate of 67,500 frames-per-second (with the discharge currents of each thruster sampled at 2 MHz). Recorded synchronously, these independent spatially and temporally resolved measurements correlate well with each other and reveal the complex nature of the interactions between the two simultaneously discharging Hall thrusters. Interactions in the near-field plume prove viable enough to encourage coupled breathing mode oscillations, in which the thrusters preferentially breathe in an in-phase “mode-0” (observed 43.4% of the run duration) or an opposite-phase “mode-1” (36.1%) manner. Comparisons of these coupled breathing mode oscillations observed in the clustered thrusters are made with single-thruster breathing mode oscillations. For both

configurations, a non-dimensional, localized electron density mean fluctuation peak-to-peak magnitude of about $72\% \pm 10\%$ is seen at most radial and axial plume locations.

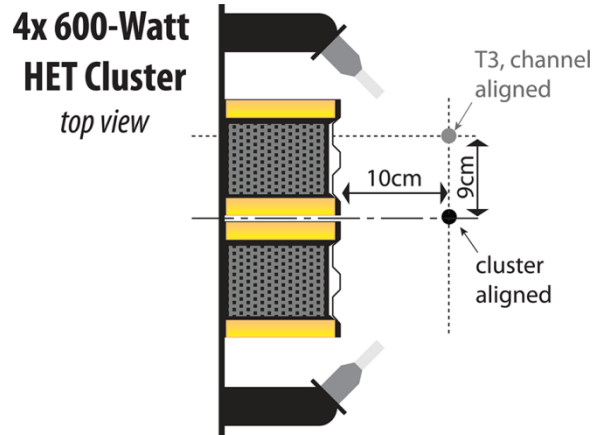


Figure 6.22. Illustration of T3 discharge channel aligned (light gray) and cluster aligned (black) plume positions examined in Figure 6.23.

6.7.1 Single-point Plasma Property Fluctuations

Using the spatial-temporal data-fusion technique detailed in Chapter 5, one may then examine the entire two-dimensional plume region on a fixed set of temporally aligned intervals. For example, at the two radial locations illustrated in Figure 6.22, simultaneous plasma oscillations are presented in Figure 6.23 (at (a) $R = 9$ cm and (b) $R = 0$ cm) for a fixed sequence of thruster discharge current fluctuations (2x cluster mode with 200-V and 2-A HET settings). The distinct 19.6-kHz breathing mode type oscillations observed in Figure 6.23(a) are similar to oscillations seen when running this thruster unclustered that have been detailed throughout preceding portions of this chapter. Since this position is separated radially from the axis of the neighboring thruster by over 10 cm, less influence is indeed expected. However, on cluster centerline as in Figure 6.23(b), nearly equivalent fluctuation contributions are provided by each breathing HET, thus creating less distinct plasma oscillations. The sum of the two thruster discharge

currents is included since the measured density transients appear to follow this effective signal (as expected from clustered HET plume density super-positioning [40]).

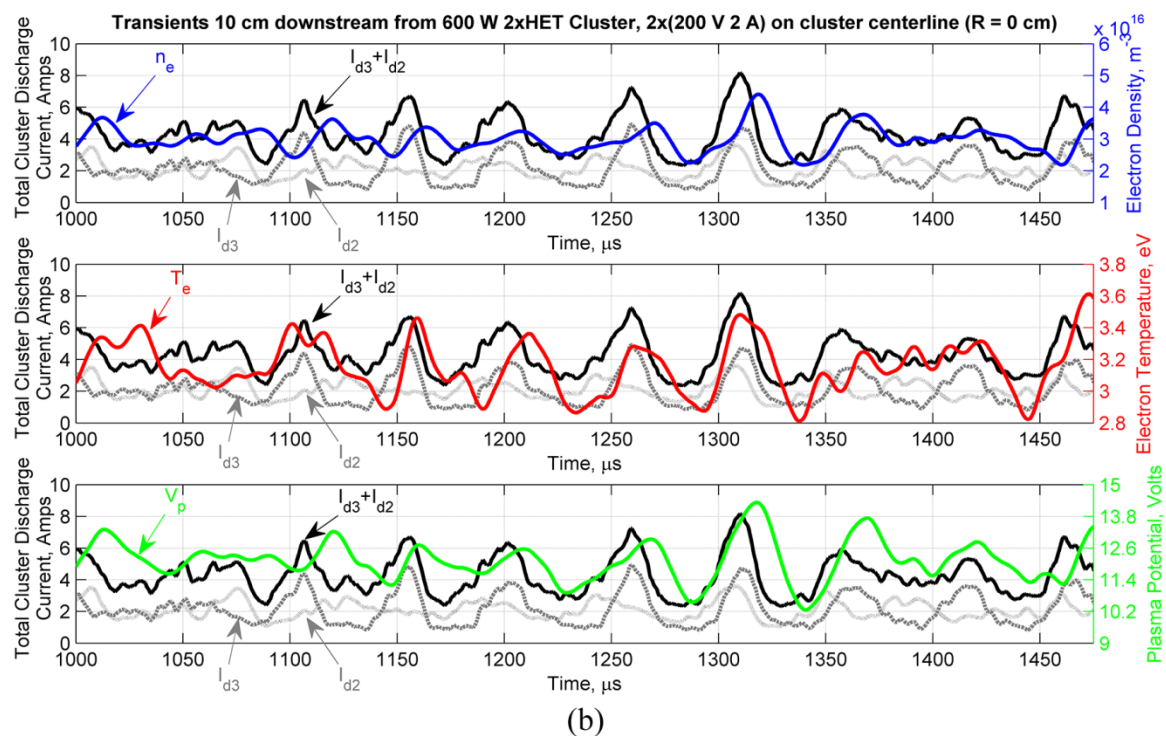
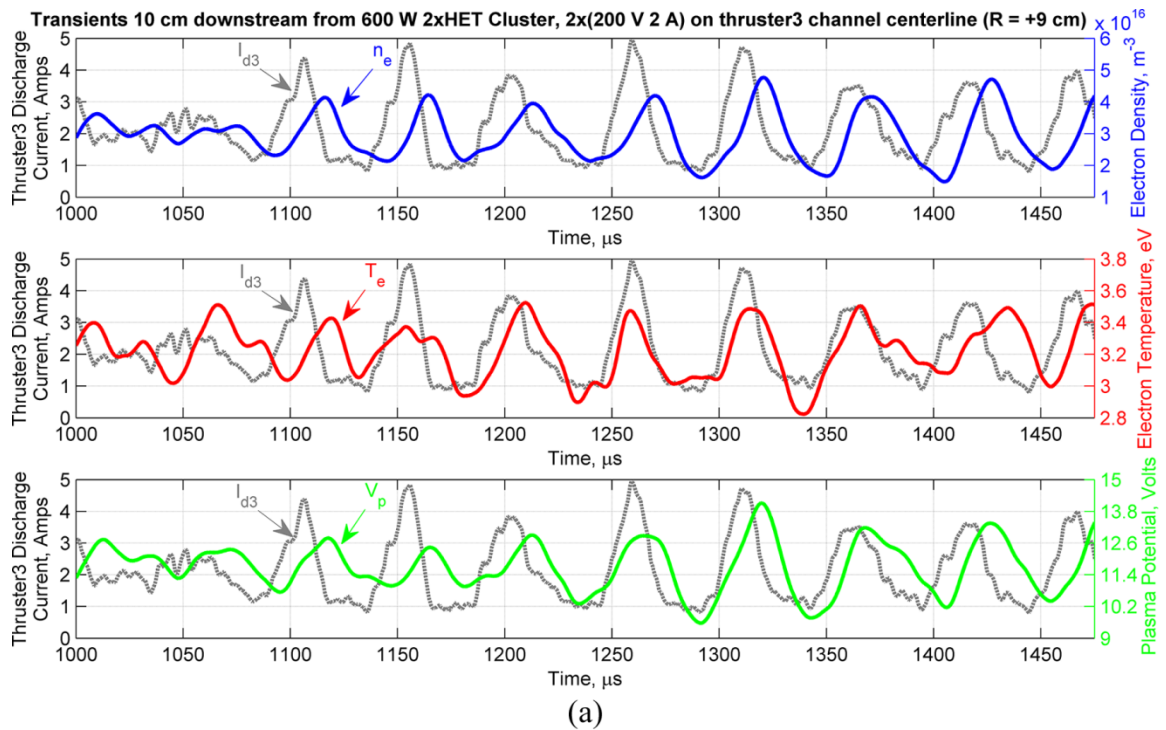


Figure 6.23. Single-point, simultaneous plume electron density, electron temperature, plasma potential, and clustered HET discharge currents for two radial positions. (a) T3 discharge channel aligned (outer edge, away from T2) plume properties. (a) Cluster aligned properties including both separate thruster anode currents (I_{d3} and I_{d2} , gray dashed) and superimposed current ($I_{d3}+I_{d2}$, solid black).

6.7.2 Clustered Modal Behavior

Examination of the time-series signals suggests that the thrusters seem to prefer oscillating at the breathing mode in-phase with each other in what shall be defined as "mode-0." To quantify this behavior, the instantaneous phase between $I_{d3}(t)$ and $I_{d2}(t)$ is determined for a large set of samples. Using the same approach applied to compute ion transit time delays, this is performed efficiently in frequency-space, where the phase between the signals at the breathing mode is simply the angle between the real and imaginary terms of the transfer function. The stochastic form of this phase encourages a statistical treatment. Thus, the probability density function (PDF) for all possible phases (at the breathing mode) is constructed by binning all phase states as in Figure 6.24. If the clustered thruster oscillations were entirely uncorrelated to one another, then a normal PDF (flat between -180° and $+180^\circ$) would be observed. However, two preferred modes of oscillation are observed: Mode-0 with 43% integrated probability and mode-1 (opposite phase oscillations) with 36% probability. The remaining 21% of oscillations appear at phases between mode-0 and mode-1 suggesting brief intermodal transitions. The predominance of mode-0 breathing mode oscillations produces more intense plasma waves as the thrusters breathe in-phase. The close thruster positioning in the cluster tested is the likely reason for increased mode-0 oscillations since the thruster plumes possess considerable overlap. In particular, overlap in the external edges of the acceleration zones would surely give rise to coupled thruster oscillations due to the key role of the acceleration zone in breathing mode models such as presented in Section 1.6.

[23]

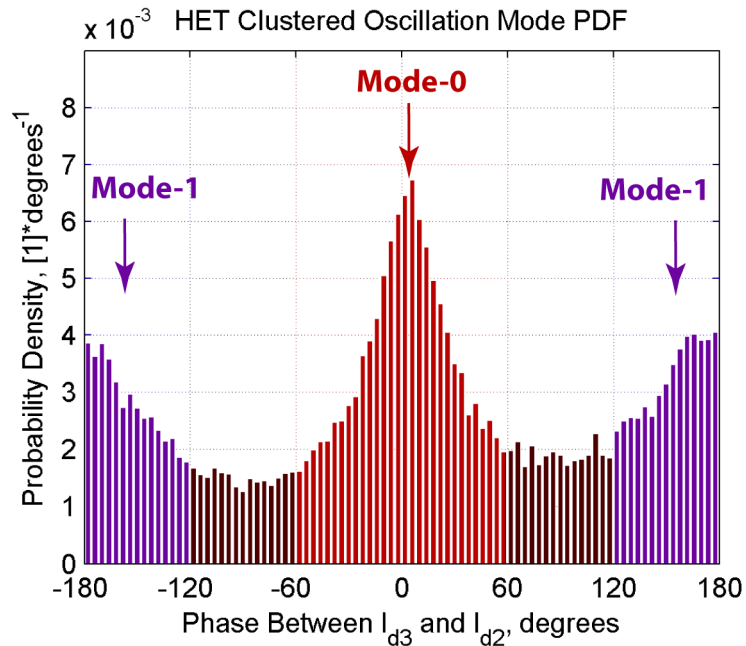


Figure 6.24. Probability density for measured phase between clustered thruster oscillations. Predominate with 43% integrated probability is mode-0, with clustered thrusters oscillating in-phase.

The Hall thrusters in this cluster are as close to each other as is physically allowed by the encasing outer electromagnets, thus the figure of 43% mode-0 behavior is likely an upper limit for clustered HETs. On real spacecraft, the thrusters would likely have additional spacing to alleviate thermal and vibration (launch) interactions. While the clustered experiments here were only performed with two thrusters, additional thrusters would increase the number of possible modes. Preliminary measurements with operating all four (2x2) HETs confirm this with the appearance of four dominant modes (mode-0 all in-phase, mode-1 right or left HETs in-phase, mode-2 upper or lower HETs in-phase, and mode-3 diagonal HETs in-phase) as shown in Figure 6.25.

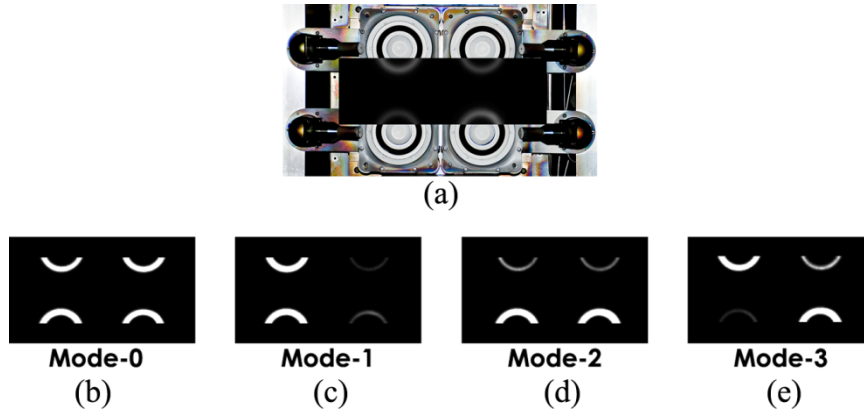


Figure 6.25. Additional clustered modes identified using high-speed imaging. The same (b) all-thrusters in-phase mode-0 appears, but there exist three different modes (c)-(e) where only two thrusters are in-phase.

6.7.3 2D Maps of Time-averaged and Fluctuation Amplitude Electron Density

The collected time-resolved planar electron density contour maps of clustered HET operation enable dramatic frame-after-frame animations, but the stochastic nature of the visualized breathing mode oscillations is best quantified by maps of the mean statistics. Thus, in Figure 6.26, the time-averaged electron density and mean fluctuation peak-to-peak amplitude planar contour maps are presented. Slight differences in the thrusters lead to a small degree of asymmetry in the time-averaged and mean fluctuation amplitude maps. As was seen with single thruster operation (in Figure 6.18), the mean peak-to-peak electron density fluctuation amplitudes nearly match the time-averaged electron densities at the same plume positions. Overall, these data compare surprisingly well with the single thruster data in Figure 6.18(a)-(b), suggesting that both the density time-averaged values and fluctuation values directly superimpose. Calculating the spatially-averaged ratio of the fluctuation mean over temporal mean yields Eqn. (6.8).

$$\left\langle \frac{n_e'_{pk2pk}}{n_e} \right\rangle_{plume(31cm\ by\ 50cm)} = 0.72 \quad (6.8)$$

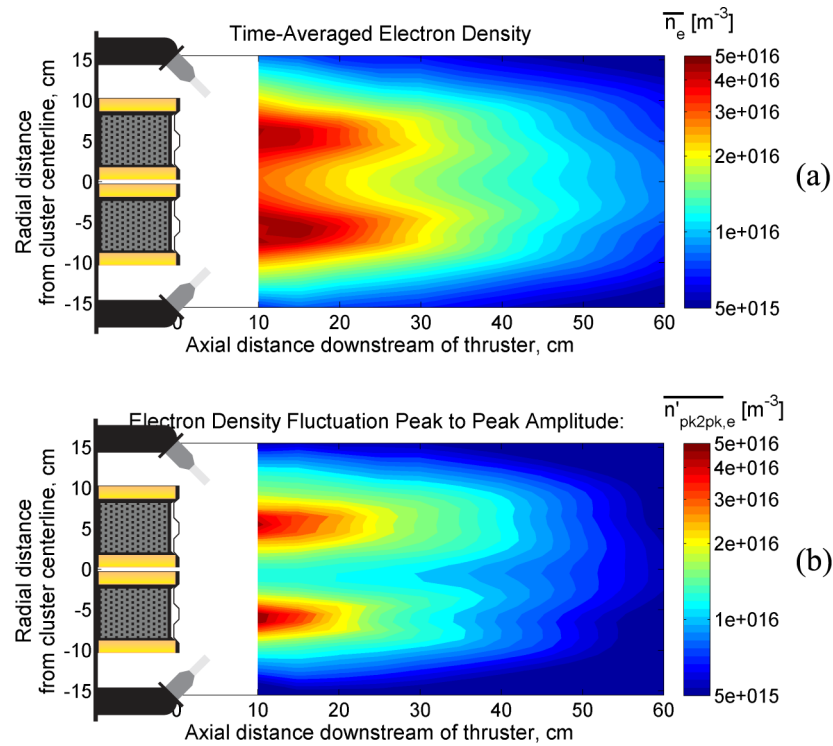


Figure 6.26. Clustered electron density contour maps of (a) HDLP time-averaged and (b) fluctuation peak-to-peak amplitude values. Both (a) and (b) are plotted on the same logarithmic colorbar scale, emphasizing the large magnitudes of the emitted density waves relative to the local DC electron density values.

Equation (6.8) lists the measured mean "non-dimensional fluctuation magnitude" which varies only by about ± 0.1 throughout the entire 31-cm by 50-cm plume region investigated with clustered operation. A similar, non-dimensional fluctuation amplitude was observed with single thruster operation (see Section 6.6.1). [113] With both cases, the relative amplitude of the breathing mode oscillations remains constant (to within about 10%) throughout the entire plume region studied. This implies the undamped

persistence of breathing mode induced ion waves in all space downstream (with line of sight) from a HET until complete plume neutralization is reached.

6.7.4 Temporally and Spatially Resolved Electron Density Results

Figure 6.27 examines full planar plume density contour maps in a time-resolved sequence of frames that capture a complete mode-0 breathing mode cycle. The discharge current signals for each thruster (T3 is upper and T2 is lower, see Figure 2.3) are included to the left of each time-stamped contour map with a red asterisk marking these simultaneous current signals. The short delay (about 10 μ s) between a burst of current and arrival of this transient at the plume map edge arises from propellant ion transit at an average velocity of 10.4 km/sec. Simultaneous FASTCAM photos are included at the approximate position (and scale) of the actual clustered HETs. These photos image a section of the thruster exit planes (i.e., looking directly into the annular discharge channels), which is perpendicular to the contour map. It should be noted that to enable various signal processing steps (and prevent information loss), all signals are digitally resampled to a common 2 MHz rate. The colorbar in Figure 6.27(g) corresponds only to the 31-cm by 50-cm plume region electron density contours in (a)-(f). The discharge current and photo intensity (F_{T3} and F_{T2}) signals are mutually in-phase for each thruster, and since a mode-0 type transient oscillation is occurring, the thrusters are in-phase with each other. During a breathing mode ionization burst, a large quantity of leakage electrons are pushed towards the anode, very rapidly producing a large (positive) spike in discharge current while simultaneously the increased ionizing (as well as classical cross-field electron transporting random walk) collisions emit lots of photons (from atomic state transitions). The rapid electron and photon velocities (compared to the slow ions)

serve to place the current and photo signals in phase (with the expected small phase difference being too small to resolve with the finite DAQ rates). The set of six frames in Figure 6.27 depict a typical breathing mode oscillation, with similar transient behavior repeating indefinitely at a rate of 19.6 kHz. Longer sequences confirm the finding in Section 6.7.2, with 43% of the breathing mode cycles occurring with both thrusters emitting waves of ions in phase with each other.

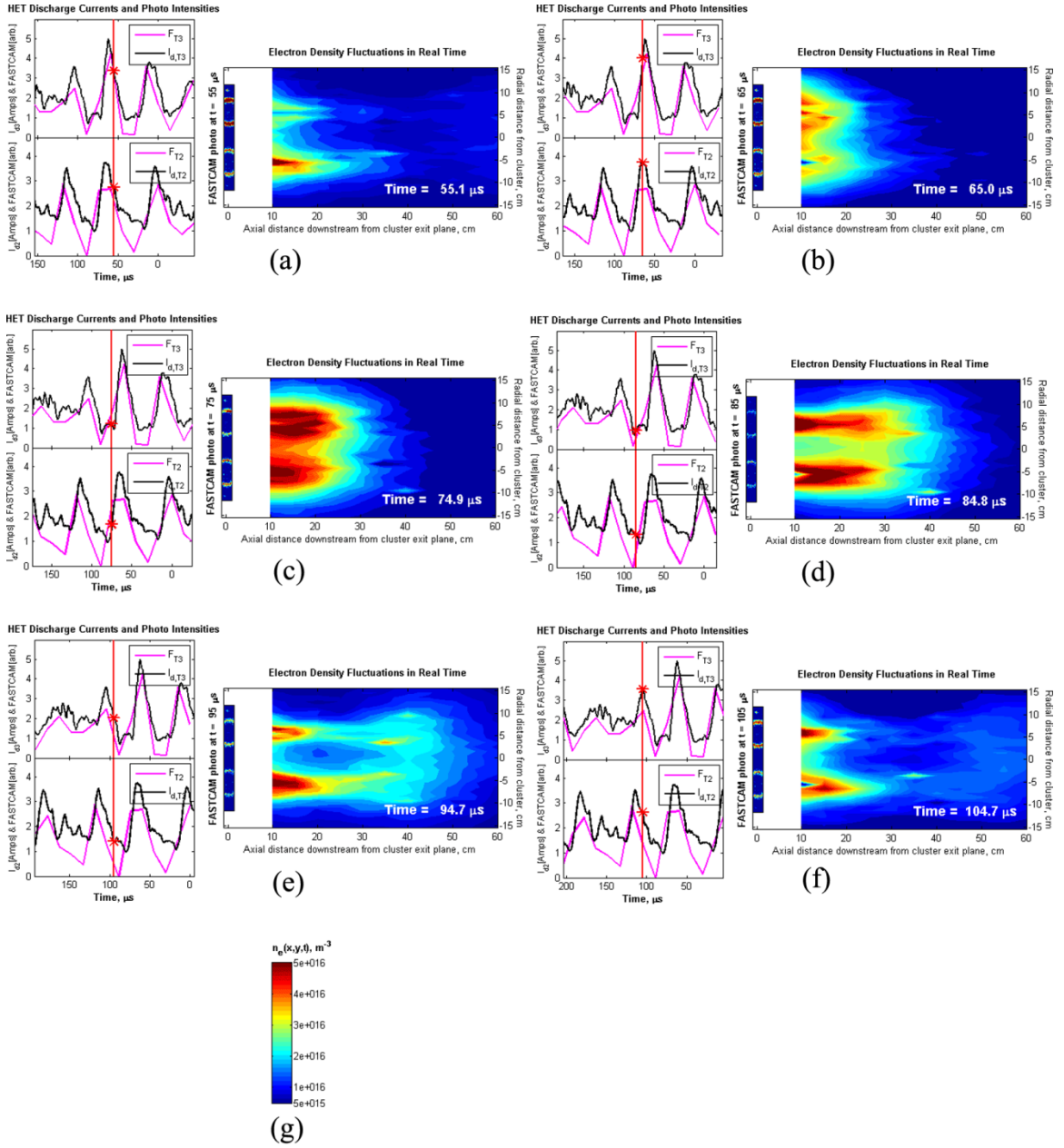


Figure 6.27. Temporally and spatially resolved electron density contours for one (mode-0 type) breathing mode sequence. The simultaneous multi-rate signals of discharge current (sampled at 2 MHz), photo intensity (67.5 kHz), and electron density (100 kHz) are included for each time interval: (a) $t = 55.1 \mu s$, (b) $t = 65.0 \mu s$, (c) $t = 74.9 \mu s$, (d) $t = 84.8 \mu s$, (e) $t = 94.7 \mu s$, and (f) $t = 104.7 \mu s$. Colorbar (g) applies to all planar density maps.

By considering the fixed radial ($R = 0$) position on the cluster centerline, axial waves of electron density are observed in Figure 6.28. The rear wall of this figure contains the temporally synchronous discharge current and photo intensity signals. FASTCAM photos at the corresponding times are also included, and as the rear wall axial coordinate is 0 cm, these photos are coplanar with the thruster exit planes. In this plot, the first oscillations by each thruster are nearly opposite-phase or mode-1 type. The resulting axial density wave from this mode-1 event is less distinct since the transient density contributions from each thruster somewhat cancel each other out. The sum of both clustered thruster discharge currents is included (as was done in Figure 6.23) to show how the density waves track this net signal as anticipated from super-positioning.

[40]

Simultaneous Time-resolved Plasma Measurements Downstream of 2x 200V 2A HET Cluster on Centerline

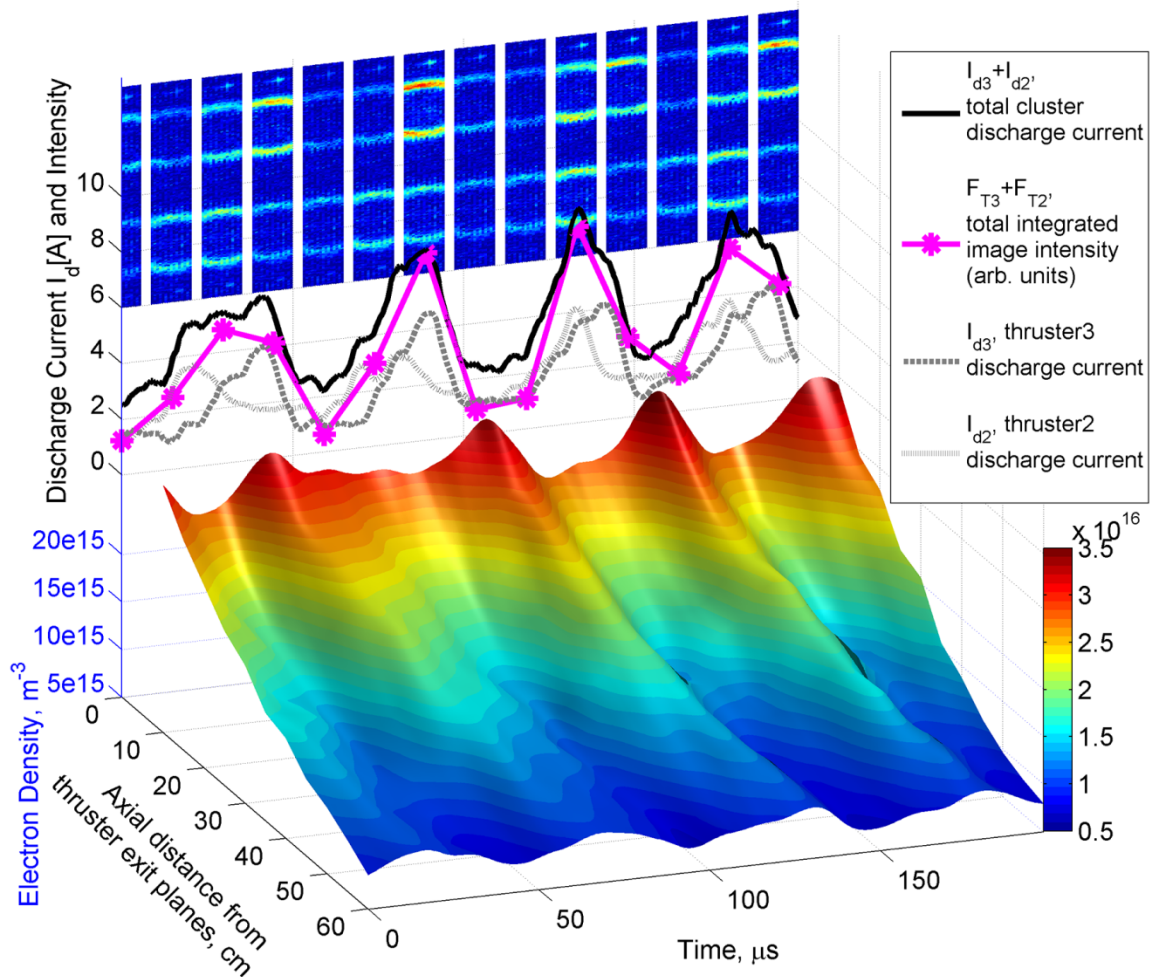


Figure 6.28. 3D axial electron density wave profiles on cluster centerline ($R = 0$). The vertical axis combines all properties including: the time-resolved centerline electron density in blue (also colorbar scaled), separate thruster discharge currents (I_{d3} and I_{d2}), summed discharge currents ($I_{d3} + I_{d2}$), total integrated intensity ($F_{T3} + F_{T2}$), and the time-aligned FASTCAM photos.

6.7.5 Conclusions

The discharge from two simultaneously operated, low-power Hall thrusters has been temporally and spatially resolved revealing large magnitude property oscillations. These breathing mode oscillations occur in all measured plasma and thruster properties including: thruster discharge currents, electron density, electron temperature, plasma

potential, and photo intensity. Even with independent thruster setups, a 43% tendency exists for in-phase thruster (mode-0) oscillation. Super-positioning appears to hold with clustered Hall thruster density fluctuations as well as with DC densities. The overall dynamic behavior of clustered Hall thrusters is quite similar to single thruster operation, with both configurations having non-dimensional localized electron density fluctuation (peak-to-peak over mean) magnitudes near $72\% \pm 10\%$ throughout the entire downstream near- and far-field plume.

Chapter 7

Summary and Future Work

A strong global demand to develop advanced electric propulsion systems such as Hall thrusters has matured the technology to present day efficiencies in excess of 60%. However, portions of the physics describing these devices are still evolving (e.g. anomalous electron conductivity, and erosion mechanisms). One shortcoming apparent in the predominant pre-existing base of HET measurements was a detailed temporal view of the discharge process. This dissertation developed a novel High-speed Dual Langmuir Probe (HDLP) to address this inadequacy of time-resolve HET measurements. The construction of the diagnostic was detailed and its theory and limitations discussed. Time- and space-resolved HDLP measurements were performed within the plume of single, as well as clustered, modern low-power HETs. The large amplitude breathing mode fluctuations characteristic of Hall thruster operation were observed in the thruster discharge current signal (as expected), but were also observed in the electron density, electron temperature and plasma potential measurements. Strong correlations were computed between the various fluctuating properties including relationships in the fluctuation magnitudes and their relative phases. Several thruster settings were investigated and for all cases, configurations, and spatial locations, turbulent breathing mode fluctuations dominated the temporal plasma property measurements. A novel method of spatiotemporal data fusion was developed to overcome the temporal

incoherence of the single-point HDLP measurements. Application of this technique revealed dramatic ion plasma waves propagating from the thruster with each discrete breath of ionized xenon (schematically drawn in Figure 7.1 with various scaling terms discussed in Chapter 6).

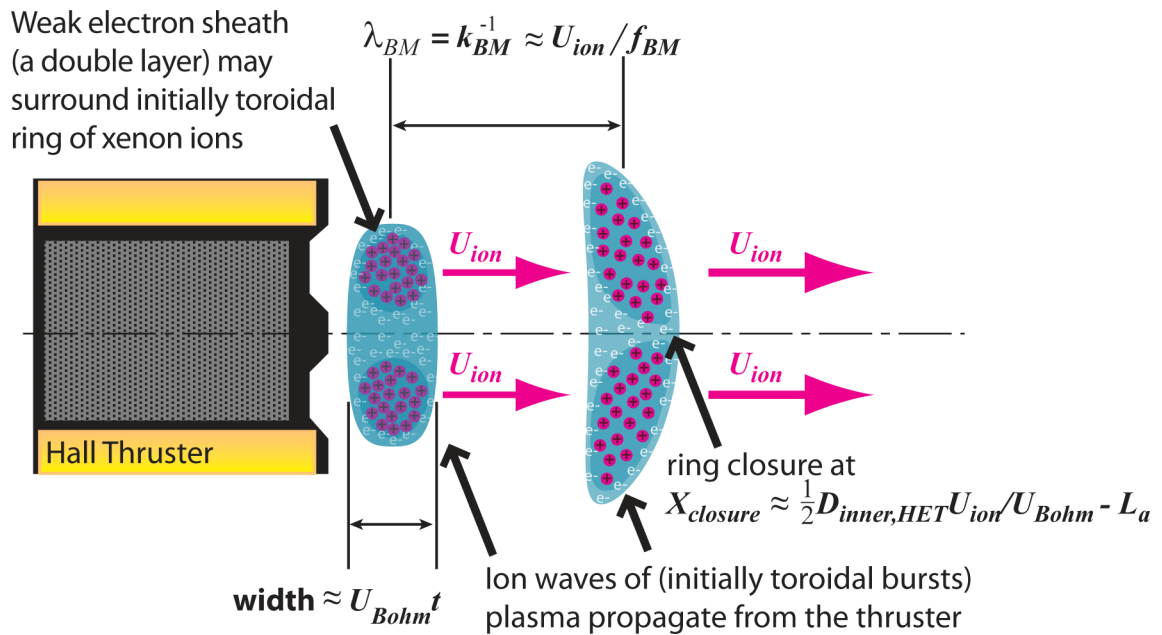


Figure 7.1. Schematically exaggerated view of the electrodynamic Hall thruster breathing mode with simple scaling relations.

This time-resolved investigation of the HET plasma has unveiled a discharge process rich in oscillatory behavior. The labeling of closed drift Hall effect thrusters as "electrostatic" devices is highly misrepresentative of their nature and these devices should be reclassified as electrodynamic thrusters. To emphasize this point, an estimation of the time-resolved propulsive thrust from a Hall thruster is now derived. From the definition of thrust in Eqn. (1.1) and an exhausted ion energy (and velocity U_i) set by the ion mass, m_i , and the discharge voltage, V_D , ($\frac{1}{2} m_i U_i^2 = e V_D$) the following expression of thrust is obtained:

$$T = \frac{d}{dt}(mU_i) = \dot{m}U_i + \sqrt{\frac{em_i}{2V_D}} \frac{\partial V_D}{\partial t} = \frac{m_i}{e} I_D U_i + \sqrt{\frac{em_i}{2V_D}} \frac{\partial V_D}{\partial t} \quad (7.1)$$

Differentiating again to examine the temporal variation in thrust, and ignoring the second order terms that arise from the final term of Eqn. (7.1),

$$\frac{\partial T}{\partial t} \approx \frac{m_i U_i}{e} \frac{\partial I_D}{\partial t} + I_D \sqrt{\frac{m_i}{2V_D e}} \frac{\partial V_D}{\partial t} + \dots \quad (7.2)$$

Now, the fluctuation amplitude during one breathing mode oscillation should approximate the standard deviation amplitude from a collection of time-resolved data.

Using this allows one to express the partial derivatives as (for example with the discharge current), $\frac{\partial I_D}{\partial t} \approx \tilde{I}_D \cdot (2\pi f_{BM})$. Applying this to the partial derivatives in Eqn. (7.2) and

approximating the remaining terms at their time-averaged values obtains:

$$\tilde{T} \approx \frac{m_i U_i}{e} \tilde{I}_D + \overline{I_D} \tilde{V}_D \sqrt{\frac{m_i}{2V_D e}} \quad (7.3)$$

Finally, dividing by the time-averaged thrust, $\overline{T} = m_i \overline{U_i} \overline{I_D} / e = \overline{I_D} \sqrt{2m_i \overline{V_D}} / e$, achieves the estimation of the fluctuation in thrust given breathing mode plasma oscillations:

$$\frac{\tilde{T}}{\overline{T}} \approx \frac{\tilde{I}_D}{\overline{I_D}} + \frac{1}{2} \frac{\tilde{V}_D}{\overline{V_D}} \quad (7.4)$$

For the HDLP plasma measurements obtained for the 600-W HET studied in this work, the fluctuations in thrust are roughly $\left. \frac{\tilde{T}}{\overline{T}} \right|_{600\text{-W HET}} \approx 75\%$. Certainly, any electric propulsion device with this magnitude of thrust oscillation would not be classified as electrostatic.

7.1 Future Work

The developed HDLP diagnostic provided measurements of unprecedented spatial and temporal detail within the HET plume. However, the examination of the temporal limitations of the probe in Chapter 4 suggested that an upper probing rate of 1 MHz is possible. Future development of this capability is already underway, and the finer temporal detail (coupled with a faster 1-Mfps high-speed camera) will enable the examination of higher-frequency plasma oscillations such as the azimuthal modes (ionization, transit-time, drift instability, etc.) common in the very-near-field of HETs. To that end, future measurements using the HDLP to perform internal time-resolved measurements would be tremendously insightful. The strong magnetic fields in this region are known to exhibit anomalous electron transport, and with detailed time-resolved measurements, one could examine the nature of turbulent transport. Additionally, the use of a HDLP for obtaining time-resolved electron energy distribution functions is very promising (see Figure 3.9(d)). Measurements of the unsteady state of electron equilibrium could help identify transient plasma phenomena that could be tailored to enhance the efficiency of ionization and acceleration. While HETs are already rather efficient devices, the developed diagnostic capabilities could provide new insights with time-resolved measurements in other plasma systems (e.g. fusion research endeavors, pulsed plasmas, and field reversed configuration devices, etc.).

Appendix A

Measurements of Thrust from Clustered Hall Thrusters

A cluster of four 600 Watt Hall thrusters has been evaluated in terms of performance characteristics including the measurement of (time-averaged) thrust, anode efficiency, and anode specific impulse. [44], Operation of Hall Effect Thrusters (HET) in a clustered configuration may conceivably lead to increased concentrations of charge exchange ions, amplified discharge current instabilities, and direct increases in thrust (due to localized re-digestion and plume-focusing effects).[40] In an effort to quantify these speculations, analysis of 600 Watt fixed-power performance is conducted in various configurations including: single-thruster, dual-thruster, tri-thruster, and full-cluster (4-thruster) operation. The total thrust generated by the clustered operation of the 600 W thrusters is observed to exceed, by 3.6%, the sum of thrusts from the same thrusters when operated singly (for a 200 V discharge voltage). Finally, an estimate of the facility effects on thrust is used to demonstrate the chamber-pressure independence of the Large Vacuum Testing Facility (LVTF) utilized for these tests involving the low power HET cluster (setup shown in Figure A.2). Results from the clustered configurations and from the single thruster configuration are presented with operational set-points determined by tuning the magnetic circuit and mass flow rates for optimal thrust to power and optimal efficiency at discharge voltages from 150-V to 600-V.

A.1 Performance Measurements

In this appendix, the performance effects from clustering multiple identical Hall thrusters are investigated. Thrust, specific impulse, and efficiency are among the various performance parameters that are measured. For the purposes of data consistency, all performance measurements are gathered at a fixed power level of 600 Watts, as this is the base power level of a single 600-W Hall thruster used in these experiments. To further the comparability of data in the differing clustered configurations, performance measurements will largely be expressed in a per thruster normalization basis—that is to say, for example, that the total thrust generated by operating the full cluster of four Hall thrusters simultaneously, is divided by four and reported as the effective single thruster thrust (or “per thruster thrust”). In this manner, trends due to any clustered configuration of Hall thrusters are directly observable by monitoring the trends in the measured performance parameters of thrust, I_{sp} , and efficiency.



Figure A.2. Internal view of Hall thruster cluster from within the LVTF. Cluster is mounted upon the NASA-type inverted pendulum thrust stand, near the radial center of the vacuum chamber. The seven cryogenic pumps are clearly visible. This photo was taken shortly before pumping down to vacuum conditions.

A.2 Thrust Stand and Performance Measurements

The measurement of the force signal resulting from the thrust produced by the operation of the 600-W Hall thrusters is executed with a NASA-GRC type inverted pendulum Null balanced thrust stand [114]. A linear variable displacement transducer (LVDT) is used to measure the small displacement caused by the thrust force applied. This LVDT signal is the input to a commercial Stanford Research Systems closed-loop proportional, derivative, and integral (PID) feedback controller (model SIM960). The PID output is amplified with a linear power supply and applied to a null balancing electromagnetic coil to restore the thruster platform to the initial set-point. This commercially available OTS (off the shelf) solution to control the null coil was only recently implemented at PEPL [115] and improves the accuracy, repeatability, and ease with which thrust measurements are performed. The magnitude of this PID output (the null signal), is proportional to the force applied to the thruster platform. Small weights strung along a two-pulley system may be remotely lowered with a small DC-motor, thereby applying a series of small forces to the thruster aligned parallel to the thrust force. In this manner, the proportionality constants between the null signal (in mV) and the thrust force (in mN) are ascertained from a linear regression as shown in Figure A.3. Calibrations of this type are performed for each measurement of thrust reported in this appendix. While the average slope from all 47 tests performed exhibits a variance of only 0.43%, the zero point (with zero thrust production and no weights applied) shifts are significant due to thermal loading and other effects. Thus, calibrations are performed for every measurement of thrust. The mean correlation (Pearson) coefficient from all 47 calibrations is $R^2_{ave} = 0.99993$ (minimum $R^2_{min} = 0.99951$). The procedure followed for each measurement of thrust is as follows:

- 1) Start cathode keepers if not already running
- 2) Initiate desired xenon flow to anode, wait two minutes
- 3) Activate Hall thruster(s) and set all power supplies to appropriate settings, shutting off keepers
- 4) Wait thirty minutes or more until discharge current and thrust signals level out (changes less than 1% per 5 minutes are considered “leveled out”)
- 5) Record the null signal representing thrust—immediately afterwards extinguish discharges by shutting down discharge supplies and closing propellant flow lines but leaving magnets on (cathode keepers are turned on prior to thruster shutdown)
- 6) Two minutes after shutdown record zero point of the Null signal
- 7) Immediately perform an in situ calibration of the thrust stand using the small weights

The null signal is measured in three separate ways for redundancy: a Fluke 77 III digital multimeter, an analog strip chart, and a PC data acquisition system with a LabView-based strip chart data-logging program. The multimeter specifications provide the best accuracy of the three measurements, and are therefore used as the primary measurement of the null signal (thus used to compute thrust). Even so, the effective resolution of the multimeter is only 12-bits, and this proves to be the dominant source of error in these experiments. The resolution of the null signal, with this setup, is 0.1 mV (or 0.06 mN, in terms of thrust)—as limited by the digits displayed on the multimeter. The error arising from the multimeter null signal measurements tallies an average of about ± 1 mV. The error due to the “goodness” of the calibration linear-fits is determined as well, and averages about ± 0.7 mV. Together these errors give rise to an average accuracy of about ± 1 mN for the measurement of thrust. This represents the absolute error, whereas the repeatability of the measurement of thrust has a significantly improved precision. To quantify the repeatability, a few thruster cases were repeated to measure thrust under the same operational conditions, but on separate days. The half-dozen repeated tests yield a

standard deviation, $\sigma = \pm 0.22$ mN, for both single -thruster and full-clustered operation. Care has been taken in the computation of all accuracies for performance measurements herein reported. Standard methods of error propagation are applied to each measurement of thrust (T), specific impulse (I_{sp}), and efficiency (η). The respective errors are displayed as error bars on all figures in this appendix and these errors fully represent the absolute accuracy propagated into the computation by including all known sources of error (MFCs, thrust stand, displays, power supplies, etc.).

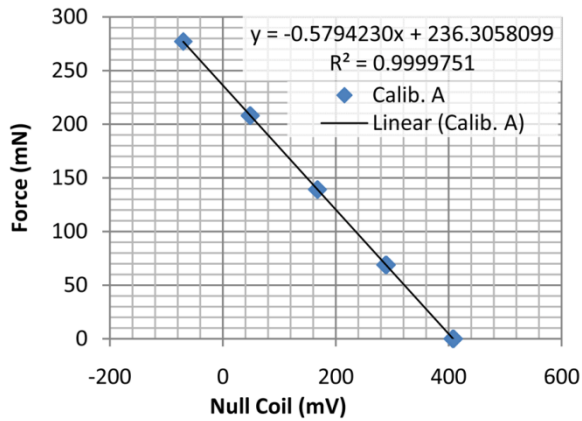


Figure A.3. Sample calibration of thrust stand as measured for test#1. Linear fit parameters are listed. A total of 10 points are plotted (five test masses twice sampled) but overlap quite well due to the excellent repeatability of the calibration.

A.3 Cathode Suspension

Unique to this setup (but not unheard of), the cathodes were suspended away from the 600-W Hall thrusters, thereby isolating them from the thrust stand. This detachment of the cathodes was necessitated by the sheer number of eight xenon flow lines that are nominally required to operate the full cluster. The thrust stand does, however, have four flow lines integrated into its design and thus the four 600-W HET anodes were attached to these. By disjoining the cathodes from the thrust stand, the remaining four cathode flow lines could then be run externally to the cathodes. Other configurations involving

split flows and electrically actuated valves were also considered, but ultimately abandoned, due to complexity issues and significant uncertainties in the per thruster xenon flow. An aluminum frame rigidly supporting the cathodes was attached to the cluster, tightly routing all cathode flow lines and electrical lines to central distribution points. The complete cluster of thrusters was then mounted to the thrust stand and the cathode support frame was externally supported with a rigid connection to an overhanging beam. Once this configuration was attained, the screws securing the cathodes to the Hall thrusters were removed. The cathode frame assembly was then shifted by 3.2 mm to create a safe non-contact gap between the cathodes and the thruster bodies. This shift also effectively pushed the cathode emission tips 3.2 mm closer to the anode exit plane of the cluster. While the positioning of cathodes about HETs is of ongoing interest [116], the measurements by Walker suggest that the performance effects are generally negligible.[117]

A.4 Single Thruster Performance Measurements

In order to characterize the performance of a single thruster within the cluster of 600-W thrusters, the magnetic fields and anode flowrate must be optimized for each discharge voltage under investigation. Optimization occurs when the efficiency of the thruster is maximized. Total and anode efficiencies are defined for an electric thruster as:

$$\eta = \frac{T^2}{2\dot{m}P_T} \tag{A.1}$$

$$\eta_a = \frac{T^2}{2\dot{m}_a P_D}$$

P_T and P_D represent the total electrical power (including inner and outer electromagnets) and the discharge power respectively. The flowrates in Eqn.(A.1) are the total xenon mass flow to the thruster (\dot{m}), including both the anode and cathode; whereas the anode efficiency only includes the anode mass flowrate (\dot{m}_a). The efficiencies defined in Eqn. (A.1) are thruster efficiencies only, and do not incorporate the losses associated with the power supplies (which have efficiencies near 80% at full load). Using the second equation, we can now present results obtained for the quasi-optimization performed with Thruster number 3 (T3).

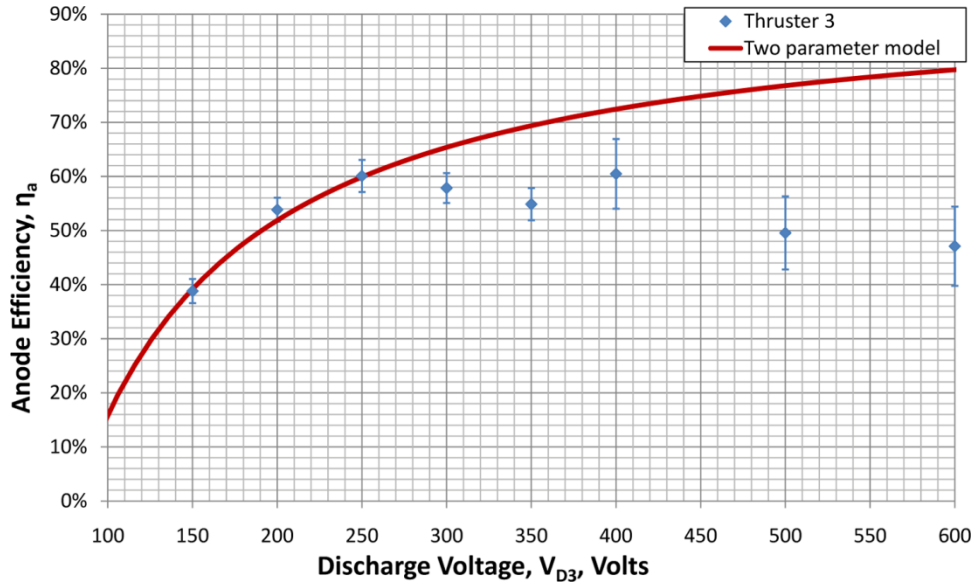


Figure A.4. Fixed power 600 W single thruster anode efficiency at discharge voltages ranging from 150 V to 600 V. Model data is included for qualitative comparison.

Figure A.4 displays the variation of the anode efficiency, at the different discharge voltages examined. Typically, one expects the anode (or total) efficiency of a Hall thruster to increase monotonically with the discharge voltage. This trend is presented as the included “two parameter model” data also shown in Figure A.4. The model, adapted from other Hall thruster “two parameter” models [118] is a rudimentary (but never-the-

less useful) attempt to account for the real-world efficiency behavior of a Hall thruster at different discharge voltages. The model data is only shown here to suggest the expected performance trend of the Hall thruster had the optimization procedure proved more fruitful. The presented experimental data diverge from the model, exhibiting an efficiency plateau at about 200 Volts and then, after 400 Volts, efficiency decay begins. This efficiency loss might be the result of poor propellant utilization at the lower flowrates used for 600 Watt discharges above 400 V. These settings are referred to as quasi-optimal because they may not represent the true optimal setting of the 600-W thruster at the tested discharge voltages. For each discharge voltage, a reasonable effort was applied in the tuning process to find the optimal magnet settings; but the anode flow and cathode flow are not adjusted significantly to enhance the attained optimization. The applied procedure of optimization roughly follows: 1) The anode flow is initially set by an estimate based on the desired discharge current, and the cathode flow is nominally set to 8% of the anode flow. 2) The inner and outer electromagnet currents are varied slowly while watching the efficiency and thrust/power values in real-time (via a LabView data-logging interface). 3) After mapping a sufficient range of magnet settings, the point of maximum efficiency is returned to. 4) Finally, the discharge current is set to the desired value by adjusting the anode flowrate in the appropriate direction (and cathode flow follows at 8% of the new anode flow). 5) Once the desired discharge current is attained and stabilized, the magnet settings are rechecked to confirm the optimization. This procedure is imperfect since the flowrates are not sufficiently tuned. As such, expected trends such as increasing efficiency with increasing discharge voltage may not be correctly captured. Additional experiments are certainly required to more fully optimize

this thruster. For the purposes of the research herein presented, finding the true optimal settings is not necessary. Indeed, the main interest of this experiment is to see how the various performance parameters are affected by the operation of differing clustered configurations. So long as the same quasi-optimal settings are used with each of the thrusters, then the effects caused by clustering Hall thrusters are still accurately characterized.

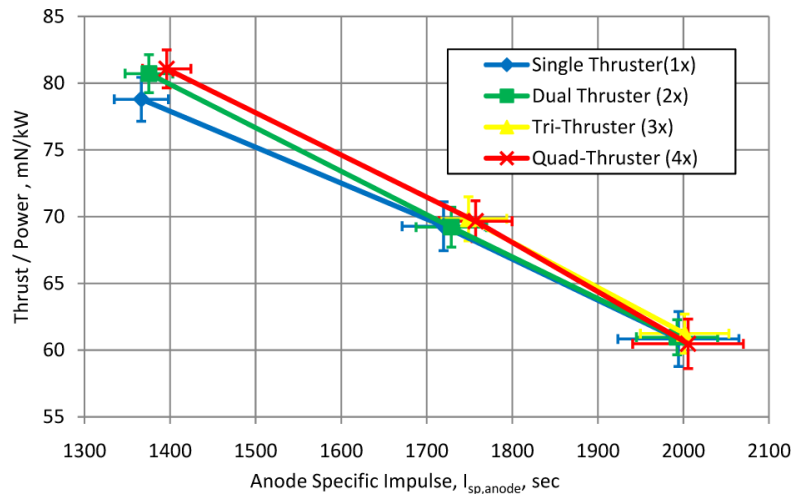


Figure A.5. Fixed-power thrust-to-power trend of quasi-optimized single-thruster performance. Sample model data included for qualitative trend comparison.

Next presented in Figure A.5, is the Thrust to Power (discharge power) versus the anode specific impulse. The anode specific impulse is defined in units of seconds as: $I_{sp,a} = T/(\dot{m}_a g_0)$, with $g_0 = 9.81 \text{ m/s}^2$. The same thrust measurements used here were also used in Figure A.4, but we can now explore the throttleability of the 600-W Hall thruster. Again, some model data is shown in conjunction with the experimentally measured data. A clear peak in the measured thrust to power of 80 mN/kW appears at an anode specific impulse of about 1370 sec. This maximized thrust to power performance corresponds to a 200-V 3-A discharge of the 600-W HET. As seen earlier, the

performance drops as the anode specific impulse (which scales with the discharge voltage as seen in Figure A.6) continues to increase.

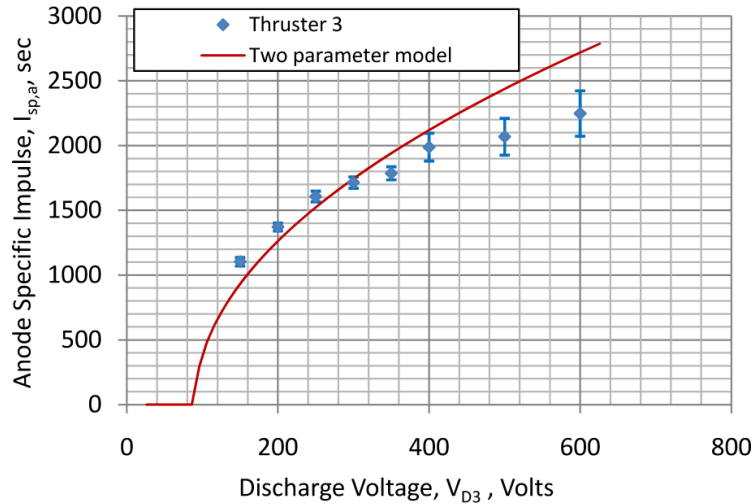


Figure A.6. Fixed-power anode specific impulse for quasi-optimized single-thruster. Sample model data included for qualitative trend comparison.

Having examined the bulk of the measured single thruster performance data, a clear loss of performance is consistently observed at discharge voltages above 300 Volts. There may be several reasons for this performance drop. As mentioned earlier, this could be the result of imprecise optimization. Another possibility is that the operational envelope of this thruster is narrow, and off-design settings, especially at higher discharge voltages, simply run inefficiently. Finally, the “flight-qualified” nature of the 600-W thruster likely leaves little room for increasing the peak discharge-channel-magnetic-field due to a minimized use of heavy magnetic-core materials. The iron-alloy may begin saturating at electromagnetic currents just above the nominal magnet current of 2-A used for the 300-V 2-A discharge settings. Additionally, this lack of extra iron lowers the thermal dissipation mass of the thruster and the risk of nearing the Curie-point temperature of the core materials is increased at higher electromagnet current settings (due to resistive heating of the coils). Indeed, while attempting to optimize performance

at discharge voltages above 300-V, unusual thrust trends were observed when attempting to run the electromagnets with currents in excess of 2.5 A. It is thought that the electromagnets might be overheating at these high settings, thereby lowering the saturation magnetic field-strength, potentially causing saturation and distortion in the magnetic field lines. Lending to this hypothesis was the observation that the electromagnets could be operated at increased currents as high as (4-A) causing noticeable variations in performance—but only for a short period of time, since the discharge current would then drift in a peculiar and inconsistent manner if the electromagnets remained at such current levels. Because of this characteristic, the highest magnet current used in the optimizing of the thruster was 2.5 A. It is quite likely that better high discharge voltage performance optimization would have been achieved if the electromagnets could be reliably operated above 2.5 A.

A.5 Clustered Hall Thruster Performance Measurements

Now that a set of quasi-optimal throttle points have been mapped for a single thruster, various multi thruster configurations are examined using these same settings. In general, manufacturing tolerances could give rise to slightly shifted optimal settings for each thruster within the cluster. In this appendix we shall ignore that possibility, and assume that the quasi-optimized settings determined for thruster 3 will apply as quasi-optimal settings for the remaining three thrusters. In practice, this assumption appeared quite valid, but even so, the variance in the thrust produced by the individual thrusters ranged from ± 1.0 mN or $\pm 2.2\%$ (at $V_D = 200$ V) to ± 0.2 mN or $\pm 0.5\%$ (at $V_D = 400$ V). With measureable differences in thrust among the four 600-W thrusters, additional experiments were deemed necessary to measure the thrust of each thruster at each of

three discharge voltages (200 V, 300 V, and 400 V). While this squared the intended test-matrix, it yields the impressive results in Figure A.7.

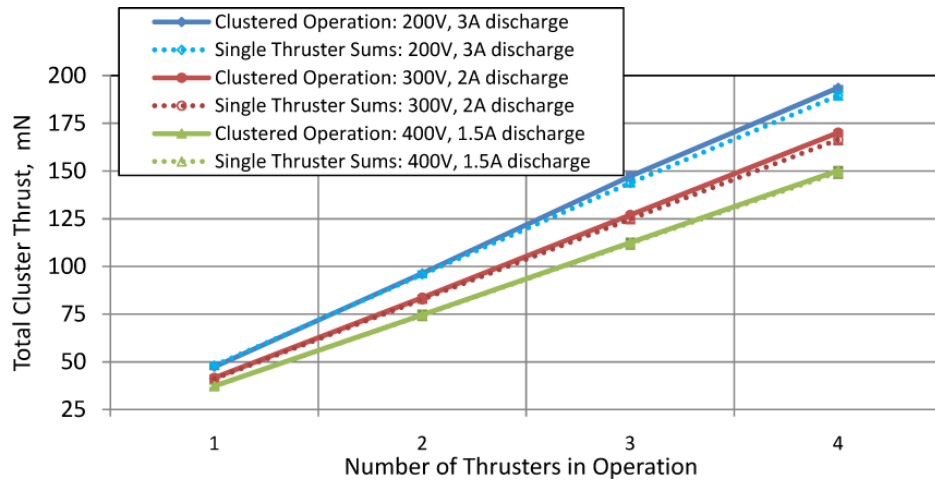


Figure A.7. Total thrust produced by single (600 W), dual (2 x 600 W), tri (3 x 600 W), and quad (4 x 600 W) Hall thruster cluster operation. Also shown, is the sum of the thrusts collected for each of the thruster when operating alone (un-clustered). The clustered total thrust exceeds the sum of the non-clustered individual thrusts in all cases.

Here the linear trend of increased thrust is apparent as additional HETs are added to the clustered configuration. Now, in addition to these data, the sums of the thrusts from the individually (non-clustered) operated Hall thrusters are also shown in Figure A.7. Remarkably, for each data-point, the clustered net-thrust exceeds the sum of the individual thrusters—and at several points these differences exceed all of the uncertainties involved in the measurements of thrust. Thus is it experimentally proven that when clustering together Hall thrusters, the thrusts of one-plus-one does not equal two. This clustered boost in thrust is shown in Table A.1.

Table A.1. Gain in thrust due to clustering Hall thrusters for three discharge voltages.

V_D (V)	I_D (A)	Indiv. Thrust per Thruster (mN)	Clustered Thrust per Thruster (mN)	Boost in thrust from clustering (%)
200	3.0	47.2	49.0	3.62%
300	2.0	41.8	42.9	2.55%
400	1.5	37.4	37.6	0.65%

To determine the listed “Thrust per Thruster” values, a linear regression was applied to each of the six curves in Figure A.7. The resulting slope possesses the units of mN/thruster and is thus used to populate Table A.1. This method may underestimate the clustered per thruster thrust since all clustered configurations are weighted equally in a method of least squares fit. It is plausible that thrust boost is a non-linear function of the number of clustered Hall thrusters. Yet, with only four Hall thrusters to study in this research there is no way to be certain what might happen to the thrust boost as dozens of Hall thrusters are clustered together. The percent boosts in thrust shown in Table A.1 are with respect to the non-clustered condition of operation. While a mere 0.65% gain in thrust is achieved at a 400-V discharge, a whopping 3.6% thrust boost occurs at 200-V. As has been suggested in prior Hall clustering research, localized propellant re-digestion may provide a physical mechanism to increase thrust. For the presented fixed-power data it is noticed that the propellant flowrate is highest at the lower voltage discharges; at 200-V 3-A, the anode flow to a single thruster registers 3.57 mg/sec (versus 2.47 mg/sec for a 300-V 2-A discharge and 1.91 mg/sec for a 400-V 1.5-A discharge). The ratio of the 200-V thrust boost to the 300-V thrust boost works out to 1.42 while flowrate ratios equate 1.50; certainly lending support to the localized propellant re-digestion hypothesis.

A.6 Facility Effects on the Production of Thrust

One possible flaw in the propellant localized re-digestion hypothesis is the vacuum chamber facility-effects, since the aggregate flowrate when running the full four thruster cluster is four times the flowrate incurred in running a single thruster. Prior research has been applied to understanding and correcting for the facility effects in operating electric thrusters of this kind [13, 41]. Thankfully, the cluster utilized in this research is quite low

in power at 600-W per thruster, and thus the seven employed cryogenic pumps do not struggle to maintain high-vacuum conditions ($< 1 \times 10^{-5}$ torr) whilst pumping 240,000 liters of xenon per second. To put this back-pressure effect into perspective, some basic gas kinetics laws regarding the random flux of particles into the discharge channel are used to express the thrust increment $\Delta T_{chamber}$ due to this pressure [41, 119]:

$$\Delta T_{chamber} = A_{eff} P_{chamber} P_{ioniz} \sqrt{\frac{eV_D}{\pi k T_{amb}}} \quad (\text{A.5})$$

where, A_{eff} is the *effective area* of the discharge channel, $P_{chamber}$ is the corrected chamber pressure, P_{ioniz} is the probability of ionization (100% assumed here), e is the charge constant, V_D is the discharge voltage, k is Boltzmann's constant, and T_{amb} is the ambient room temperature in Kelvin (all SI units). This equation conservatively assumes that the ingested particles (xenon atoms here) accelerate to the full potential of the discharge voltage. Using the combined discharge channel area of all four thruster discharge channels, $A_{eff} \approx 48 \text{ cm}^2$, $T_{amb} = 315 \text{ K}$, and $V_D = 200 \text{ V}$, Table A.2 is constructed:

Table A.2. Estimation of facility-effect-thrust for clustered HETs.

$P_{chamber}$ (torr)	$\Delta T_{chamber}$ (mN)
1.00×10^{-7}	0.003
1.00×10^{-6}	0.031
1.00×10^{-5}	0.310
1.50×10^{-5}	0.465
2.00×10^{-5}	0.620
1.00×10^{-4}	3.100

The highest measured corrected chamber pressure was 1.5×10^{-5} torr, occurring during the operation of the full four-thruster cluster at a discharge of 200-V 3-A. The total clustered thrust generated at this condition measured 193.6 mN (± 0.9 mN). According to Table A.2, the estimated facility-effect contribution to total thrust is only 0.5 mN or about 0.3% of the total thrust. While a better means than the provided kinetic estimate is required to truly quantify the facility effects of the 600-W HET cluster, it is at least clear that the magnitude of thrust due to facility caused propellant re-digestion is on the order of the overall error in the measurement of thrust. As such, the observed increases in thrust (in Table A.1) can only be attributed to localized propellant re-digestion (an effect that would also occur in the true vacuum of space, due to the close thruster-to-thruster proximity within this cluster) or some other clustering phenomena such as beam focusing that have been observed in clustered Hall thruster beams.[40]

A.7 Cluster Performance: Additional Results and Discussion

Next presented in Figure A.8 and Figure A.9 are the clustered anode efficiency versus discharge voltage, and the clustered thrust to power versus anode specific impulse, respectively:

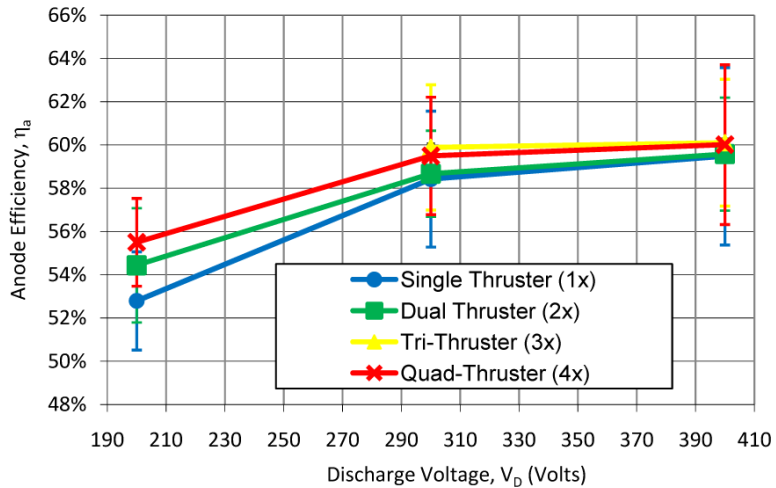


Figure A.8. Anode efficiency for various clustered configurations. The single thruster data represent the mean anode efficiency computed from separate experiments with each of the four thrusters at the three discharge voltages shown.

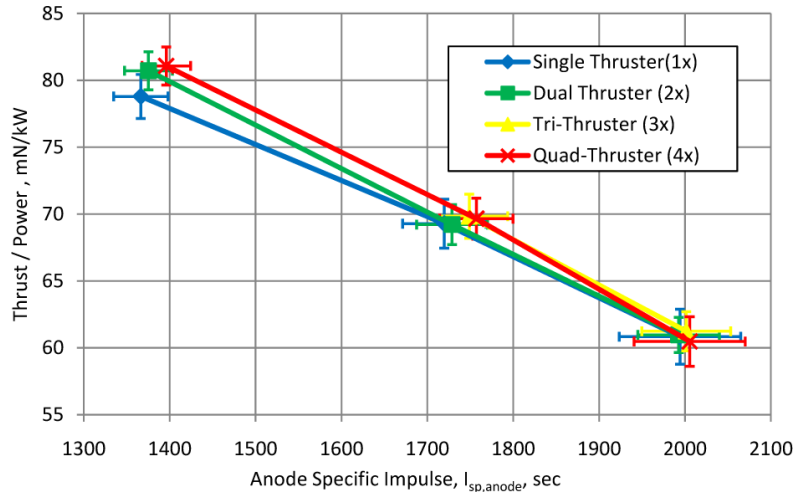


Figure A.9. Thrust-to-Power ratios plotted against anode specific impulse for all clustered configurations. The single thruster data represents the mean T/P_D computed from separate experiments with each of the four thrusters.

While the overall clustering trend of improved performance is indeed observed in the preceding two figures, the absolute errors propagated into the computations of anode efficiency and anode specific impulse overwhelm the certainty in these trends. To more accurately display the data, the single thruster data points are computed from the average values of these performance parameters (T/P_D , η_a , and $I_{sp,a}$) as measured separately with each of the four 600-W thrusters. As was seen in Figure A.7, where the sum of the

individually measured thrusts was less than the total clustered thrust, it is also observed here that the clustered values of T/P_D , η_a , and $I_{sp,a}$, exceed those same values measured during single thruster operation. Recalling that a maximal boost in thrust is observed at our lowest voltage 200 V discharge setting, we see that this corresponds to our least efficient point. This implies that the performance benefits from clustering are greater for lower efficiencies. Considering how anode efficiency is defined in Eqn. (A.1), the clustered boost in thrust must result from increased free propellant flux. The anode efficiency of the Hall thruster drops at low voltage likely because more xenon is being exhausted than can be effectively ionized and fully accelerated away from the anode. Thus, a larger fraction of neutrals and incompletely accelerated ions exit each Hall thruster discharge channel. In single thruster operation, these particles would stream or radiate away from the thruster and contribute little to the overall thrust. However, when Hall thrusters are closely clustered together, many of these particles will stream across the faces of the neighboring thrusters. To these neighboring thrusters the overlapping plumes give rise to slight increases in the localized density near the discharge channels (compared to non-clustered operation where no plume overlap occurs). This additional flux of propellant can then be more fully ionized and accelerated by these neighboring thrusters thereby leading to increased overall performance of the cluster. In this way, clustered Hall thrusters cooperate with each other to improve performance beyond what is achieved alone and un-clustered.

A.8 Concluding Remarks

Fixed-power, 600-W per thruster, performance measurements have been performed with the 600-W HET four thruster cluster in all basic configurations including: single-

thruster, dual-thruster, tri-thruster, and quad-thruster operation. Single-thruster quasi-optimizations were carried out with one of the 600-W Hall thrusters at 8 different discharge voltages between 150 Volts and 600 Volts. Nominal accuracy in the absolute measurement of thrust averaged ± 1 mN with an observed repeatability of ± 0.3 mN. Cold gas flow corrections were applied to the measurement technique, and vacuum facility effects were estimated to contribute negligible thrust (< 1 mN) at all operational conditions from quad- to single-thruster. Performance measurements from the clustered configurations exceeded the single-thruster values for each the three discharge voltages evaluated (200 V, 300 V, and 400 V). The total thrust from the running of each of the clustered configurations always exceeded the sum of the thrusts produced by the same thrusters when operated alone. The direct gain in thrust due to clustering measured +1.8 mN per additional thruster (+3.6%) at 200 V and +0.2 mN per additional thruster (+0.7%) at 400V. Small increases are similarly observed in the clustered efficiencies and clustered specific impulses when compared to the non-clustered (single thruster) performance.

Bibliography

- [1] Jahn, R. G., *Physics of electric propulsion*, McGraw-Hill, 1968.
- [2] Sutton, G. P. and Biblarz, O., *Rocket Propulsion Elements*, 7th Edition, Wiley-Interscience, 2000.
- [3] Goebel, D. M. and Katz, I., *Fundamentals of Electric Propulsion: Ion and Hall Thrusters*, Wiley, 2008.
- [4] Kim, V., "Electric propulsion activity in Russia," IEPC-2001-005, 27th International Electric Propulsion Conference, Pasadena, California, October 14–19, 2001.
- [5] The Aerospace Corporation, "Crosslink: Developing Responsive and Agile Space Systems, Research Horizons: Low-Power Electric Propulsion", vol. 10, no. 1, Summer 2009.
- [6] Gascon, N., Dudeck, M., and Barral, S., "Wall material effects in stationary plasma thrusters. I. Parametric studies of an SPT-100," *Physics of Plasmas*, vol. 10, pp. 4123-4136, Oct. 2003.
- [7] Barral, S., Makowski, K., Peradzynski, Z., Gascon, N., and Dudeck, M., "Wall material effects in stationary plasma thrusters. II. Near-wall and in-wall conductivity," *Physics of Plasmas*, vol. 10, pp. 4137-4152, Oct. 2003.
- [8] Gascon, N., Crawford, S., Corey, R., and Cappelli, M., "Coaxial Hall Thruster with Diamond Inner Channel Wall," AIAA-2006-4995, 42nd Joint Propulsion Conference, 9-12 July, Sacramento, CA, 2006.
- [9] Television Bureau of Advertising, "TV Basics Alternate Delivery Systems - National," <http://www.tvb.org/rcentral/mediatrendstrack/tvbasics/12_ADS-Natl.asp>, date retrieved: 20 Dec. 2009.
- [10] Lieberman, A., Leanna, A., McAlonan, M., and Heshmatpour, B., "Small Thermoelectric Radioisotope Power Sources," SPACE TECHNOLOGY AND APPLICATIONS INTERNATIONAL FORUM-STAIIF 2007: 11th Conf Thermophys.Applic.in Micrograv.; 24th Symp Space Nucl. Pwr. Propulsion; 5th Conf

Hum./Robotic Techn. & Vision Space Explor.; 5th Symp. Space Coloniz.; 4th Symp New Frontiers & Future Concepts, pp. 347-354, Albuquerque, New Mexico (USA): AIP, 2007.

[11] Knight, T. and Anghaie, S., "Estimation of Specific Mass for Multimegawatt NEP Systems Based on Vapor Core Reactors with MHD Power Conversion," SPACE TECHNOLOGY AND APPLICATIONS INTERNATIONAL FORUM-STAIIF 2004: Conf. on Thermophys. in Microgravity; Commercial/Civil Next Gen. Space Transp.; 21st Symp. Space Nuclear Power Human Space Explor.; Space Colonization; New Frontiers & Future Concepts, pp. 379-387, Albuquerque, New Mexico (USA): AIP, 2004.

[12] Hargus, W. and Reed, G., "The Air Force Clustered Hall Thruster Program," AIAA-2002-3678, 38th AIAA/ASME/SAE/ASEE Joint Propulsion Conference and Exhibit, Indianapolis, IN, 2002.

[13] Walker, M. L. R., "Effects of Facility Backpressure on the Performance and Plume of a Hall Thruster," Ph.D. Thesis Ann Arbor: University of Michigan, 2005.

[14] Kuninaka, H., Nishiyama, K., Shimizu, Y., Yamada, T., Funaki, I., Hosoda, S., and Koizumi, H., "Re-ignition of Microwave Discharge Ion Engines on Hayabusa for Homeward Journey," IEPC-2007-009, 30th International Electric Propulsion Conference, Florence, Italy, September 17-20, 2007.

[15] Press Release by the Japan Aerospace Exploration Agency (JAXA), "Restoration of Asteroid Explorer, HAYABUSA's Return Cruise," November 19, 2009.

[16] Choueiri, E. Y., "Plasma oscillations in Hall thrusters," Physics of Plasmas, vol. 8, pp. 1411-1426, Apr. 2001.

[17] Beiting, E., Garrett, M., Pollard, J., Pezet, B. and Gouvernayre, P., "Spectral Characteristics of Radiated Emission from SPT-100 Hall Thrusters," IEPC-2005-221, 29th International Electric Propulsion Conference, Princeton University, New Jersey, 2005.

[18] Chesta, E., Lam, C. M., Meezan, N. B., Schmidt, D. P., and Cappelli, M. A., "A characterization of plasma fluctuations within a Hall discharge," IEEE Transactions on Plasma Science, vol. 29, pp. 582-591, 2001.

[19] Bugrova, A., Desyatskov, A., Morozov, A., and Kharchevnikov, V., "Measurement of the plasma electron temperature with microsecond resolution," Instruments and Experimental Techniques, vol. 43, pp. 528-531, Jul. 2000.

- [20] Janes, G. S. and Lowder, R. S., "Anomalous Electron Diffusion and Ion Acceleration in a Low-Density Plasma," *Physics of Fluids*, vol. 9, pp. 1115-1123, Jun. 1966.
- [21] Albarede, L., Mazouffre, S., Bouchoule, A., and Dudeck, M., "Low-frequency electron dynamics in the near field of a Hall effect thruster," *Physics of Plasmas*, vol. 13, p. 063505, 2006.
- [22] Bradley, J. W., Bäcker, H., Kelly, P. J., and Arnell, R. D., "Space and time resolved Langmuir probe measurements in a 100 kHz pulsed rectangular magnetron system," *Surface and Coatings Technology*, vol. 142-144, pp. 337-341, Jul. 2001.
- [23] Fife, J. M., Martinez-Sanchez, M., and Szabo, J., "A numerical study of low-frequency discharge oscillations in Hall thrusters," AIAA-1997-3051, 33rd AIAA Joint Propulsion Conference, 1997.
- [24] Boeuf, J. P. and Garrigues, L., "Low frequency oscillations in a stationary plasma thruster," *Journal of Applied Physics*, vol. 84, pp. 3541-3554, Oct. 1998.
- [25] Baranov, V. I., Nazarenko, Y. S., Petrosov, V. A., Vasin, A. I., and Yashnov, Y. M., "Theory of oscillations and conductivity for Hall thruster," AIAA-1996-3192, 32nd AIAA, ASME, SAE, and ASEE, Joint Propulsion Conference and Exhibit, Lake Buena Vista, FL, 1996.
- [26] Barral, S. and Ahedo, E., "On the Origin of Low Frequency Oscillations in Hall Thrusters," *PLASMA 2007: International Conference on Research and Applications of Plasmas*, AIP Conference Proceedings, vol. 993, p. 439, 2008.
- [27] Zhurin, V., Kahn, J., Kaufman, H., Kozubsky, K., and Day, M., "Dynamic Characteristics of Closed Drift Thrusters," IEPC-93-095, 23rd International Electric Propulsion Conference, Seattle, WA, 1993.
- [28] Yoshikawa, S. and Rose, D. J., "Anomalous Diffusion of a Plasma across a Magnetic Field," *Physics of Fluids*, vol. 5, pp. 334-340, Mar. 1962.
- [29] Connor, J. W., Fasoli, A., Hidalgo, C., Kirk, A., Naulin, V., Peeters, A. G., and Tala, T., "13th EU-US Transport Task Force Workshop on transport in fusion plasmas," *Nucl. Fusion*, vol. 49, p. 047001, 2009.
- [30] Nedospasov, A. V., "On the estimation by Kadomtsev of coefficients of turbulent transport in magnetized plasma," *Physics of Plasmas*, vol. 16, pp. 060501-6, Jun. 2009.
- [31] Stangeby, P., *The Plasma Boundary of Magnetic Fusion Devices*, Taylor & Francis, 2000.

- [32] Boniface, C., Garrigues, L., Hagelaar, G. J. M., Boeuf, J. P., Gawron, D., and Mazouffre, S., "Anomalous cross field electron transport in a Hall effect thruster," *Applied Physics Letters*, vol. 89, pp. 161503-3, Oct. 2006.
- [33] Raitses, Y., Staack, D., Keidar, M., and Fisch, N. J., "Electron-wall interaction in Hall thrusters," *Physics of Plasmas*, vol. 12, pp. 057104-9, May. 2005.
- [34] Taccogna, F., Longo, S., Capitelli, M., and Schneider, R., "Anomalous transport induced by sheath instability in Hall effect thrusters," *Applied Physics Letters*, vol. 94, pp. 251502-3, Jun. 2009.
- [35] Keidar, M. and Beilis, I. I., "Sheath and boundary conditions for plasma simulations of a Hall thruster discharge with magnetic lenses," *Applied Physics Letters*, vol. 94, pp. 191501-3, May. 2009.
- [36] Prepared by NOAA, NASA, and USAF, *U.S. Standard Atmosphere, 1976*, U.S. Government Printing Office, Washington, DC, 1976.
- [37] Gulczinski, F. and Schilling, J., "Comparison of Orbit Transfer Vehicle Concepts Utilizing Mid-Term Power and Propulsion Options," IEPC-2003-0022, March 2003.
- [38] Beal, B. E. and Gallimore, A. D., "Energy analysis of a Hall thruster cluster," IEPC-2003-035, 28th International Electric Propulsion Conference, Toulouse, France: 2003.
- [39] Beal, B. E., Gallimore, A. D., Haas, J. M., and Hargus, W. A., "Plasma properties in the plume of a Hall thruster cluster," *Journal of Propulsion and Power*, vol. 20, pp. 985-991, 2004.
- [40] Beal, B. E., "Clustering of Hall Effect Thrusters for High-Power Electric Propulsion Applications," Ph.D. Thesis, University of Michigan, Ann Arbor 2004.
- [41] Walker, M. L. R. and Gallimore, A. D., "Performance Characteristics of a Cluster of 5-kW Laboratory Hall Thrusters," *Journal of Propulsion and Power*, vol. 23, pp. 35-43, 2007.
- [42] Zakharenkov, L. E., Semenkin, A. V., Rusakov, A. V., Urchenko, N. A., Tverdokhlebov, S. O., Garkusha, V.I., Lebedev, U.V., Podkolsin, S. N., and Fife, J. M., "STUDY OF MULTI THRUSTER ASSEMBLY OPERATION," IEPC-2003-0311, 28th International Electric Propulsion Conference, Toulouse, France:, 2003.
- [43] Jacobson, D. T. and Manzella, D. H., "50 KW Class Krypton Hall Thruster Performance," AIAA 2003-4550, 39th AIAA/ASME/SAE/ASEE Joint Propulsion Conference and Exhibit, Huntsville, Alabama, 20-23 July 2003.

- [44] Lobbia, R. B. and Gallimore, A. D., "Performance Measurements from a Cluster of Four Hall Thrusters," IEPC-2007-177, 30th International Electric Propulsion Conference, Florence, Italy 2007.
- [45] Kusamoto, D. and Komurasaki, K., "Optical Diagnosis of Plasma in a Channel of Hall Thrusters," IEPC-97-067, 25th International Electric Propulsion Conf., Cleveland, OH, 1997.
- [46] Darnon, F., Lyszyk, M., and Bouchoule, A., "Optical investigations on plasma oscillations of SPT thrusters," AIAA-1997-3051, 33rd Joint Propulsion Conference, Seattle, WA, pp. 6–9, 1997.
- [47] Gascon, N., Thomas, C., Hermann, W., and Cappelli, M. A., "FURTHER INVESTIGATIONS OF AN OPEN DRIFT HALL THRUSTER WITH BORON NITRIDE AND DIAMOND WALL," IEPC-2003-0327, 28th International Electric Propulsion Conference, Toulouse, France, 2003.
- [48] Yamamoto, N., Yokota, S., Watanabe, K., Sasoh, A., Komurasaki, K., and Arakawa, Y., "Suppression of Discharge Current Oscillations in a Hall Thruster," *Trans Jpn Soc Aeronaut Space Sci*, vol. 48, pp. 169-174, 2005.
- [49] Daren, Y., Jiapeng, D., and Jingmin, D., "Spectrum Diagnosis for Fuchsia Plume of Hall Effect Thruster with Xenon as Propellant," *Plasma Science and Technology*, vol. 8, pp. 685-689, 2006.
- [50] Kester, W., *Data Conversion Handbook*, Newnes, 2004.
- [51] Lobbia, R. B. and Gallimore, A. D., "High-speed Dual Langmuir Probe," *Review of Scientific Instruments*, submitted for review, 2009.
- [52] Mott-Smith, H. M. and Langmuir, I., "The Theory of Collectors in Gaseous Discharges," *Physical Review*, vol. 28, p. 727, Oct. 1926.
- [53] Lieberman, M. A. and Lichtenberg, A. J., *Principles of plasma discharges and materials processing*, John Wiley and Sons, 2005.
- [54] Swift, J. D. and Schwar, M. J. R., *Electrical probes for plasma diagnostics*, American Elsevier Publishing, New York, 1970.
- [55] Chen, F. F., Editor: Huddlestone, R. H., *Plasma Diagnostic Techniques*, New York: Academic Press, pp. 113-200, 1965.
- [56] Hershkowitz, N., "How Langmuir probes work," *Plasma Diagnostics* vol. 1, pp. 113-183, Academic Press, San Diego, 1989.

- [57] Liewer, P. C., McChesney, J. M., Zweben, S. J., and Gould, R. W., "Temperature fluctuations and heat transport in the edge regions of a tokamak," *Physics of Fluids*, vol. 29, pp. 309-317, Jan. 1986.
- [58] Balbin, R., Hidalgo, C., Pedrosa, M. A., Garcia-Cortes, I., and Vega, J., "Measurement of density and temperature fluctuations using a fast-swept Langmuir probe," *Proceedings of the 9th topical conference on high temperature plasma diagnostics*, pp. 4605-4607, Santa Fe, New Mexico (USA): AIP, 1992.
- [59] Giannone, L., Balbin, R., Niedermeyer, H., Endler, M., Herre, G., Hidalgo, C., Rudyj, A., Theimer, G., and Verplanke, P., "Density, temperature, and potential fluctuation measurements by the swept Langmuir probe technique in Wendelstein 7-AS," *Physics of Plasmas*, vol. 1, pp. 3614-3621, Nov. 1994.
- [60] Chiodini, G., Riccardi, C., and Fontanesi, M., "A 400 kHz, fast-sweep Langmuir probe for measuring plasma fluctuations," *Review of Scientific Instruments*, vol. 70, p. 2681, 1999.
- [61] Schubert, M., Endler, M., and Thomsen, H., "Spatiotemporal temperature fluctuation measurements by means of a fast swept Langmuir probe array," *Review of Scientific Instruments*, vol. 78, pp. 053505-7, May. 2007.
- [62] Yang, T. F., Zu, Q. X., and Liu, P., "A dual-cable noise reduction method for Langmuir probes," *Review of Scientific Instruments*, vol. 66, pp. 3879-3882, Jul. 1995.
- [63] Lobbia, R. B., Liu, T. M., and Gallimore, A. D., "Correlating Time-resolved Optical and Langmuir Probe Measurements of Hall Thruster Dynamics," SPS-III-36, Presented at the JANNAF 6th Modeling and Simulation / 4th Liquid Propulsion / 3rd Spacecraft Propulsion Joint Subcommittee Meeting, Orlando, FL, December 8-12, 2008.
- [64] Lobbia, R. B. and Gallimore, A. D., "Temporal Limits of a Rapidly Swept Langmuir Probe," *Review of Scientific Instruments*, submitted for review, 2009.
- [65] Kluiver, H. D., Barth, C. J., and Donne, A. J. H., "Current driven turbulence and microturbulent spectra in the TORTUR Tokamak," *Plasma Physics and Controlled Fusion*, vol. 30, pp. 699-719, 1988.
- [66] Crawford, F. W., "Frequency Spectra of Low-Frequency Fluctuations in a Plasma," *Journal of Applied Physics*, vol. 33, p. 15, 1962.
- [67] Mott-Smith, H. M. and Langmuir, I., "The Theory of Collectors in Gaseous Discharges," *Physical Review*, vol. 28, p. 727, Oct. 1926.

- [68] Hippler, R., Pfau, S., Schmidt, M., and Schoenbach, K. H., *Low Temperature Plasmas*, Wiley-VCH, 2008.
- [69] Crawford, F. W., "Modulated Langmuir Probe Characteristics," *Journal of Applied Physics*, vol. 34, pp. 1897-1902, Jul. 1963.
- [70] Demetriades, A. and Doughman, E. L., "Langmuir probe diagnosis of turbulent plasmas," *AIAA Journal*, vol. 4, pp. 451-459, 1966.
- [71] Stalder, K. R., Anderson, C. A., Mullan, A. A., and Graham, W. G., "Time-resolved optical emission and electron energy distribution function measurements in rf plasmas," *Journal of Applied Physics*, vol. 72, pp. 1290-1296, 1992.
- [72] Hutchinson, I. H., *Principles of plasma diagnostics*, Cambridge University Press, 2002.
- [73] Cherrington, B. E., "The use of electrostatic probes for plasma diagnostics—A review," *Plasma Chemistry and Plasma Processing*, vol. 2, pp. 113-140, 1982.
- [74] Okuda, T., "Dynamic properties of a probe in gas-discharge plasma," *Journal of the Institute of Electrical Engineers (Japan)*, vol. 83, pp. 28-38, 1963.
- [75] Nikiforov, S., Kim, G., and Rim, G., "Dynamics of high-voltage pulsed cylindrical sheath," *Plasma Science, IEEE Transactions on*, vol. 31, pp. 94-103, 2003.
- [76] Calder, A. C. and Laframboise, J. G., "Time-dependent sheath response to abrupt electrode voltage changes," *Physics of Fluids B: Plasma Physics*, vol. 2, pp. 655-666, Mar. 1990.
- [77] Shih, C. H. and Levi, E., "Transient performance of negatively biased Langmuir probes," *AIAA Journal*, vol. 10, pp. 104-110, 1972.
- [78] Lieberman, M. A., "Model of plasma immersion ion implantation," *Journal of Applied Physics*, vol. 66, pp. 2926-2929, Oct. 1989.
- [79] Oskam, H., Carlson, R., and Okuda, T., "Studies of the dynamic properties of Langmuir probes III: Discussion of the results," *Physica*, vol. 30, pp. 375-386, Feb. 1964.
- [80] Loeb, L., *Recent advances in basic processes of gaseous electronics*, vol. 1, Berkeley: University of California Press, 1973.
- [81] McMahon, J. C., Xu, G. Z., and Laframboise, J. G., "The effect of ion drift on the sheath, presheath, and ion-current collection for cylinders in a collisionless plasma," *Physics of Plasmas*, vol. 12, pp. 062109-11, Jun. 2005.

- [82] Chung, P. M., Talbot, L., and Touryan, K. J., "Electric Probes in stationary and flowing plasma: Part 1. Collisionless and transitional probes," *AIAA Journal*, vol. 12, pp. 133-154, 1974.
- [83] Stangeby, P. C., "Measuring plasma drift velocities in tokamak edge plasmas using probes," *Physics of Fluids*, vol. 27, pp. 2699-2704, Nov. 1984.
- [84] Hoegy, W. R. and Wharton, L. E., "Current to a moving cylindrical electrostatic probe," *Journal of Applied Physics*, vol. 44, pp. 5365-5371, Dec. 1973.
- [85] Stangeby, P. C., "Plasma sheath transmission factors for tokamak edge plasmas," *Physics of Fluids*, vol. 27, pp. 682-690, Mar. 1984.
- [86] Sheridan, T. E. and Goree, J., "Langmuir-probe characteristic in the presence of drifting electrons," *Physical Review E*, vol. 50, p. 2991, Oct. 1994.
- [87] Chen, F. F., *Introduction to Plasma Physics and Controlled Fusion*, Springer, 2006.
- [88] Nedospasov, A. V. and Uzdensky, D. A., "On Dynamical Effects on I-V Characteristic of Langmuir Probes in Tokamak Edge Plasma," *Contributions to Plasma Physics*, vol. 34, pp. 478-483, 1994.
- [89] Okuda, T., Carlson, R., and Oskam, H., "Studies of the dynamic properties of Langmuir probes II: Experimental results," *Physica*, vol. 30, pp. 193-205, Jan. 1964.
- [90] Crawford, F. W. and Grard, R., "Low-Frequency Impedance Characteristics of a Langmuir Probe in a Plasma," *Journal of Applied Physics*, vol. 37, pp. 180-183, Jan. 1966.
- [91] Wang, S. and Wendt, A., "Sheath thickness evaluation for collisionless or weakly collisional bounded plasmas," *Plasma Science, IEEE Transactions on*, vol. 27, pp. 1358-1365, 1999.
- [92] Brace, L. H.; Editors: Pfaff, R. F., Borovsky, J. E., and Young, D. T., *Measurement techniques in space plasmas*, pp. 23-34, American Geophysical Union, 1998.
- [93] Lobbia, R. B. and Gallimore, A. D., "Fusing spatially and temporally separated single-point turbulent plasma flow measurements into two-dimensional time-resolved visualizations," *Information Fusion, 2009. FUSION '09. 12th International Conference on*, pp. 678-685, 2009.
- [94] Williams Jr, G. J., Smith, T. B., Gulczinski III, F. S., Beal, B. E., Gallimore, A. D., and Drake, R. P., "Laser Induced Fluorescence Measurement of Ion Velocities in the

Plume of a Hall Effect Thruster,” AIAA-1999-2424, 35th AIAA/ASME/SAE/ASEE Joint Propulsion Conference, Los Angeles, CA, June 1999.

[95] Hussain, A. K. M. F. and Reynolds, W. C., “The Mechanics of an Organized Wave in Turbulent Shear Flow,” *Journal of Fluid Mechanics Digital Archive*, vol. 41, pp. 241-258, 1970.

[96] Sung, J. and Yoo, J. Y., “Three-dimensional phase averaging of time-resolved PIV measurement data,” *Measurement Science and Technology*, vol. 12, pp. 655-662, 2001.

[97] Bonhomme, G., Enjolras, C., Kurzyna, J., Mazouffre, S., Albarede, L., and Dudeck II, M., “Characterization of Hall Effect Thruster Plasma Oscillations based on the Hilbert-Huang Transform,” IEPC-2005-46, 29th International Electric Propulsion Conference,, Princeton, New Jersey: 2005.

[98] Lobbia, R.B. and A.D. Gallimore, "Evaluation and Active Control of Clustered Hall Thruster Discharge Oscillations," AIAA-2005-3679, 41st AIAA Joint Propulsion Conference and Exhibit, Tucson, Arizona, 2005.

[99] Lazurenko, A., Albarède, L., and Bouchoule, A., "High-frequency Instabilities in Hall-effect Thrusters: Correlation with the Discharge Current and Thruster Scale Impact," IEPC-2005-142, 29th International Electric Propulsion Conference, Princeton University, October 31 – November 4, 2005.

[100] Knoll, A. K. and Cappelli, M. A., "Experimental Characterization of High Frequency Instabilities within the Discharge Channel of a Hall Thruster," IEPC-2009-099, 31st International Electric Propulsion Conference, University of Michigan, Ann Arbor, Michigan, USA, September 20-24, 2009.

[101] Katz, I., Parks, D. E., Gardner, B. M., Mende, S. B., Collin, H. L., Manzella, D. H., and Myers, R. M., “Spectral line emission by the SEPAC plasma contactor-Comparison between measurement and theory,” AIAA-1995-0369, Aerospace Sciences Meeting and Exhibit, 33 rd, Reno, NV, 1995.

[102] Hofer, R. R. and Jankovsky, R. S., "The Influence of Current Density and Magnetic Field Topography in Optimizing the Performance, Divergence, and Plasma Oscillations of High Specific Impulse Hall Thrusters," IEPC-2003-142, 28th International Electric Propulsion, Toulouse, France, March 17-21 2003.

[103] Hargus, W.A., Pote, B., “Examination of a Hall Thruster Start Transient,” AIAA-2002-3956, 38th AIAA Joint Propulsion Conference and Exhibit, Indianapolis, IN., July 2002.

- [104] Yamamoto, N., Nakagawa, T., Komurasaki, K., Arakawa, Y., "Extending Stable Operation Range in Hall Thrusters," AIAA-2002-3953, 38th AIAA/ASME/SAE/ASEE Joint Propulsion Conference and Exhibit, Indianapolis, Indiana, July 7-10, 2002.
- [105] Gascon, N., Bechu, S., Lasgorceix, P., Izrar, B., Dudeck, M., Bonhomme, G., Caron, X., "Signal processing and non-linear behavior of a Stationary Plasma Thruster - First results," AIAA-1999-2427, 35th AIAA/ASME/SAE/ASEE Joint Propulsion Conference and Exhibit, Los Angeles, CA, June 20-24, 1999.
- [106] Yamamoto, N., Arakawa, Y., and Komurasaki, K., "Discharge Current Oscillation in Hall Thrusters," Journal of Propulsion and Power, vol. 21, pp. 870-876, 2005.
- [107] Schmidt, D. P., Meezan, N. B., Jr, W. A. H., and Cappelli, M. A., "A low-power, linear-geometry Hall plasma source with an open electron-drift," Plasma Sources Science and Technology, vol. 9, pp. 68-76, 2000.
- [108] Litvak, A. A., Raitses, Y., and Fisch, N. J., "High-frequency probing diagnostic for Hall current plasma thrusters," Review of Scientific Instruments, vol. 73, p. 2882, 2002.
- [109] Linnell, J. and Gallimore, A., "Statistical Analysis of the Acceleration Zone Location in Hall Thrusters," AIAA-2008-4721 44th AIAA/ASME/SAE/ASEE Joint Propulsion Conference and Exhibit, Hartford, CT, July 2008.
- [110] Beal, B. E., Gallimore, A. D., and Hargus, W. A., "Preliminary Plume Characterization of a Low-Power Hall Thruster Cluster," AIAA-2002-4251, 38th Joint Propulsion Conference, Indianapolis, IN, July 7-10, 2002.
- [111] Lobbia, R. B. and Gallimore, A. D., "Two-dimensional Time-resolved Breathing Mode Plasma Fluctuation Variation with Hall Thruster Discharge Settings," IEPC-2009-106, 31st International Electric Propulsion Conference, University of Michigan, Ann Arbor, Michigan, USA, September 20-24, 2009.
- [112] Lobbia, R., Liu, T., and Gallimore, A., "Temporally and Spatially Resolved Measurements in the Plume of Clustered Hall Thrusters," AIAA-2009-5354, 45th AIAA/ASME/SAE/ASEE Joint Propulsion Conference and Exhibit, Denver, Colorado, Aug. 2-5, 2009.
- [113] Lobbia, R. B. and Gallimore, A. D., "A Method of Measuring Transient Plume Properties," AIAA-2008-4650, 44th AIAA/ASME/SAE/ASEE Joint Propulsion Conference and Exhibit, Hartford, CT, July 21-23, 2008.

- [114] Jacobson, D. T. and Manzella, D. H., "50 KW Class Krypton Hall Thruster Performance," AIAA-2003-4550, 39th AIAA/ASME/SAE/ASEE Joint Propulsion Conference and Exhibit, Huntsville, Alabama, 20-23 July 2003.
- [115] Reid, B. M., Gallimore, A. D., Hofer, R. R., "Correcting Hall Thruster Performance Measurements for the Effects of Vacuum Facility Background Gas Entrainment," Journal of Propulsion and Power, submitted for publication, 2007.
- [116] McDonald, M. S. and Gallimore, A. D., "Cathode Position and Orientation Effects on Cathode Coupling in a 6-kW Hall Thruster," IEPC-2009-113, 31st International Electric Propulsion Conference, University of Michigan, Ann Arbor, Michigan, USA, September 20-24, 2009.
- [117] Walker, M. L. and Gallimore, A. D., "Hall Thruster Cluster Operation with a Shared Cathode," Journal of Propulsion and Power, vol. 23, p. 528, 2007.
- [118] Pote, B. H., Hruby, V., and Monheiser, J., "Performance of an 8 kW Hall Thruster," IEPC-1999-080, 25th International Electric Propulsion Conference, Kitakyushu, Japan, 1999.
- [119] Randolph, T., Kim, V., Kaufman, H., Kozubsky, K., Zhurin, V. V., and Day, M., "Facility Effects on Stationary Plasma Thruster Testing," IEPC-1993-093, 23rd International Electric Propulsion Conference, Seattle, WA, USA, Sept. 1993.